This is to certify that the
dissertation entitled

Hyperthermia treatment of Breast Cancer with RF phased
array applicator and RF/US hybrid applicator

presented by

LIYONG WU

has been accepted towards fulfillment
of the requirements for the

Ph.D degree in Electrical & Computer Engineering

Robert J. McDougal

Major Professor's Signature

Oct. 27, 2006

Date

Hyperthermia treatment of Breast Cancer with RF phased array applicator and RF/US hybrid applicator

By

Liyong Wu

A DISSERTATION

Submitted to
Michigan State University
in partial fulfillment of the requirements
for the degree of

DOCTOR OF PHILOSOPHY

Department of Electrical and Computer Engineering

2006

ABSTRACT

Hyperthermia treatment of Breast Cancer with RF phased array applicator and RF/US hybrid applicator

By
Liyong Wu

Several RF phased array applicators have been designed and constructed for hyperthermia treatments in the intact breast. These RF phased arrays consist of four or five antennas mounted on a lexan water tank, and geometric focusing is employed so that each antenna points in the direction of the intended target. The operating frequency for these phased arrays ranges from 130-160 MHz. The RF arrays have been characterized both by electric field measurements in a water tank and by electric field simulations using the finite element method. The finite element simulations are performed includes the geometry of the tank enclosure, antennas and 3D patient model extracted from medical images. The electric (E) field, specific absorbing ratio (SAR) and temperature in the breast region by the four antenna applicator are calculated with SAR optimization. In order to improve the heating performance in deep region, an radio frequency/ultrasound (RF/US) hybrid applicator is designed and a square shape ultrasound phased array is mounted on one side wall and/or the bottom wall. The ultrasound phased array delivers energy into the deep region of the tumor, where RF can not reach and the combined heating has better performance than RF alone and US alone. The temperature distribution generated by the hybrid applicator shows

that the character of RF and US source improves the heating performance for regional hyperthermia. The effect of the E field polarization is also examined and a cross antenna, radiated E field in the circular polarization mode, is designed to remove the hot spot caused by E field linear polarization of the dual dipole antenna. Several new applicators based on the dipole antenna, U-shaped and cross antenna are designed for improving the heating performance and steering ability of the RF hyperthermia applicator.

For my wife, Xiangrong and my parents

ACKNOWLEDGMENTS

There are many people who deserve acknowledgement for both the work contained in this thesis, and the countless other things that I was able to be involved in during my time at Michigan State. First and foremost, a special thanks to Dr. Robert McGough for letting me walk my own paths, while always being there to point to things on the map. I have truly enjoyed my time as your student and feel fortunate to have been able to study under your guidance. Thanks to Dr. Shanker B. and Dr. Leo Kempel for teaching me some computational EM stuff that will help me for years to come. A thank you is also in order for Dr. Guowei Wei and Dr. Ed Rothwell, for agreeing to serve on my Ph.D. committee.

Thanks to James Kelly for research related talk, which inspires me new ideas. Thanks to Xiaozheng and Chen Duo for cooperation on the research. which helped me to keep up with publication activities.

A special acknowledgement to my parents for their love and support always. Thank you for that. My deepest gratitude is reserved for wife, Xiangrong, who has supported me throughout my studies and will give me a beautiful baby. Without your help, all this would not have been possible. I love you and our future baby with all my heart and soul.

TABLE OF CONTENTS

LIST OF FIGURES

LIST OF TABLES

CHAPTER 1

INTRODUCTION

1.1 The cellular and molecular basis for hyperthermia

Hyperthermia (also called thermal therapy or thermotherapy) is a type of cancer treatment in which body tissue is exposed to high temperatures. High temperatures can damage and kill cancer cells, usually with minimal injury to normal tissues [3]. By killing cancer cells and damaging proteins and structures within cells [4], hyperthermia can shrink tumors. Hyperthermic heating of the tumor to 43°C combined with radiation and/or chemotherapy is a proven treatment for malignant tumors [3, 5]. Hyperthermia makes some cancer cells more sensitive to radiation and harms other cancer cells that radiation cannot damage. Hyperthermia can also enhance the effects of certain anticancer drugs. The effectiveness of hyperthermia treatment is a function of the temperature achieved during the treatment, as well as the length of treatment and cell and tissue characteristics [3, 4]. To ensure that the desired temperature is reached, but not exceeded, the temperature of the tumor and surrounding tissue is monitored throughout the hyperthermia treatment [5]. Various modalities are available to heat tissue in *vivo*. The selected method depends on the location and the volume to be treated. There are two ways to heat the tumor: interstitial heating and external heating. The interstitial heating can be obtained by radio-frequency/microwave, ultrasound electrodes or introducing ferro-magnetic seeds in a tumor. The external heating can be obtained by ultrasound applicators (ultrasound array) or radio-frequent/microwave electromagnetic radiation.

Hyperthermia has a cytotoxic effect on cells and the highest heat sensitivity is observed during the mitotic phase (M-phase). There is a great diversity of molecular mechanisms of cell death following hyperthermia after being exposed to temperature greater than 43^oC. Cells can develop thermotolerance against hyperthermic cell death. This thermotolerance might be attenuated under some conditions such as lowered intracellular pH and some forms of drug resistance [4].

Hyperthermia temperature over 42^oC have some special features in tissue and cells *in vivo* that induce alterations of tumor blood flow and tumor micro environment. Hyperthermia enhances the cytotoxicity of various antineoplastic agents (thermal chemosentization). Hyperthermia also has effects on the cell membranes, cytoskeleton, cellular proteins, nucleic acids, and cellular immune response.

1.2 The breast cancer

Breast cancer is the most prevalent cancer among women and affects approximately one million women worldwide. In the United States, among women, breast cancer is the most common malignancy diagnosed and the second leading cause of death from the cancer. Breast cancer accounts for 30 percent of all female cancers in the UK and approximately 1 in 9 women in the UK will get breast cancer sometime during their life (http://www.who.int). Of all women diagnosed with breast cancer, 20% have locally advanced breast cancer (LABC). Women with locally advanced cancer of the breast who are exposed to standard treatments experience a 5 year survival rate of 50%, and this rate declines to 30% after 10 years. The treatment of the disease depends on the tumour type and the stage of disease – how far the cancer has spread to involve either lymph glands or other organs in the body. There are various ways a cancer can be staged and classified. Stages or classifications of breast cancer are divided into three groups (http://www.breastcancersource.com/): Early or operable breast cancer, Locally advanced breast cancer and Advanced breast cancer.

1.2.1 Early or operable breast cancer

Early breast cancer refers to cancer that is confined to the breast and/or the lymph glands in the axilla (arm pit) on the same side of the body. At this stage, the tumor size is usually smaller than 2 *cm*. The stage tumor can be removed by the surgery

1.2.2 Locally advanced breast cancer

Locally advanced breast cancer has spread beyond the breast and axillary lymph glands and involves the skin or the chest wall of the breast. These cancers tend to have a worse outlook than early breast cancer and are usually best initially treated by drug therapy or radiotherapy rather than surgery. In locally advanced breast cancer, the skin of the breast can either be directly involved by cancer or it is swollen or red. These changes occur because cancer cells enter the fluid channels that drain the breast (lymphatics) and block them, which causes the skin of the breast to be swollen and look like the skin of an orange. Locally advanced breast cancers were initially treated with surgery but this treatment was successful in only about 30 percent of patients. In the remainder, the cancer recurred in the areas immediately next to where the surgery was performed

1.2.3 Advanced breast cancer

In this statge, breast cancer has spread beyond the breast to other parts or organs of the human body such as lymph glands in the neck, bone, lungs, liver and even in brain.

1.3 The RF/Microwave modality for hyperthermia

Radio frequency (RF) radiation is one of the most versatile hyperthermia modalities; absorption of the electromagnetic energy in tissue causes a temperature elevation. The spatial control of microwave and radio frequency systems is limited due to physics. At higher frequencies some control is possible but penetration depth is extremely limited; while at lower frequencies with high penetration depths, spatial control is limited due to the significant wavelength. The wavelength in the muscle tissue at 140 MHz is about 22 cm. RF phased arrays for hyperthermia are now commercially available at several institutions, such as BSD-2000 system. Currently, there are no commercial systems particular for breast cancer with external, radiative RF arrays. In order to obtain high performance of breast tumor treatment, RF arrays need to be placed around and close to the tumorous breast.

1.4 The ultrasound phased array modality for hyperthermia

Ultrasound has numerous applications in medicine including ultrasound imaging and therapy. The therapeutical applications of ultrasound includes high intensity focused ultrasound (HIFU) and ultrasound hyperthermia. These applications are based on the absorption of acoustic wave. HIFU usually heats the tissue heated over 50^oC and destructs the tumor cells directly. In ultrasound hyperthermia treatment, tissue is usually heated to temperature between 41~45^oC for 30~120 mins.

Among different ultrasound therapy system, the ultrasound array system utilize electronic and/or geometric focusing to increase the intensity gain and improve the penetration depth. Ultrasound systems generate precise focal spots, usually much smaller than ordinary tumor dimension (Hunt, 1990). To expand the heated region, mechanical scanning or electronic scanning are utilized to improve the tumor coverage. But ultrasound phased array posses greater potential for improving the heating performance(Hynynen and Lulu 1990) than mechanical scanning. There are various ultrasound phased array prototypes including sector-vortex, N×N square, cylindrical section and spherical section.

The research in this dissertation is focus on computational simulations of breast cancer hyperthermia treatments of breast cancer with RF phase array and RF/US phased array applicator. The electromagnetic field distribution and properties are investigated to help the treament planning. The hybrid applicator, which combines RF modality and ultrasound modality togeter, takes advantage from both modalities and is proposed here to be the future clinical hyperthermia system. A new ultrasound focuing method, which combines sector-vortex method and phase delay method, is designed here for 2D planar array to generate large focus for ultraound heating purpose. This dissertation is organized into 9 chapters. Chapter 2 introduces the main simulation methods used in this whole dissertation. Chapters 3 and 4 describe the inestigation on electromagnetic field distribution and properties in four antenna RF applicator and five antenna RF applicator. Chapters 5 and 7 describe two designs of RF/US hybrid applicator. Chapter 6 discusses the new focusing method for planar array to generate large focus. A new type antenna is dicussed in Chapter 8, which can generate circular polarized wave in tumor region. Finally, Chapter 9 summarizes the conclusions drawn from this work and provides some suggestions for the future work.

CHAPTER 2

SIMULATION METHODS AND ROUTINES

Computer simulations and treatment planning routines require several computational procedures for field calculation and optimization. The field calculations simulate the eletromagnetic and ultrasound power depositions for each antenna or ultrasound element and optimization routines maximize the tumor heating by selecting the magnitude and phase for each channel. In this thesis, the finite element method (FEM) and the finite difference time domain (FDTD) method calculate the electric fields radiated by the antennas, the fast near field method (FNM) and angular spectrum approach (ASA) calculate the acoustic pressure field, and the bio-heat transfer equation computes the temperature distribution.

2.1 Electromagnetic numerical calculation

2.1.1 The Finite Element Method (FEM)

The finite element method is one of the most successful frequency domain computational methods for electromagnetic simulations. It combines geometrical adaptability and material generality for modeling arbitrary geometries and materials of any composition [6]. The latter is particularly important to current project since the human body is composed of fat, ribs, heart, lung, muscle, etc. which have different material properties; In addition, the applicator consists of copper antennas, a plastic enclosure, and water. The problem of electromagnetic analysis is actually a problem of solving a set of Maxwell's equations subject to boundary conditions. The electric field satisfies the vector wave equation with a differential form given by [7]:

$$\nabla \times \left(\frac{1}{\mu_r} \nabla \times \vec{E} \right) - k_0^2 \epsilon_r \vec{E} = 0 \tag{2.1}$$

Where $\overrightarrow{E}$ is the vector of the electric field, k_0 is the wave number in free space, μ_r is the relative permeability and ϵ_r is the relative permittivity. A boundary condition must also be specified for a unique solution. Boundary conditions include Dirichlet condition, Neumann condition, impedance condition, radiation condition and higher-order conditions. The principle of the FE method is to replace an entire continuous domain by a number of sub-domains in which the unknown function is represented by simple interpolation functions with unknown coefficients [7]. The system of equations is formulated by the Ritz method (a variational method) or the Galerkin's Method (a weighted residual method), the latter is presently more popular.

The finite element analysis includes the following basic steps:

1. Subdivision of the domain,

2. Selection of the interpolation functions,

3. Formulation of the system of equations,

4. Solution of the system of algebraic equations.

The radiation boundary condition is also essential in this problem. Because generating a mesh or grid in an infinite region is impossible, truncating the problem into a finite region is necessary, and the truncated boundary is the radiation boundary.

Most computations of the electric field (E-field) generated by radio-frequency (RF) electromagnetic devices designed for hyperthermia presently utilize either the finite difference time domain (FDTD) method [8] or the finite element method (FEM) [9, 10, 11]. The finite element method provides an advantage in E-field modeling by facilitating the geometric adaptability of the computational mesh. The finite element method solves the weak form of the vector wave equation [7]

$$\int_V [\frac{1}{\mu_r}(\nabla \times \mathbf{E}) \cdot (\nabla \times \mathbf{W}) - k_0^2 \epsilon_r \mathbf{E} \cdot \mathbf{W}] dV \tag{2.2}$$
$$= -\int_{S_0} \mathbf{W} \cdot (\hat{n} \times \nabla \times \mathbf{E}) dS - \int_V \mathbf{f} \cdot \mathbf{W} dV.$$

This expression describes the E-field throughout the volume V subject to a given set of boundary conditions on the surface S_0 enclosing the volume V. In Eq. 2.2, μ_r is the relative permeability, $\mathbf{W}$ is a weighting function, ϵ_r is the relative permittivity, k_0 is the wavenumber in free space, and $\mathbf{f}$ is the electromagnetic source function given by

$$\mathbf{f} = jk_0 Z_0 \mathbf{J} + \nabla \times (\frac{1}{\mu_r})\mathbf{M}. \tag{2.3}$$

In Eq. 2.3, Z_0 is the free space wave impedance, $\mathbf{J}$ is the electric current density, and $\mathbf{M}$ is the magnetic current density. The first item in the right hand side (RHS) of Eq. 2.2 is the boundary integral, which vanishes on a perfect electrical conductor (PEC). This term represents the absorbing boundary condition on a truncated surface for an open structure [7].

Finite element simulation results are generated by HFSS Version 8.0, which is a commercial software package produced by Ansoft Corp. (Pittsburgh, PA). In HFSS simulations of the electric field generated by the phased array applicator, the computational model consists of a three dimensional mesh of tetrahedral elements. HFSS provides a convenient interface for defining geometric structures and assigning material properties of each structure, then HFSS automates the generation of the mesh based on the structural properties of the overall system. In each tetrahedral element, the initial lengths of the edges are determined from the material properties, and the mesh is automatically refined based on the results of the computed E-field. The convenient user interface provided by HFSS allows an experienced operator to quickly define a new applicator structure and phantom geometry, generate the corresponding mesh, and solve for the resulting E-fields.

Finite element simulations of the phased array applicator truncate the boundary of the defined mesh with an absorbing boundary condition (ABC). The ABC for these simulations is implemented as a second order radiation boundary condition located in the air surrounding the outside of the applicator. In HFSS, the ABC elements are cuboid that surround the computational volume. The absorbing boundary is located roughly $\lambda/10$ away from the applicator, and since the antennas radiate primarily into the water tank, the E-field decays significantly before reaching the ABC. Results (not shown) were also obtained with an absorbing boundary located λ from the applicator. The difference between the computed fields obtained with the boundaries at $\lambda/10$ and λ is approximately 1.24%, therefore the distance from the water tank to the absorbing boundary is $\lambda/10$ for all simulations. By placing the ABC closer to the applicator, the size of the mesh is reduced, which in turn diminishes the computer memory requirements and the total computation time.

The E-field distribution is computed for each antenna separately, and then the results are superposed. The magnitude of the total E-field is computed according to

$$|\mathbf{E}(x, y, z)| = \left| \sum_{n=1}^{N} \mathbf{U}_n(x, y, z) I_n \right|, \tag{2.4}$$

where I_n is a complex number representing the amplitude and the phase of the n-th antenna input, and the vector $\mathbf{I}$ steers and focuses the E-field. In Eq. 8.2, $\mathbf{U}_n$ represents the electric field contribution produced by the n-th antenna for a unit input excitation (i.e., $I_n = 1\angle 0°$), $N = 4$ is the number of the antennas in the phased array applicator, $\mathbf{E}$ represents the total electric field, and (x, y, z) represents the Cartesian coordinates of the simulated E-field. In the simulation model, the voltage excitation is located in the center of the antenna, and each antenna input is modeled as a lumped gap source located at the center of each input port with an impedance of 50Ω. Once the 3D E-field is computed, the SAR is calculated from the amplitude of the total E-field according to

$$SAR(x,y,z) = \frac{\sigma(x,y,z)}{2\rho(x,y,z)} \left|\mathbf{E}(x,y,z)\right|^2, \tag{2.5}$$

where σ represents the conductivity and ρ represents the density for each tissue type.

2.1.2 Finite Difference in Time Domain (FDTD)

FDTD is another numerical method solving the Maxwell Equation. The FDTD method is a numerical solution for Maxwell's curl equations, which are based upon volumetric sampling of the unknown electric field and magnetic field within and surrounding the structure of interest over a period of time.

The FDTD method is efficient and accurate for electromagnetic wave interaction problems in unbounded regions. For our problems, and absorbing boundary condition (ABC) must be introduced at the outer lattice boundary to simulate the extension of the lattice to infinite. This is achieved for FDTD simulations by the perfectly matched layer(PML). Any plane waves of arbitrary incidence, polarization and frequency are matched at the boundary and are absorbed by the PML.

In this thesis, the E field propagations in and out of antenna in the time domain are calculated by the commercial software XFDTD (Remcom, Inc. State College, PA). XFDTD can handle 3D models of antennas and applicators, by subdividing these into equal-space meshes with 1 mm grid size (about 0.005 @ 140MHz in water) and automatically adding a PML boundary to the region of interest.

2.2 Ultrasound pressure calculation

2.2.1 The Fast near field method (FNM) for calculating pressure field

There are several different methods for calculating ultrasound fields generated by rectangle or circular piston. The most widely used approach for diagnostic imaging is the impulse response method derived by Oberhettinger and Stepanishen and Lockwood and Willette. This approach computes the pressure quickly but some numerical problems near the edge of the transducer. Other methods include the point source superposition methods (Zemanek) and the rectangular radiator method (Ocheltree). These two methods compute the field generated by circular and rectangular pistons by dividing these into small sub-elements. Both methods generate relatively large errors, and the computation times are relatively long.

The fast near field method (FNM) is derived directly from the impulse response method. The fast near field method eliminates the singularities that are produced by the impulse response method, thus the fast nearfield method (McGough) reduces the computation time and the peak normalized error.

2.2.2 Angular spectrum approach (ASA)

The angular spectrum approach computes acoustic pressures in a 3D volume in parallel planes. This approach is based on the theory that waves diffracted from finite apertures can be approximated by a sum of plane waves traveling in different directions [12]. The two dimensional (2D) Fourier transform decomposes the diffracted wave into transverse components, each of which has a vector angular frequency associated with the direction cosines. The ASA is essentially a Green's function approach that computes the field by multiplying the source and the Green's function (propagator) in the spectral domain. The accuracy and numerical efficiency of this method has been studied widely. For example, Christopher [13] described a ray theory truncation method to reduce the errors for radially symmetric fields. Wu[14, 15, 16, 17] discussed the optimal angular ranges in terms of the spatial aliasing errors.

The simulation stage often involves a large number of pressure field calculations, which are extremely time consuming using conventional analytical methods. However, much faster calculations can be achieved using the angular spectrum approach.

2.3 Thermal analysis

The temperature distribution is determined from the computed SAR distribution using the steady-state Bio-Heat Transfer Equation (BHTE) ,

$$0 = \kappa\nabla^2 T + c_b W_b (T - T_b) + SAR\rho. \tag{2.6}$$

In Equation 2.6, κ is the thermal conductivity (W/m/$°C$), T is the tissue temperature ($°C$), c_b is the specific heat of blood ($J/kg/°C$), W_b is the blood perfusion rate ($kg/m^3/s$), T_b is the temperature of blood ($°C$), σ is the electrical conductivity, SAR represents the specific absorption rate and $\rho$is the density of the tissue (kg/m^3). In these simulations, the steady-state finite difference solution of Eq. 2.6 is obtained for the resulting tissue temperature T. The finite difference calculations maintain the water surrounding the breast at a constant temperature, and a radiation boundary condition is enforced at the remaining interfaces. Subject to these boundary conditions, the finite difference model is evaluated within a computational grid that contains the entire 3D model of the breast depicted in Fig. Figure 8.3. The grid elements are cuboid, and each grid location contains SAR values obtained from the truncated finite element mesh defined for E-field calculations.

The temperature distribution is computed from the SAR distribution using the Bio-Heat Transfer Equation (BHTE). The static Pennes' bioheat equation (Eq.2.7) are given by:

$$\rho_p C_p \frac{dT}{dt} = \nabla(\kappa_p \nabla T) + C_b W_b (T_a - T) + SAR \cdot \rho_p \tag{2.7}$$

$$0 = \nabla(\kappa_p \nabla T) + C_b W_b (T_a - T) + SAR \cdot \rho_p \tag{2.8}$$

In Equation 2.8 and 2.7, T is the tissue temperature, t is the time, C_p is the tissue specific heat (J/kg/°C), κ_p is the tissue thermal conductivity (watt/m/°C), C_b is the specific heat of blood ($J/kg/°C$), W_b is the blood perfusion rate ($kg/m^3/s$), T_b is the temperature of blood (°C), ρ_p is the tissue density (kg/m^3), and SAR represents the specific absorption rate.

The final temperature can be computed with a steady-state finite difference method. The 3D discretization manipulation of Eq. 2.8 is shown in Eq. 2.9. In order to speed up the calculation, successive over-relaxation is utilized in the simulation. The time-varying temperature distribution can be calculated by the discretized form of Eq. 2.7 with it's discretization form in Eq. 2.10. Since the water is maintained a constant temperature, the thermal computational region is cuboid truncated from the FE region and this cuboid region contains the whole breast model and some water around the breast model. The six boundary faces of the cuboid region are set as a thermal radiation boundary condition for BHTE calculations.

$$\begin{aligned} T_{i,j,k}^{m+1} &= \frac{\kappa_p}{6\kappa_p + (\delta_x)^2 W_b C_b} \\ &\times \left(\frac{(\delta_x)^2 \rho_p}{\kappa_t} SAR_{i,j,k} + T_{i+1,j,k}^m + T_{i-1,j,k}^m + T_{i,j+1,k}^m + T_{i,j-1,k}^m + T_{i,j,k+1}^m + T_{i,j,k-1}^m \right) \end{aligned} \tag{2.9}$$

$$T_{i,j,k}^{n+1} = \left[1 - \frac{\delta_t W_b C_b}{\rho_p C_p} - \frac{6\delta_t \kappa_p}{\rho_p C_p \delta_x^2}\right] \times T_{i,j,k}^n + \frac{\delta_t}{C_p} SAR_{i,j,k} + \frac{\delta_t W_b C_b}{\rho_p C_p} T_b$$
$$+ \frac{\delta_t \kappa_p}{\rho_p C_p \delta_x^2} \left[T_{i+1,j,k}^n + T_{i-1,j,k}^n + T_{i,j+1,k}^n + T_{i,j-1,k}^n + T_{i,j,k+1}^n + T_{i,j,k-1}^n\right] \quad (2.10)$$

In these two equations, m indicates the iteration step, n is the time step, δ_x is the step in space, and δ_t is the time step. $T_{i,j,k}^m$ is the temperature at step m for the spatial point $[i \cdot \delta_x, j \cdot \delta_x, k \cdot \delta_x]$.

2.4 E-field calculation with HFSS

The FEM calculation of the E-field in the simulation model is performed by HFSS. Modeling the patient in HFSS is the most time-consuming step. The contours, which are extracted from MRI or CT images, are drawn in HFSS and connected into solids (by macro commands including *connect*, *coversheets*, and *stitch*). Sometimes the *connect* command does not work very well, when connecting two contours into a solid object, which is caused by the irregular point distribution along the contours. The average or maximum edge length of the mesh should be kept smaller than a tenth of a wavelength in that material. The lumped gap source is the power input for the antenna with the rectangular shape and the calibration line and impedance line are assigned inside the port and attached to the antenna. The external radiation boundary is ideally at least $\lambda/10$ from the antenna. After the E field is calculated, the result is exported to another program for thermal analysis.

2.5 Focusing strategy

The E-field is typically focused by optimizing the SAR [18, 2, 19, 20], and focusing is also achieved by directly optimizing the temperature [21]. Here, the phased array is focused by maximizing the constructive interference produced by the individual E-field components at a single point. A focus is generated when the magnitude squared of the total E-field

$$|\mathbf{E}|^2 = \sum_{m=1}^{4} \sum_{n=1}^{4} (\mathbf{U}_m I_m)(\mathbf{U}_n I_n)^* \tag{2.11}$$

is maximized relative to the sum of the squared input magnitudes $\sum_{n=1}^{4} |I_n|^2$. Defining the individual components of $\mathbf{E}$ through a matrix-vector product yields [21]

$$\begin{bmatrix} E^X \\ E^Y \\ E^Z \end{bmatrix} = \begin{bmatrix} U_1^X & U_2^X & U_3^X & U_4^X \\ U_1^Y & U_2^Y & U_3^Y & U_4^Y \\ U_1^Z & U_2^Z & U_3^Z & U_4^Z \end{bmatrix} \begin{bmatrix} I_1 \\ I_2 \\ I_3 \\ I_4 \end{bmatrix}, \tag{2.12}$$

which is equivalent to $\underline{\mathbf{E}} = \underline{\underline{\mathbf{U}}}\,\underline{\mathbf{I}}$, where a single underbar indicates a vector quantity and a double underbar indicates a matrix quantity. After this matrix-vector notation is applied to Eq. 2.11 and the result is normalized with respect to the sum of the squared input magnitudes $\langle \underline{\mathbf{I}}, \underline{\mathbf{I}} \rangle = \underline{\mathbf{I}}^{*t}\underline{\mathbf{I}}$, the optimization problem becomes

$$\max_{\underline{\mathbf{I}}} \frac{\langle \underline{\mathbf{E}}, \underline{\mathbf{E}} \rangle}{\langle \underline{\mathbf{I}}, \underline{\mathbf{I}} \rangle} = \max_{\underline{\mathbf{I}}} \frac{\underline{\mathbf{I}}^{*t} \underline{\underline{\mathbf{U}}}^{*t} \underline{\underline{\mathbf{U}}}\,\underline{\mathbf{I}}}{\underline{\mathbf{I}}^{*t}\underline{\mathbf{I}}}. \tag{2.13}$$

The extrema of the quadratic form in Eq. 2.13 are the eigenvalues of $\underline{\underline{\mathbf{U}}}^{*t}\underline{\underline{\mathbf{U}}}$, and the maximum value λ_{max} of Eq. 2.13 is achieved by the eigenvector $\underline{\mathbf{I}}_{max}$ of $\underline{\underline{\mathbf{U}}}^{*t}\underline{\underline{\mathbf{U}}}$ [21] that satisfies

$$\underline{\underline{\mathbf{U}}}^{*t}\underline{\underline{\mathbf{U}}}\,\underline{\mathbf{I}}_{max} = \lambda_{max}\underline{\mathbf{I}}_{max}. \tag{2.14}$$

The input $\underline{\mathbf{I}}_{max}$ maximizes the power deposition at a single coordinate in the tumor target. As a result, constructive interference is also achieved in nearby regions, and the surrounding tumor tissue is also heated. The optimal excitation vector $\underline{\mathbf{I}}_{max}$

is selected such that the peak power deposition is located within the tumor in a location proximal to the applicator. Focusing in this location reduces hot spots in normal tissues and other problems related to penetration depth.

The expression in Eq. 2.14 represents the optimal solution when the magnitudes and phases of the excitation are unconstrained. If the magnitudes of the entries in $\underline{\mathbf{I}}$ are specified in advance, then the expression in Eq. 2.11 is a nonlinear function of the phase variables $\arg(I_n) = \phi_n$. Defining the arguments of the antenna outputs for unit input excitations as $\arg\left(U_m^X\right) = \theta_m^X$, $\arg\left(U_m^Y\right) = \theta_m^Y$, and $\arg\left(U_m^Z\right) = \theta_m^Z$ yields an equivalent objective function

$$\sum_{n=1}^{2} \sum_{m=n+1}^{3} |I_n|\,|I_m| \left\{ \left|U_n^X\right| \left|U_m^X\right| \cos\left(\theta_n^X - \theta_m^X + \phi_n - \phi_m\right) \right.$$
$$+ \left|U_n^Y\right| \left|U_m^Y\right| \cos\left(\theta_n^Y - \theta_m^Y + \phi_n - \phi_m\right) + \left. \left|U_n^Z\right| \left|U_m^Z\right| \cos\left(\theta_n^Z - \theta_m^Z + \phi_n - \phi_m\right) \right\}$$
$$+ \sum_{n=1}^{3} |I_n|\,|I_4| \left\{ \left|U_n^X\right| \left|U_4^X\right| \cos\left(\theta_n^X - \theta_4^X + \phi_n\right) \right.$$
$$+ \left|U_n^Y\right| \left|U_4^Y\right| \cos\left(\theta_n^Y - \theta_4^Y + \phi_n\right) + \left. \left|U_n^Z\right| \left|U_4^Z\right| \cos\left(\theta_n^Z - \theta_4^Z + \phi_n\right) \right\} \quad (2.15)$$

when the reference phase for the fourth input is $\phi_4 = 0°$. The expression in Eq. 2.15 is readily maximized by iterative solvers such as the Matlab function *fminunc*, which quickly converges to the optimal values of ϕ_1, ϕ_2, and ϕ_3 that produce a global maximum. Solutions to both the linear and nonlinear objective functions in Eqs. 2.14 and 2.15, respectively, generate viable focal patterns for thermal therapy.

CHAPTER 3

FOUR CHANNEL RF PHASED ARRAY APPLICATOR

External heating devices appropriate for deep hyperthermia in the intact breast include ultrasound phased arrays [22] and radio-frequency (RF) electromagnetic phased arrays [23, 24, 25, 26]. Ultrasound is an appropriate local modality for heating small targets in the breast (up to about 2cm diameter [27]), whereas heat generated by RF electromagnetic devices is delivered regionally across a much larger area. RF phased arrays have been developed previously for deep hyperthermia in the pelvis [28] and in the extremities [29, 23], respectively. These arrays apply RF frequencies in the 60-140MHz range for increased penetration while delivering heat to deep targets. A microwave phased array system has also been constructed for thermal therapy in the breast [30]. The microwave phased array system requires breast compression because of the shallow penetration achieved at 915MHz.

To exploit the greater penetration depths afforded by RF applicators, a four-channel RF phased array applicator has been developed for hyperthermia cancer treatments in the intact breast. This phased array operates at 140MHz, which increases the penetration depth substantially over that achieved by microwaves. This RF phased array has been characterized with measurements of the electric field, and these measurements are consistent with the fields predicted by finite element simulations. Additional finite element and bio-heat transfer modeling results suggest that this array is capable of delivering therapeutic heat in an idealized model of the breast. These measurement and simulation results show that this RF phased array system can focus the electric field within a water tank and in simulated tumor targets in the breast.

3.1 RF phased array applicator and E field measurement system

3.1.1 Applicator geometry

A photograph of the prototype four-antenna RF phased array applicator is shown in Fig Figure 3.1. This design is an adaptation of previous cylindrical phased array geometries [31, 23], where only the portion of the array that directs RF energy to the breast is retained. The applicator consists of a water tank enclosure with four pairs of end-loaded dipole antennas mounted on the inner surface of the water tank. The tank enclosure consists of 6 solid Lexan (GE Polymerland, North America: www.gepolymerland.com) side panels and a Lexan top piece with a large opening. RF antennas are mounted on four of the rectangular side panels, and the two remaining side panels are irregular pentagons with one axis of symmetry. The four rectangular side panels are 12.8cm by 21.5cm, and the pentagonal side panels are 12.8cm by 12.8cm by 12.8cm by 12.8cm by 33.2cm. In each pentagonal side panel, the obtuse angle measured at the lowest point on the tank is 112°, the two obtuse angles measured at adjacent vertices are 153°, and the two remaining acute angles are 61°. Each Lexan panel is approximately 5mm thick. The top opening is 33.2cm by 20.5cm, the overall size of the tank enclosure in the x, y, and z directions is 21.5cm by 33.8cm by 18.4cm, respectively. For electric field measurements and patient treatments, the water tank is filled with deionized water.

The RF phased array applicator consists of four end-loaded dipole antennas that are composed of attached segments of 0.03mm thick copper foil [23]. This antenna geometry forms a transmission line with the two horizontal segments, and these in turn guide the RF energy to the vertical sections. For each of the antennas shown in Fig. Figure 3.1, the RF voltage input is applied at the center of the end-loaded dipole. Impedance matching is implemented with a coaxial cable stub, so each antenna is driven at 140MHz with a low return loss.

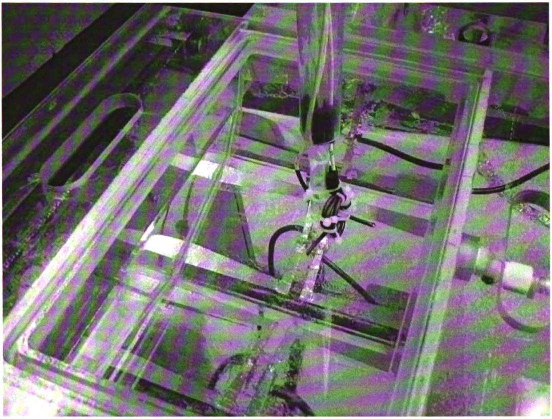

Figure 3.1. RF phased array prototype with four antennas designed for hyperthermia treatments in the intact breast.

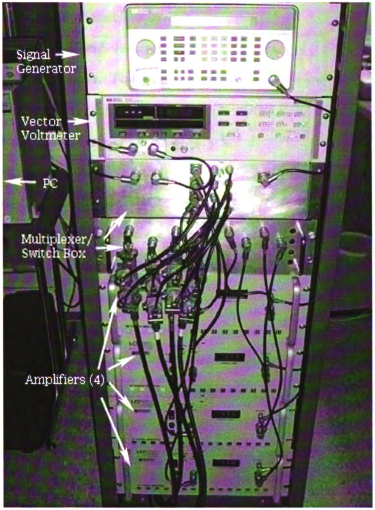

Figure 3.2. RF phased array amplifier system. This rack-mounted system consists of a signal generator, a vector voltmeter, a multiplexer/switch box, and four RF power amplifiers. The signal source generates a common excitation frequency for each of the amplifiers, the vector voltmeter provides phase and power feedback, and the multiplexer/switch box combination controls the inputs to the RF amplifiers. In turn, the RF amplifiers drive the individual antennas in the phased array applicator.

3.1.2 Amplifier system

The main components of the RF phased array amplifier system include a signal generator, a vector voltmeter, a multiplexer, a switch box, and four RF power amplifiers. The signal source for all channels is an HP (Palo Alto, CA) 8647A signal generator. An HP (Palo Alto, CA) 8508A vector voltmeter measures the output phase and power as well as the reflected power. These measurements deliver phase and power feedback to the controlling computer via GPIB. The multiplexer/switch box combination specifies the amplitude and phase of the input to the RF power amplifiers with analog attenuators and phase shifters through a Kontron (San Diego, CA) AOB6-P digital to analog converter (DAC) card that is installed in the controlling computer. The RF power amplifiers are LCF Enterprises (Post Falls, ID) model B020 rack-mount amplifier systems that operate in the 120-170MHz frequency range with a maximum power output of 150W. The output of each RF power amplifier is attached to a circulator, a low-pass filter, and a directional coupler that provides a direct connection to the antenna and a feedback connection to the vector voltmeter. The controlling computer is a Pentium II system with 128MB of RAM running the Windows 98 operating system, and the system control software is written in Visual Basic (Microsoft Corporation; Redmond, WA).

3.1.3 Measurement system

The electric field is measured with an E-field probe attached to a 3-axis positioning system. The measurement system hardware consists of 1) a LinTech (Monrovia, CA) M1-102412 3-axis positioning system, 2) three EP-400 E-field array probes from BSD Medical Corporation (Salt Lake City, UT), 3) an HP/Agilent (Palo Alto, CA) 34970A Data Acquisition/Switch Unit, 4) three Digiplan (Poole, Dorset, United Kingdom) PDX15 motor drivers (one for each axis), 5) a custom water degasser, and 6) a personal computer (PC). The E-field mapping software is controlled through a Matlab

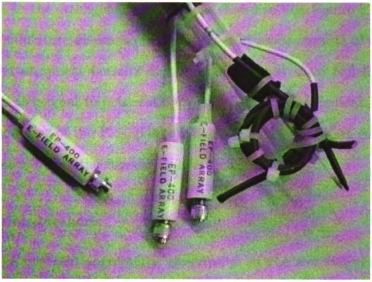

Figure 3.3. Three E-field array probes are attached to a Plexiglas rod for measurements of the electric field produced by the RF applicator. This probe arrangement is scanned across a rectilinear grid within the water tank by a computer-controlled positioning system. The measurements obtained with these scans characterize the E-field distribution generated by the RF phased array.

graphical user interface operating on a Windows 98 platform. Low-level interface routines are provided by the Matlab Instrument Control toolbox. The EP-400 E-field probes are connected to the HP 34970A, which transfers measured voltage values to the PC via GPIB. The stepper motor positioning system is controlled by the Digiplan motor drivers, and these communicate with the PC through a daisy-chained serial port connection.

The 3-axis probe combines three separate EP-400 E-field array probes attached to a Plexiglas rod in the orthogonal arrangement shown in Fig. Figure 3.3. Each probe contains three miniature diodes, so the 3-axis E-field probe consists of nine miniature diodes. This arrangement permits averaging of the individual E-field components, which improves the signal-to-noise ratio for each E-field measurement. Each probe is offset from the center of the Plexiglas rod, and the control software compensates for the offset distance before the signals are averaged.

3.2 Simulation Methods

Fig. Figure 3.4 contains a geometric description of the simulation model for the four antenna phased array applicator. In the finite element model, the size of the Lexan tank matches the dimensions of the prototype applicator. The Lexan tank is surrounded by air and filled with deionized water. In these simulations, the permittivity of Lexan is $\epsilon_r = 2.9$, the conductivity of Lexan is $\sigma = 0$, the relative permittivity of deionized water is $\epsilon_r = 76.5$, and the conductivity of deionized water is $\sigma = 0.0001 S/m$. The four end-loaded dipole antennas, which are attached to the Lexan tank, are copper strips excited by a lumped gap source. The resulting E-field is evaluated in the water tank and in a tissue phantom model suspended within the water tank.

The simulated tissue phantom in these finite element simulations is the simplified 3D breast model shown in Fig. Figure 3.5. This 3D model, which was in part

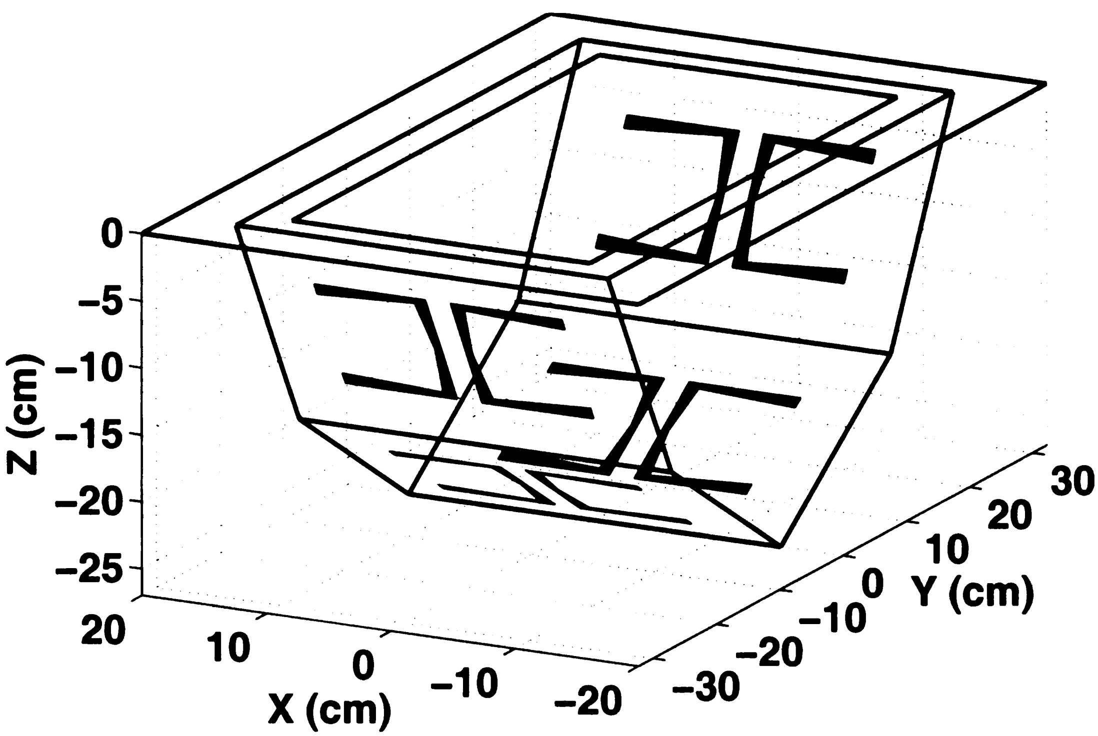

Figure 3.4. Simulation model for the four antenna RF phased array applicator. The geometric model, which has the same dimensions as the applicator in Fig. Figure 3.1, defines the input parameters for finite element simulations.

motivated by the axis-asymmetric model in [32], consists of an extended hemisphere and a spherical tumor mass that is offset somewhat with respect to the central axis of the breast model. The model in Fig. Figure 3.5 includes a skin layer, a fat layer, and a muscle layer. In Fig. Figure 3.5, the radius of the hemispherical breast is 7.5cm, the radius of the simulated tumor mass is 2.5cm, the thickness of the skin layer is 0.5 cm, the muscle layer is about 4.2cm thick, and the fat layer is 1cm thick. In this model, skin, breast, and fat share the same material property values [33]. The material properties for each tissue type are listed in Table Table 5.1. In FEM simulations, the applicator in Fig. Figure 3.4 is filled with deionized water, and the breast model is suspended in deionized water. The E-field is then computed in the breast and all surrounding regions, including the deionized water, the lexan tank, and the surrounding air space.

3.3 Results

3.3.1 E-field measurements in the water tank

The electric field is focused in the water tank with an appropriate selection of phases and amplitudes. A focus is generated by iteratively modifying the phase, and the combination of phase values that produce the maximum peak magnitude of the measured electric field in the desired location is selected as the input. This focusing approach is required because of the phase errors that are typically present in RF phased array systems [34]. These phase errors are in part caused by the unavoidable crosstalk between antennas that are coupled to a resonant cavity (the water tank) filled with low-loss material (deionized water) and in part caused by errors inherent in the controlling hardware [34]. After the desired combination of input phases and amplitudes is determined, the resulting E-field distribution is measured with the E-field probe depicted in Fig. Figure 3.3.

A focus was achieved in the center of the water tank with input phase settings of

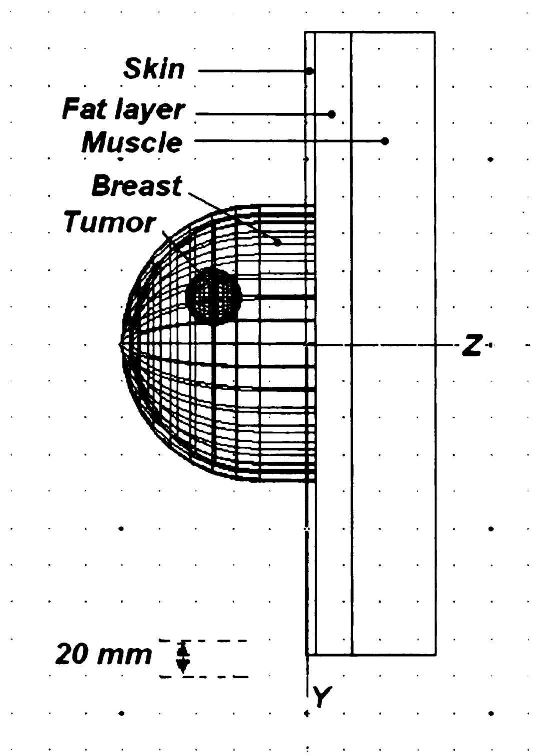

Figure 3.5. Schematic of the breast model defined for FEM simulations. The breast is modeled by a hemisphere with a 75mm radius, and a spherical tumor model with a 25mm radius is located inside the breast. The hemispherical breast model is attached to a 5mm thick skin layer, a 25mm thick fat layer, and a 42mm thick muscle layer.

$0°$, $-60°$, $-30°$, and $-90°$ applied to channels 1, 2, 3, and 4, respectively. Forward power settings of 40W were applied to each channel, and for the centered focus, the measured values of the reflected powers were 3.4W, 3.9W, 10.4W, and 1.7W for channels 1, 2, 3, and 4, respectively. The measured E-field distribution for the centered focus is shown in Fig. Figure 3.6. In each figure, the total E-field is the square root of the sum of the squares of the individual component magnitudes. The measured E-field values in Fig. Figure 3.6 are indicated by a star ('*') symbol, and the intermediate values indicated by dashed lines are obtained from the results of cubic spline interpolation. Fig. Figure 3.6a contains the measured E-field along the x-axis, Fig. Figure 3.6b shows the measured E-field along the y-axis, and Fig. Figure 3.6c demonstrates the measured E-field along the z-axis. Figs. Figure 3.6a and Figure 3.6b show that the desired peak is located near the center of the water tank. Fig. Figure 3.6c indicates that the maximum measured value along the z-axis is located $3cm$ below the water surface and the minimum measured value is located $12cm$ below the water surface.

A steered focus was generated in the water tank with input power values of 50W for channels 1 and 2 and 25W for channels 3 and 4. The phase settings for the steered focus were $0°$, $0°$, $-130°$, and $-130°$ and the measured reflected powers were 65W, 9W, 0.4W, and 14W for channels 1, 2, 3, and 4, respectively. These reflected power values emphasize the need for circulators in the amplifier system while indicating that focusing is preferentially achieved in the center of the water tank. The measured E-field distribution is shown in Fig. Figure 3.7a, which shows that the peak is located at $(0, 4, -3)cm$.

3.3.2 E-field simulations in the water tank

Simulation results for specified input settings are obtained by superposing the contributions from each antenna. In these simulations, the E-field is computed separately for each antenna using a common finite element mesh. This mesh is defined by the

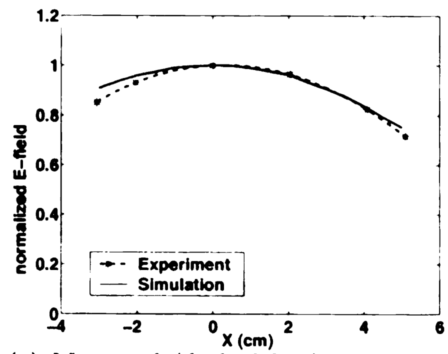

(a) Measured (dashed line) and simulated (solid line) E-field values in the water tank plotted with respect to the x coordinate where $y = 0$ and $z = -3cm$.

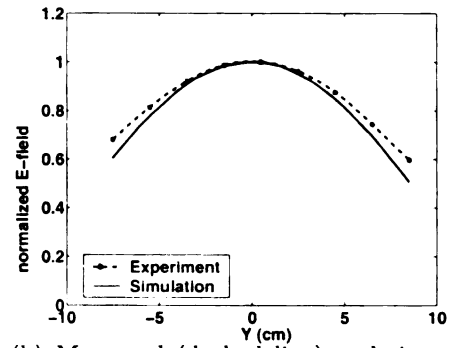

(b) Measured (dashed line) and simulated (solid line) E-field values in the water tank plotted with respect to the y coordinate where $x = 0$ and $z = -3cm$.

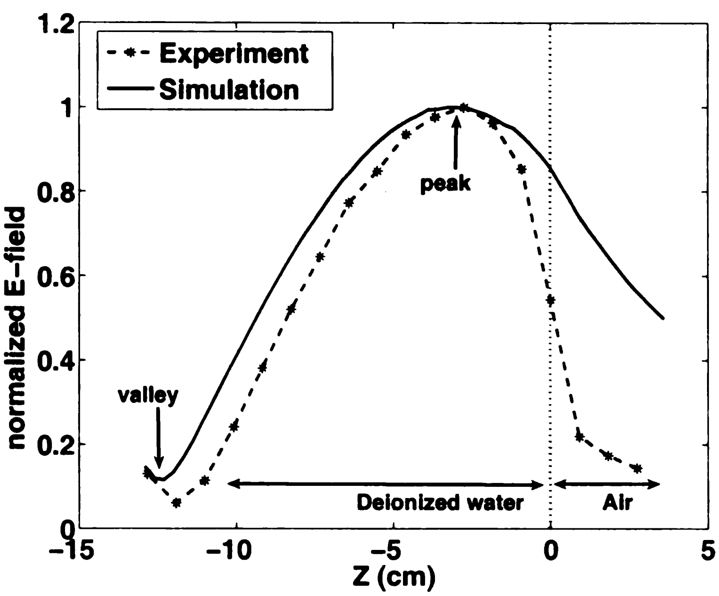

(c) Measured (dashed line) and simulated (solid line) E-field values in the water tank plotted with respect to the z coordinate where $x = 0$ and $y = 0cm$.

Figure 3.6. E-field distributions generated by the RF phased array depicted in Fig. Figure 3.1. The applicator prototype operates at 140MHz, producing a focus in the center of a tank filled with deionized water. The E-field measurements are performed by the apparatus depicted in Fig. Figure 3.1, and the E-field is computed with the finite element method for uniform phase and amplitude inputs.

model geometry and the material properties of water, Lexan, copper, and air, and for the breast model, material properties of different tissue types are also included. The finite element mesh is initially generated by HFSS and then automatically refined. Additional manual mesh manual refinement is applied as necessary near material interfaces, in regions where the electric field is changing rapidly, and in regions where node spacings are otherwise too large. After the mesh generation is completed, the average distance between adjacent nodes is between $\lambda/10$ and $\lambda/75$, depending on the model geometry and material properties, with higher node densities near radiating sources and material interfaces. The finite element mesh includes an absorbing boundary condition, where the shortest distance in air from the edge of the water tank to the absorbing boundary is $20cm$ in the x-direction, $18cm$ in the y-direction, $20cm$ measured from the top of the water tank in the z-direction, and $12cm$ measured from the bottom of the water tank in the z-direction.

A typical finite element simulation consists of an initial automated mesh generation, 11 automated mesh refinements, and one or more additional manual refinements resulting in a mesh containing up to 73,000 tetrahedra. After each mesh refinement, the E-field is computed with the finite element method using an edge element formulation. The computation time associated with this sequence of calculations is about 8 hours on a 2.4GHz Pentium 4 personal computer with 1GB RAM running the Windows XP operating system.

A simulated focus in the center of the water tank is generated with uniform power and phase inputs. The simulated inputs are normalized with respect to the peak input power, so the input power applied to each channel is 1W, and the phase value is 0° for each input channel, shown in Fig. Figure 3.8. The simulated E-field distribution for the centered focus is shown in Fig. Figure 3.6. Each plot is also normalized, which facilitates comparisons between simulated and measured values. The simulated E-field values in Fig. Figure 3.6 are indicated by solid lines, where Fig. Figure 3.6a contains the simulated E-field along the x-axis, Fig. Figure 3.6b shows the simulated E-field along the y-axis, and Fig. Figure 3.6c demonstrates the simulated E-field along the z-axis. Figs. Figure 3.6a and Figure 3.6b show that the simulated peak is again near the center of the water tank. Fig. Figure 3.6c indicates that the simulated peak value along the z-axis is also located about $3cm$ below the water surface.

The simulated focus is steered to the right with input powers of 0.5W, 0.5W, 1W, and 1W and input phases of $-87°$, $-91°$, $-66°$, and $0°$ applied to channels 1, 2, 3, and 4, respectively. The input power values in these simulations are proportional to the input powers that generated the measured E-field distribution depicted in Fig. Figure 3.7a, and the input phases maximize the objective function in Eq. 2.15 for a focus selected at $(0, 4, -3)cm$. This target represents the location of the peak E-field magnitude and the maximum constructive interference. The phases that generate this result were obtained from the solution to Eq. 2.15, which converged to the optimal solution after 170 iterations.

3.3.3 Breast model simulations

Simulations that combine the applicator model in Fig. Figure 3.4 with the breast tumor model in Fig. Figure 8.3 demonstrate an example of RF energy focused within a tumor target. In these simulations, the breast model is suspended in the water tank such that the skin layer indicated in Fig. Figure 3.5 is parallel to the flange on the top of the water tank, and then the breast model is centered within the opening on top of the tank. The E-field is focused on the tumor in the breast model with the solution to the eigenvalue problem in Eq. 2.14, and the resulting E-field, SAR, and temperature response are computed in 3D using the material properties in Table Table 5.1. The ABC boundaries for the breast model are the same as those defined earlier for E-field simulations in the water tank. These dimensions encompass the simulation model that combines the applicator in Fig. Figure 3.4 and the breast tumor model in Fig. Figure 3.5. After the E-field is computed, the SAR is calculated with Eq. 2.5. To reduce the

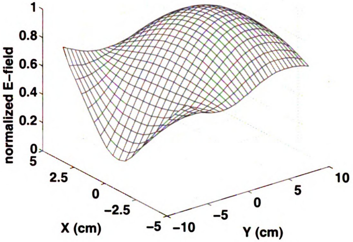

(a) Measured E-field for a steered focus.

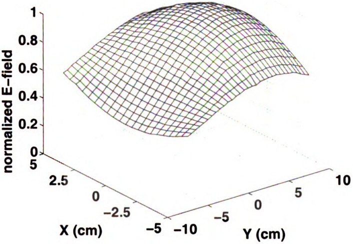

(b) Simulated E-field for a steered focus.

Figure 3.7. Examples of measured (a) and simulated (b) 140MHz E-fields in the xy plane achieved through electronic steering. Although some differences appear near the far corner of the grid, the shapes of these E-field meshes are quite similar, particularly in the region near the peak. In (a) and (b), the E-field is measured 3cm below the water surface (z = -3cm).

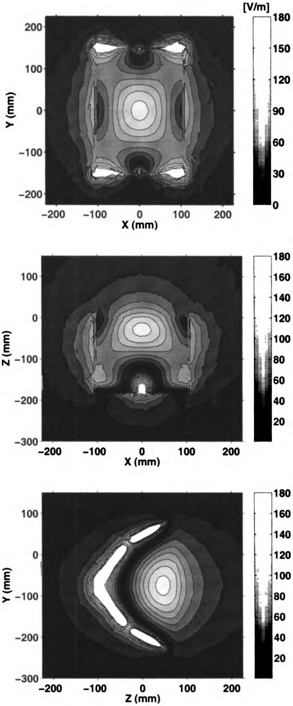

Figure 3.8. E field distribution in the water tank. the input power applied to each channel is 1W, and the phase value is 0° for each input channel. a) E field in xy plane with z = -3cm, b) E field in xz plane with y = 0cm and b) E field in yz plane with x = 0cm.

memory and time required for temperature calculations, SAR values are stored within a restricted volume that contains the entire breast and some connected soft tissues. For SAR and temperature calculations only, the x values are limited to the range from $-81mm$ to $81mm$, the y values are limited to the range from $-81mm$ to $81mm$, and the z values are limited to the range from $-110mm$ to $110mm$. Since there is very little penetration beyond the breast at 140MHz, the SAR distribution in these restricted coordinates produces approximately the same temperature distribution in the breast as the larger grid of SAR values in much less time. The temperatures in the breast are then calculated with a steady-state finite difference implementation of Eq. 2.6 that maintains a boundary condition of $39°C$ in the water tank, where this boundary condition simulates the effect of a circulating water bath during a patient treatment.

The results of these E-field, SAR, and temperature calculations are shown in Figs. Figure 3.9 and Figure 3.10 for a focus located at $(x, y, z) = (0, -15, -67)mm$, which is within the tumor model near the tumor boundary and proximal to the applicator. The computed values for the E-field, SAR, and temperature in Fig. Figure 3.9 are demonstrated in the central portion of the breast model evaluated in the $x = 0$ plane. The E-field, SAR, and temperature values in Fig. Figure 3.10 are evaluated in the $y = -16mm$ plane, where the peak SAR and temperature values occur. This plane is near the center of the spherical tumor model, which is located at $(x, y, z) = (0, -12, -50)mm$ in the applicator coordinate frame. The center of the breast is located at $(x, y) = (0, 0)mm$ in this coordinate frame, with the surface of the skin layer defined in Fig. Figure 8.3 coincident with the $z = 0$ plane.

The antenna phases that generate these results are $\theta_1 = 26.76°$, $\theta_2 = 72.4°$, $\theta_3 = 60.2°$, and $\theta_4 = 0.0°$, and the corresponding magnitudes of each excitation are $|I_1| = 0.65$, $|I_2| = 1.0$, $|I_3| = 0.85$, and $|I_4| = 0.57$. The E-field and SAR values are scaled such that the peak overall output temperature is equal to $43.6°C$. The computed fields shown in Figs. Figure 3.9 and Figure 3.10 are obtained after the scale factor is applied. Fig. Figure 3.9a shows that the largest E-field values in water are located near the individual antennas, whereas in tissue, the peak E-field values in the $x = 0$ plane are near the skin surface. In Fig. Figure 3.10a (which is orthogonal to the result shown in Fig. Figure 3.9a), the peak E-field values are located near the skin surface and in fat near the tumor interface. The corresponding SAR distributions are depicted in Figs. Figure 3.9b and Figure 3.10b. The computed SAR distributions indicate that multiplying the squared E-field by higher values of conductivity in the tumor model shifts the locations of some peaks into the tumor, although significant SAR contributions remain near the skin in Fig. Figure 3.9b and in fat near the tumor in Fig. Figure 3.10b. Overall, the computed temperatures in Figs. Figure 3.9c and Figure 3.10c follow trends similar to those established for the SAR distributions in Figs. Figure 3.9b and Figure 3.10b. In particular, the temperature peak occurs within the tumor model in Fig. Figure 3.9c, and the peak temperatures occur in fat near the tumor interface in Fig. Figure 3.10c. The overall temperature peak is $43.6°C$, which is achieved in Fig. Figure 3.10c at $(x, z) = (-27mm, -62mm)$ and $(x, z) = (27, -62mm)$. These simulation results demonstrate an example of the regional heating that is produced by this RF breast applicator. Although a focus is generated within the tumor, boundary conditions and material properties strongly influence the locations of the SAR and temperature peaks.

3.4 Discussion

3.4.1 Measured and simulated E-fields in the water tank

Figs. Figure 3.6 and Figure 3.7 show that finite element simulations predict the approximate shape and location of the focus generated by the RF phased array applicator. Figs. Figure 3.6a and Figure 3.6b demonstrate that, for a focus in the center of the water tank, the measured and simulated E-field distributions are closely

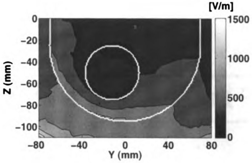

(a) Simulated E-field in the $x = 0$ plane.

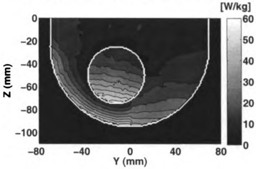

(b) Simulated SAR in the $x = 0$ plane.

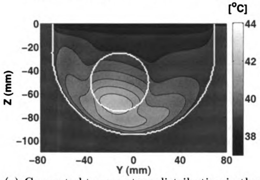

(c) Computed temperature distribution in the $x = 0$ plane. The peak temperature in this plane is $42.5°C$.

Figure 3.9. Simulated E-field, SAR, and temperature distributions generated by the RF phased array applicator and evaluated in the $x = 0$ plane of the breast tumor model, where the white contours indicate the external outlines of the breast and tumor. These simulation results show that, in the $x = 0$ plane, the E-field peaks in water are near the source antennas, the E-field peaks in tissue are near the skin surface, the peak SAR values are within the tumor model and near the skin surface, and the peak temperature in the $x = 0$ plane is within the tumor boundary.

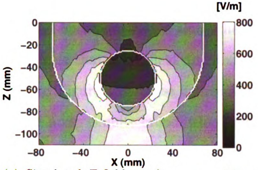

(a) Simulated E-field in the $y = -16mm$ plane.

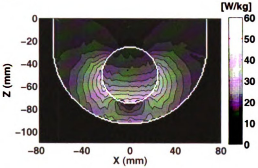

(b) Simulated SAR in the $y = -16mm$ plane.

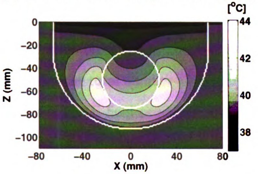

(c) Computed temperature distribution in the $y = -16mm$ plane. The peak temperature in this figure, which is also the peak overall temperature, is $43.6°C$.

Figure 3.10. Simulated E-field, SAR, and temperature distributions generated by the RF phased array applicator and evaluated in the $y = -16mm$ plane of the breast tumor model. In the $y = -16mm$ plane, E-field peaks in tissue appear in fat near the tumor interface, peak SAR values are in fat near the tumor interface and in the tumor proximal to the applicator, and the peak temperature in the $y = 0$ plane is located in fat near the tumor interface.

aligned along the x- and y-axes, respectively, for magnitudes evaluated at $z = -3cm$. Fig. Figure 3.6c also indicates that the finite element results successfully predict the locations of the minimum and maximum values along the z-axis. Likewise, simulations and measurements indicate that the E-field distributions are also similar for a steered focus as shown in Fig. Figure 3.7. These figures demonstrate that the focus generated by this RF phased array is quite broad, which suggests that this device is appropriate for regional heating.

Some differences between the measured and simulated E-field distributions are also evident in these figures. For example, simulated and measured values along the z-axis in Fig. Figure 3.6c diverge outside of the water tank. In particular, the measured E-field drops off rapidly in air beyond the water interface, whereas the simulated E-field decays slowly. Although the simulated E-field is similar to the measured E-field near the focus in Fig. Figure 3.7, the differences between simulated and measured E-fields increase with distance from the focal peak.

These differences are attributed to simulation and measurement errors. Finer meshes will reduce the numerical error where the E-field is changing rapidly, and memory limitations also restrict the total number of tetrahedrons in the finite element mesh. For these simulations of the E-field produced in the water tank, the average distance between adjacent nodes is 0.0306λ in air, 0.0134λ in lexan, and 0.05λ in water. Nodes in the finite element mesh are more closely spaced near interfaces, where the E-field changes rapidly, and where the magnitude of the E-field is relatively large, whereas the distance between adjacent nodes increases where relatively small E-field magnitudes are changing slowly. The error is introduced by the absorbing boundary is relatively small, as indicated by simulations that compare results for absorbing boundaries located $\lambda/10$ and λ from the water tank. Errors in the tank dimensions, antenna dimensions, and antenna locations likewise contribute to errors in the numerical model.

Errors are also introduced by misalignment between the simulation model and the measurement grid. Another source of error is the inherent misalignment between the three E-field probes. These E-field probes were applied to each measurement, and then the results were averaged to improve the signal to noise ratio. The relative probe locations were carefully measured before and after these measurements; however, probe locations changed after the probes were repeatedly inserted into the water tank and extracted from the water tank. In addition, some coupling between the computer-controlled 3-axis positioning system and the RF applicator was observed during these measurements. As a result, the probes were mounted on a polycarbonate rod, which was then attached to the 3-axis positioner. Additional shielding was added as necessary. Although this reduced the noise somewhat, the coupling between the applicator and the positioner nevertheless persisted, and this coupling influenced the measurement results.

Coupling between antennas is also evident in these measurements. This coupling is in part caused by standing waves within the water tank. The standing wave pattern changes as the input phases and amplitudes are varied, which also changes the coupling between antennas. This coupling also changes depending on the load in the water tank. In particular, the coupling changes for different water levels and for different phantom materials placed in a plastic cup on the water surface. This coupling is responsible in part for the differences between the measured and simulated phase and amplitude settings required for a focus in the center of the tank and for a steered focus. These effects, which are commonly encountered in RF phased array systems designed for hyperthermia [?, 34, ?], are reduced by focusing the breast applicator in center of the water tank so that the reflected powers are minimized. This defines the location where preferential focusing is achieved for this RF phased array applicator.

3.4.2 Focusing strategy

The simulated focus was generated in the water tank and in the breast model with a modified version of an approach that was defined previously for temperature optimization [21]. This approach, which is similar to a method that focuses ultrasound therapy arrays [?], maximizes the gain from the aperture to the focus. Eqs. 2.14 and 2.15 provide an alternative to more complicated methods that maximize the total SAR in the entire tumor relative to the total SAR generated in normal tissues [35, 10, 19]. With this simplified focusing approach, the results presented in Figs. Figure 3.9 and Figure 3.10 are obtained for a focus that is generated along the edge of the tumor in a location that is proximal to the applicator. This location minimizes the path to the focus through the tumor, thus reducing the effects of penetration depth on the magnitude of the simulated focus. Similar results (not shown) are obtained for this applicator geometry and breast model with the optimization method outlined in [19]. With the focusing approach of Eqs. 2.14 and 2.15, additional optimization is facilitated through control of the focus and the total input power.

3.4.3 Simulated E-fields evaluated in the breast model

The simulation results depicted in Figs. Figure 3.9a and Figure 3.10a show the E-field within a restricted field of view for the 3D breast model. Although the E-field was computed for a much larger range of coordinate values, the E-field results are demonstrated in the restricted field of view for two reasons. First, these results follow the same range of coordinate values shown in Figs. Figure 3.9b and Figure 3.10b for the SAR and in Figs. Figure 3.9c and Figure 3.10c for the temperature. Plotting these results on the same axes promotes comparisons of the similarities and differences between the computed E-field, SAR, and temperature distributions. Second, restricting the field of view centers attention on the computed E-field in soft tissues. Including the fields near the antenna obscures the fine structure of the E-field distribution in soft tissues as demonstrated in Fig. Figure 3.9a, where the magnitude of the E-field immediately adjacent to the RF antennas is significantly greater than in soft tissue. In planes that avoid the near field of the individual source antennas, more detail is clearly evident, as demonstrated in Fig. Figure 3.10a. This figure, which reduces the dynamic range by roughly a factor of two relative to Fig. Figure 3.9a, shows the full range of computed values in the $y = -16cm$ plane. By restricting the range of coordinate values in this plot, the computed values in tumor and fat are emphasized.

For the computed E-field evaluated across the entire range of coordinate values (not shown), the largest magnitudes are generated near the antennas, and intermediate values are indicated in water and within the soft tissue target. These simulations also show that the E-field decays rapidly in air. This result suggests that the RF phased array applicator operates as a resonant cavity that produces standing waves within the coupling medium. These standing waves, which are manipulated by the phase and amplitude inputs of the RF phased array applicator, produce peaks and valleys as indicated in Fig. Figure 3.6. The peaks and valleys produced by the standing wave patterns are manipulated through scanning and focusing, and these standing wave patterns also influence the reflected powers that are measured at the antenna inputs. In order to avoid unfocused near field components, the breast is positioned some distance away from the individual antennas, preferably at or near the geometric focus of the resonant cavity. Although the E-field values are relatively small in air, these values also influence the computed field through the boundary conditions. Simulation results (not shown) indicate that the material behind the breast also influences the distribution of the E-field in the breast and in the water tank at 140MHz. This suggests a need for more detailed patient models in these simulations, which are presently under development. These simulation results also depend on the distance between adjacent nodes in the finite element mesh. In simulations of the E-field generated in the breast model, the average distance between adjacent nodes is 0.0466λ in air, 0.0213λ in lexan, 0.0852λ in water, 0.0701λ in fat, and 0.0311λ in the simulated tumor. As in previous simulations, the nodes are more closely spaced near interfaces, where the E-field changes rapidly, and where the magnitude of the E-field is relatively large, and the distance between adjacent nodes increases for relatively small E-field magnitudes that are changing slowly.

Figs. Figure 3.9a and Figure 3.10a show that peak magnitude of the E-field is located outside of the tumor boundary, and similar effects are also observed for peak SAR and temperature values. In Fig. Figure 3.9a, the peak magnitude of the E-field in water is located near one of the antennas, and the peak magnitude of the E-field in soft tissue is located just beneath the skin surface. In Fig. Figure 3.10a, peak E-field magnitudes are adjacent to the tumor boundary in fat. Although the constructive interference is maximized at the focus within the tumor, the magnitude of the E-field is significantly greater at the peak outside of the tumor in Fig. Figure 3.10a. This effect is a consequence of the boundary conditions at the tumor/fat interface and the orientation of the E-field generated by the RF phased array applicator. This combination maximizes the E-field outside of the tumor model, and a severe impedance mismatch at the boundary reduces the peak magnitude of the E-field within the tumor target.

A similar trend is observed for the SAR distribution in each plane. In Fig. Figure 3.9b, the peak SAR value within the tumor is approximately the same as the peak SAR value located just beneath the skin surface. In Fig. Figure 3.10b, the peak SAR within the tumor also approaches the peak SAR achieved along the tumor boundary. Thus, multiplying the magnitude squared E-field values increases the relative contribution to the SAR within the spherical tumor model.

Peak temperatures follow the trend of the SAR away from the skin surface, which is maintained at $39°C$ by the circulating water bath. A water bath temperature above body temperature is afforded by the 140MHz excitation frequency and large aperture of the RF phased array applicator. This combination achieves heating within the breast without overheating the skin; therefore, skin cooling is not required for this system. In Fig. Figure 3.9c, a peak temperature of $42.5°C$ is indicated within the tumor model. However, a larger peak temperatures of $43.6°C$ is encountered outside of the tumor model in Fig. Figure 3.10c. Although the E-field is focused within the spherical tumor model and SAR results show that the peak SAR value in the tumor model is comparable to the peak SAR outside of the tumor, the overall peak temperatures in the breast tumor model are nevertheless generated in fat. These results demonstrate that the boundary conditions, particularly the orientation of the E-field vector within the breast and tumor regions, strongly influence the resulting temperature distribution. Other results (not shown) demonstrate that the peak temperature increases in fat and decreases in the tumor as the focus moves away from the applicator and deeper into the tumor. This suggests that the penetration depth, combined with an impedance mismatch at the fat/tumor boundary, strongly influences the ability of RF devices to heat deep tumors in the breast. The results shown in Figs. Figure 3.9 and Figure 3.10 also suggest that both SAR and temperature calculations are required for these evaluations. The heat generated along the tumor boundary is expected to contribute to regional heating in the breast, increasing the temperature of arterial blood and thereby improving the temperature distribution in the tumor. This result also demonstrates the need for noninvasive magnetic resonance (MR) thermometry [36] that provides valuable feedback for this regional heating device. Noninvasive thermometry will verify the temperature output generated by this RF phased array applicator, which changes based on the load that is presented to the applicator (i.e., for different patients). Temperature feedback will facilitate compensation for load changes and cross-coupling through phase and amplitude adjustments applied to the controlling amplifier outputs. This feedback will then enable targeted heating of breast tumors with this RF phased array device.

These results suggest that conformal heating of LABC tumors will be enhanced with an approach that incorporates an ultrasound (US) component within a hybrid RF/US phased array device. Measurement and simulation results show that the RF phased array is a regional heating device that heats a large portion of the intact breast, and adding local heat produced by an ultrasound phased array is expected to improve the temperature distribution in the distal portion of the tumor. The hybrid approach will exploit the regional heat generated by the RF applicator that increases the temperature of the arterial blood supply, and then the ultrasound component will locally raise the temperature as needed within the target volume. The existing RF phased array structure, which occupies four of the six flat panels in the lexan structure, is ideal for incorporating additional ultrasound applicators. Furthermore, the large heated region created by the RF phased array combined with the small focal spots generated by the ultrasound phased array provides multiple opportunities for optimization of the temperature distribution produced by hybrid RF/US phased array devices. This RF phased array design, which fills four lexan panels with end-loaded dipole antennas, is ideal for hybrid structures that incorporate additional ultrasound applicators into either of the remaining side panels. Other new geometries that populate fill all of the panels with end-loaded dipole antennas are also under development.

3.5 Conclusion

E-fields generated by a 4-channel RF phased array applicator designed for hyperthermia cancer therapy in the intact breast were measured in a tank filled with deionized water. This geometry was simulated with the finite element method, and the results indicate excellent agreement between the measured and simulated E-field magnitudes. The applicator generates a geometric focus in the center of the water tank, and measurements and simulations show that, through the selection of appropriate phases and amplitudes applied to each of the antennas, this focus can also be steered off-axis.

Some differences between the measured and simulated E-field magnitudes are evident in the geometric focus and the steered focus, and these are attributed to simulation errors and measurement errors. Overall, comparisons show that finite element simulations successfully predict the focal pattern generated by the RF phased array applicator within the water tank.

Finite element simulations were also evaluated in a simplified breast model that contains a spherical tumor volume. These simulations show that, although the RF phased array is focused within the spherical tumor model, the peak temperatures occur outside of the tumor. These temperature peaks, which are a consequence of the material properties of fat and tumor and the orientation of the incident E-field, are immediately adjacent to the tumor, so these peaks enhance regional heating generated by the RF phased array applicator. The simulated E-field, SAR, and temperature distributions suggest that this RF phased array applicator effectively generates effective regional heat for hyperthermia treatments of locally advanced breast cancer. Future evaluations of this RF phased array applicator will include realistic 3D anatomy derived from CT and/or MR images.

CHAPTER 4

THE FIVE RF DUAL-DIPOLE ANTENNA APPLICATOR

4.1 The five antenna MRI compatible applicator

In recent years, increased interest in thermal therapies, such as hyperthermia and thermal ablation, has occurred due to the ability of medical imaging techniques to guide the treatments. Imaging can be used to target diseased tissue, to visualize the heated area and to image the result after therapy. The use of imaging methods to measure temperature changes has been tested with ultrasound, CT and MRI. But the only currently available in *vivo* temperature imaging method is measuring the water proton resonant frequency (PRF) shift with MRI. So one key point of designing the thermal therapy applicator is MRI compatible and there is no electronic and electromagnetic interference between MRI and the therapy system.

A new MRI compatible applicator is designed and integrated with the MRI system (1.5T GE Signa Infinity with Excite magnet) to monitor the temperature distribution in the patient breast in real time. The whole system shown in Fig. Figure 4.1. To make the whole system compatible, there must be no electrical loops involved in the chamber of the MRI system and distort the RF signal and the magnetic field. Instead of the common used LC matching circuits, the single open-end transmission stub with length 22cm (one wavelength at 140 MHz) is used for impedance matching of each antenna and the connect point is at the feed point of the antenna.

The previous design of applicator is investigated in [37], four U-shaped antenna parallel mounted the inner side of the plastic tank. This applicator has limitation in two ways: one is that it lacks the ability to steer the focus in y direction (the coordinate is shown in Fig. Figure 4.2b) because all four antenna is in xz plane, the other limitation is E field linear polarization problem[38] which will cause hot spots

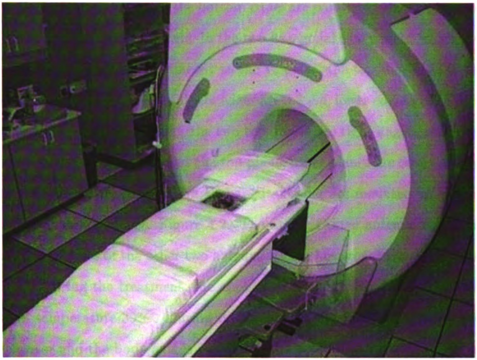

Figure 4.1. The thermal therapy applicator and MRI integrate system. The MRI compatible applicator is mounted in the bench. The patient lies on the bench with face down. This integrate system can heat patient and monitor the temperature distribution simultaneously.

in the E field direction (which will be explained in detail in later chapter). The new design of the five antenna applicator is shown in Fig. Figure 4.2. Four antennas are mounted around the breast and the fifth one is mounted on the bottom panel. With the arrangement of the antennas, the applicator can steer the focus in three dimensions.

The size of the top panel is about $33.6cm \times 22.5cm$. The bottom plane is $18.8cm \times 22.5cm$. Both the top panel and the bottom panel are parallel to the xy plane and the depth of the of the is about $12.0cm$. In the two hexagonal side panels, which are both parallel to the yz plane and symmetric to the xz plane, the top edge is 33.6 cm long, the bottom edge is 18.8 cm long, higher edges are 3.3 cm, lower edges are 15.3 cm, the two lowest obtuse angles are 150^o, the two top angles are right angles, and the other two obtuse angles are 120^o. Except the top plane, other planes are covered by plastic (Lexan) with $0.5cm$ thickness. Five U-shaped antenna are mounted on five sides of the applicator shown in Fig. Figure 4.2. The arms of three antenna are parallel to the y axis. The arms of the other two antenna on the hexagonal panel are parallel to the x axis. During the treatment, the applicator is filled with deionized water with a constant temperature 39^oC. During the treatment, the patient lies down prone to the applicator and the body axis is parallel to the y axis and there is 1-2 cm air gap between the chest wall and the water surface.

4.2 Phantom and Patient

In this chapter, several phantoms are made for testing and evaluating the applicator. The polyacrylamide gel (http://www.bergen.org/AAST/Projects/Gel/index.html) is made to mimic the breast fat tissue. The polyacrylamide gel is composed of 84% eucerin and 14% mineral oil. To reach the target material property[1], the dialectic property of the gel phantom is calibrated by adjusting the proportion of these two materials with the network analyzer[1]. The conductivity and permittivity of the

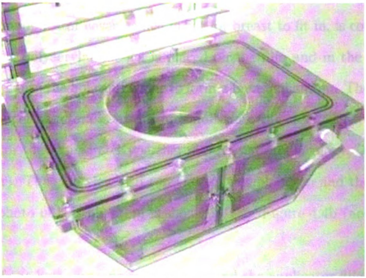

(a) Photo of the five antenna applicator

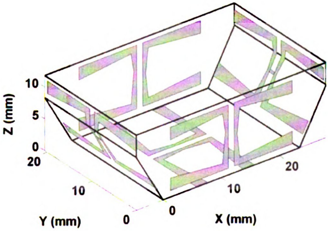

(b) Simulation model of the 5 antenna applicator

Figure 4.2. The five antenna applicator

tumor of breast cancer are similar to the muscle. The tumor phantom is a piece of beef steak is in the experiment.

4.2.1 Homogeneous Gel Phantom

The hole on the applicator cover, which is left for breast to fit in, is covered with soft plastic film; The polyacrylamide gel is placed on the film and in the hole; The film with the gel gets into the hole and water to form a breast phantom. The homogeneous polyacrylamide gel phantom is made to demonstrate the steering capabilities of the breast applicator (developed at Hyperthermia, Radiation Oncology, Duke University Medical Center). The side view and top view of this phantom and the film is shown Fig ?? and a photo of this phantom is shown in Fig. Figure 4.4b (not including the beef steak).

One slice of the homogeneous gel phantom and the applicator filled with water is shown in Fig Figure 4.3, which is under and close the water surface and the phantom is center circle in this MRI slice.

4.2.2 Fat/Tumor Heterogeneous Breast Phantom

The heterogeneous breast phantom is a two material model: fat-equivalent region and tumor-equivalent region. The tumor is surrounded by fat, which is common in Locally Advanced Breast Cancer (LABC). The location of the tumor in this phantom, indicated in Fig Figure 4.4a, is not at the center and about 2-4cm offset from the center. The tumor-equivalent phantom is a piece of steak with 4 cm length, shown in Fig. Figure 4.4b. Three temperature probes were inserted in the phantom (2 in tumor, 1 in fat) to monitor temperature change during heat up by applicator.

4.2.3 The patient and patient model

The applicator is mounted on the clinical bed, the top of the applicator is kept the same level at the surface of the bed shown in Fig.Figure 4.1 and the top of the applicator is covered with plastic cover with circle hole left open for patient breast.

Figure 4.3. Focus Steering in Homogeneous Gel Phantom

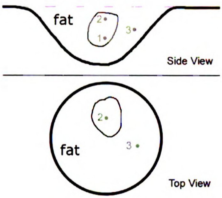

(a) Drawing of the breast phantom

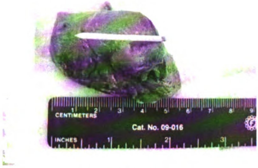

(b) Tumor phantom

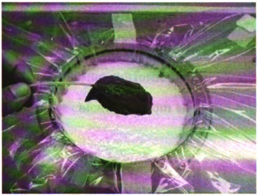
(c) Fat/tumor phantom

Figure 4.4. Tumor and fat phantom Fat/Tumor Heterogeneous Breast Phantom for breast. The size of the steak is about 5 cm

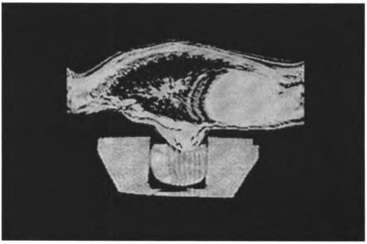

Figure 4.5. One slice of MRI images:patient with five antenna applicator.

The patient lies on the bed with face down and the breast with tumor is put into the applicator through the opening. The images of the patient and applicator are scanned by MRI scanner for treatment planning purpose before the treatment. During the treatment, the temperature distribution

4.3 Simulation model and method

The applicator, phantom and patient are modeled and E field is calculated with HFSS and exported in the region of interest (ROI). The total E field and the SAR are optimized to achieve good heating performance in desired region or tumor and temperature increased in ROI are calculated from the total SAR with BHTE equation

.

4.4 Simulation and Experiment Results

The amplifier and control system and the E field measurement system are the same as that for four antenna applicator in previous chapter. The measurement of E field in applicator was conducted without phantom and patient in water with E field probe and the positioning system outside the magnetic chamber. The temperature of the phantom is monitored with the applicator and phantom inside the MRI system. The temperature increase in three planes, which are picked by experience, are evaluated in every 2 mins by measuring the water PRFS.

4.4.1 E field and Focus steering in water

The E field is focused in the water tank with phases and amplitudes by the same method used in the previous chapter. A focus was achieved at the center of the water tank with input phase settings of 0°, -170°, -30°, -50°and 0°applied to channels 1, 2, 3, 4and 5, respectively. Forward power settings of 40W is applied to each channel, the measured reflected powers were 14.6W, 7.4W, 14.4W, 34.3W and 3.5W for channels 1, 2, 3, 4and 5, respectively. The measured E field distribution on the xy plane about 3 cm under the water surface is shown in Fig. Figure 4.6 and Fig. Figure 4.6 gives four different views of the mesh plot.

A back steered focus was generated in the water tank with input power value 50W for channel 1, 40W for channel 2 and 3 and 0W for channel 4 and 5 (in other words channel 4 and 5 are closed). Phases for five channels are 0°, -60°, 110°, 0°, 0° and the reflected power are 29W 25W 26W for channel 1, 2 and 3. The measured E field on the xy plane about 3 cm below the water is shown in Fig. Figure 4.7.

4.4.2 Focus Steering in Homogeneous Gel Phantom

The MRI-compatible breast applicator has also undergone extensive experimentation to demonstrate the control it has over the focus of heat. Here a homogeneous polyacrylamide gel phantom is used to demonstrate the steering capabilities of the breast applicator.The MRI coronal view of the polyacrylamide gel phantom with applicator is shown in Fig. Figure 4.3. Fig Figure 4.8 show temperature increase with different focus location in experiment and simulation.

Center focus heating is shown in Fig Figure 4.8 a and b. E field at the phantom

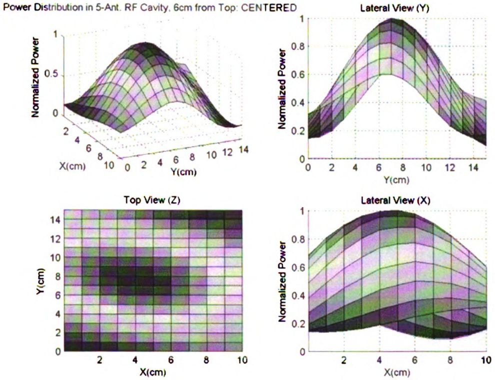

Figure 4.6. E field distribution in water and 3 cm below the water surface. The E field is focused at the center of the applicator.

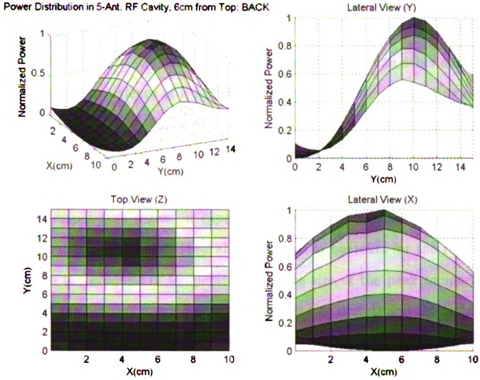

Figure 4.7. E field distribution in water and 3 cm below the water surface. The E field focus is steered to (y = 10cm) in the applicator.

center and 3cm below the top phantom surface is maximized with focusing strategy (in Chapter: Four antenna applicator) in the simulation. Because of phase errors present in RF phased array systems, the focusing and focus steering mainly depends on the E field focus experience in water. With the same combination of input phases and amplitudes as center focus in water, the temperature increase at center region of the phantom is observed which is indicated in Fig Figure 4.8a with a circle, while the around phantom region is lower temperature. The high temperature region in experiment and simulation have the same shape and the shape is not circle because two antenna parallel to yz plane are closer to the phantom than other antennas.

Based on the experience of E field focus steering in water, the heating region can be steered off the center, shown in Fig Figure 4.8c and e. With maximizing the E field at different location, the heating region can move to other location, shown in Fig Figure 4.8d with focus at [0,-5,-3]cm and Fig Figure 4.8f with focus at [5,0,-3]cm. The peak temperature region in experiment and simulation have similar contours for the bottom steering case. They also have similar contours for the right steering case. While the gradient of temperature and the size of the peak temperature are different for the bottom steering case (Fig Figure 4.8c and d) and the right steering case (Fig Figure 4.8e and f). The right steering case has smaller peak temperature region and higher temperature gradient than that in the bottom case, because two antenna parallel to yz plane are closer to the phantom than other antennas.

4.4.3 Heat Focus Steering in Fat / Tumor Heterogeneous Phantom

One slice MR image of the heterogeneous phantom with applicator is shown in Fig. Figure 4.9. The white region close the center of the phantom is the tumor phantom (beef steak) and dark region around the tumor is the gel phantom. Outside the gel phantom is water.

The temperature change in the phantom was recorded in three parallel planes with different depth. One of them is shown in Fig. Figure 4.10a at time turning

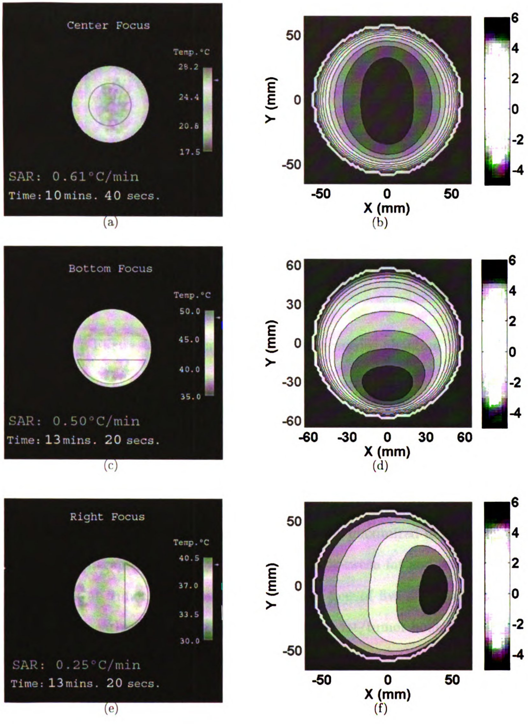

Figure 4.8. Focus steering in experiment and simulation

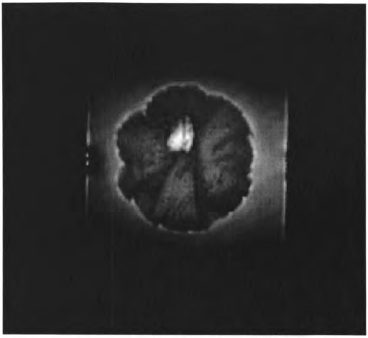

Figure 4.9. MR image of the heterogeneous phantom

off the applicator and temperature reaching the peak. In Fig.Figure 4.10a, the peak temperature distributes at the tumor/fat boundary and not inside the tumor, while some part of the tumor/fat boundary is not heated as much as that in temperature peak region. The same phenomena happens in simulation results. The same shape tumor in the breast model is simulated and E field is maximized in and around the tumor region. Because of the impedance mismatch between fat and tumor, E field is reflected back at tumor/fat boundary. Because of four of five antenna in xy plane, the E field is linearly polarized in xy plane and those fat/tumor boundary vertical to the polarization direction are prone to be well heated.

The temperature change in time domain is also studied in experiment and simulation. FigFigure 4.11a shows the measured temperature change at peak temperature region [3,2,-3]cm. and Fig Figure 4.11b shows the simulated temperature change at

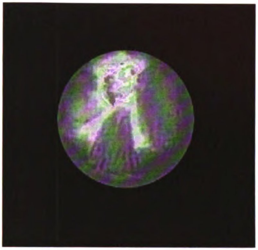

(a)

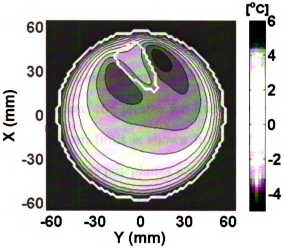

(b)

Figure 4.10. Heat Focus Steering in Fat / Tumor Heterogeneous Phantom

the same location. The applicator is turned on for 23 mins and then turned off after that. The curves match each other when the phantom cooling down, while simulated temperature increases faster than the measured temperature. It could be that air around the phantom takes away the heat, which is not counted in the simulation.

4.4.4 Heat the real 3D breast model

The 3D breast model, extracted from the patient MR images, is treated with the five antenna applicator in simulation. The electric field distribution in the breast model, water tank and air is calculated with HFSS and the E field for each antenna are calculated separately. The SAR and temperature are evaluated in $14cm \times 14cm \times 10cm$ region. The temperature is calculated from the electric field SAR with the static BHTE equation. The water is keep at 37^oC in all temperature calculation and the maximum temperature rise in the whole region is set as 6^oC. The material property and blood perfusion are shown in previous chapters. To deliver maximum power from the power amplifier, the power magnitude of each channel is usually the maximum available power. In the optimization, the magnitude for each channel is set unit 1 and only phases of five channel are optimized.

Without phase optimization, the phases for five channel are all 0. The temperature distribution with 44^oC up limit is shown in Fig. Figure 4.12. The SAR and temperature distributions in three cut planes are shown in Fig. Figure 4.13.

With the Wiersma method, The average SAR ratio (the average SAR in tumor to the average SAR in health tissue) is maximized and the optimized phases for five channels are 212^o, 108^o, 18^o, $-90^o$and 65^o. The temperature distribution with 44^oC up limit is shown in Fig. Figure 4.14. The SAR and temperature distributions in three cut planes are shown in Fig. Figure 4.15.

With the point phase method, the E field value at specified location [-2, 2, -5]cm is maximized and the optimized phases for five channels are -153^o, 146^o, 176^o, $17^o$and 0^o. The temperature distribution with 44^oC up limit is shown in Fig. Figure 4.16.

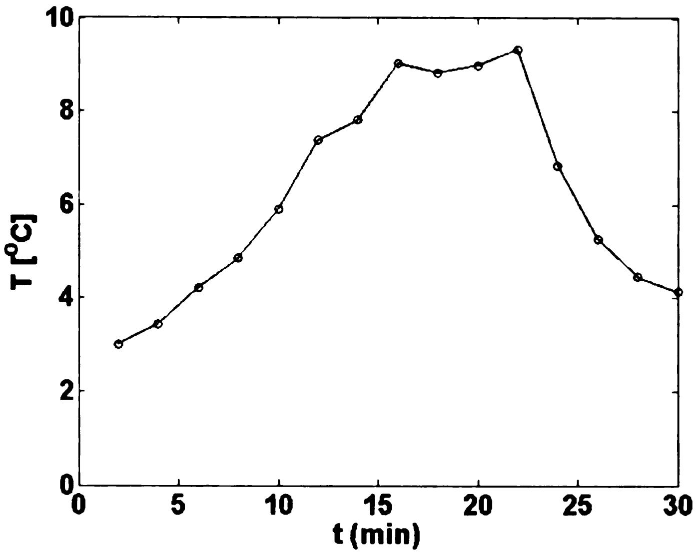

(a) Experiment result

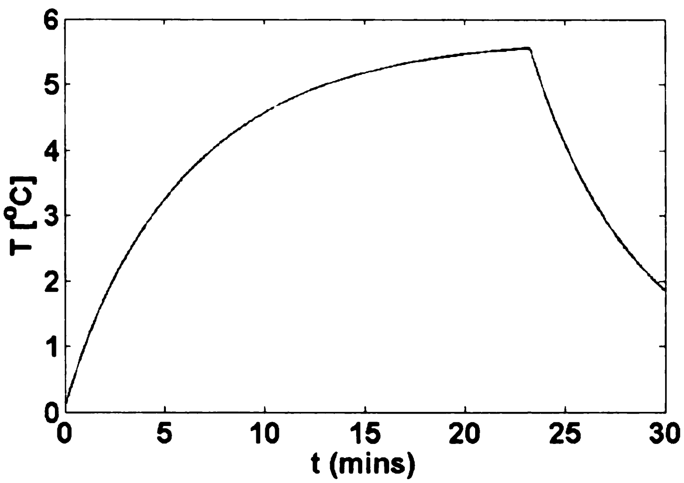

(b) Simulation result

Figure 4.11. Temperature varying with time at sample point

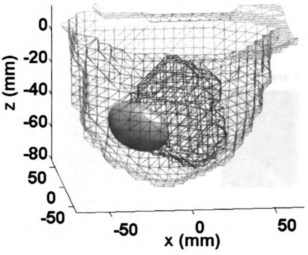

Figure 4.12. Temperature 3D distribution without optimization

The SAR and temperature distributions in three cut planes are shown in Fig. Figure 4.17. some other location, such as [0, 0, -5]cm and [-4, 4, -4]cm, are also optimized and the 3D temperature contours look similar to the contour in Fig. Figure 4.16.

4.5 Discussion

There exist a lot of sources of uncertainty that can occur in MRI-based temperature measurements, including noise, uncertainty in the baseline temperature, the effects of averaging the temperature over several MR voxels, uncertainty in the calibration of the PRF shift *in vivo,* drift of the static magnetic field, artifacts induced by motion or tissue swelling and the other reported errors in the temperature mapping. However, even with the uncertainties described above, a growing number of animal and clinical studies have been performed that demonstrated a good agreement between MRI temperature mapping and the heating results and showed MRI temperature mapping can be online control of thermal therapy and/or ablation.

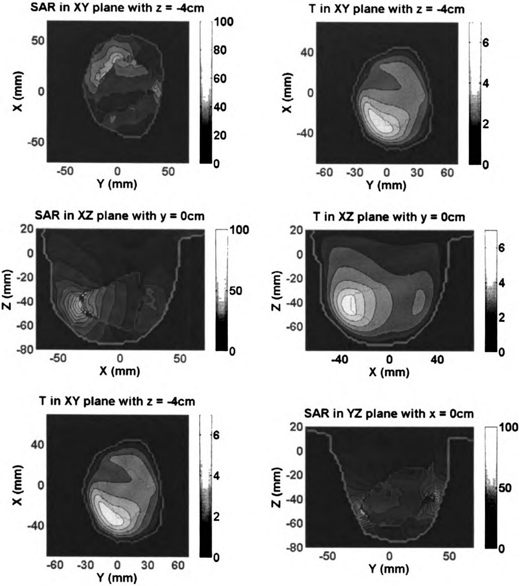

Figure 4.13. No optimization

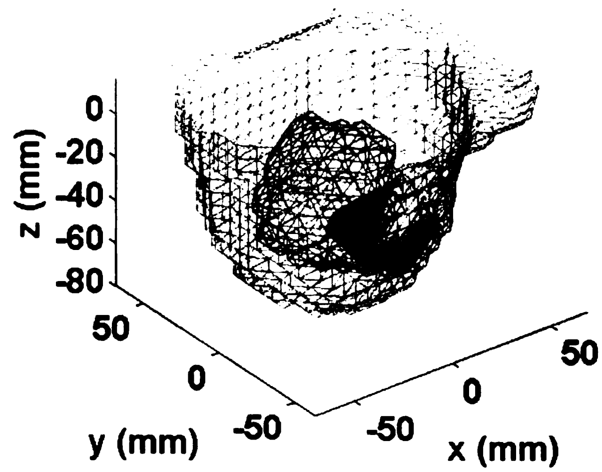

Figure 4.14. Temperature 3D distribution with the Wiersma method. The average SAR ratio (the average SAR in tumor to the average SAR in health tissue) is maximized and the optimized phases for five channels are 212^o, 108^o, 18^o, -90^{o}and 65^o.

In this hyperthermia MRI integration system, the RF applicator also disturb the B_1 field of the RF coil and it will also introduce artifact to the imaging although the RF frequency 140MHz is different from the Larmor frequency. The current RF coil is the single loop RF coil (transmitter and receiver) for breast imaging. The electromagnetic interference between the RF coil and the RF antenna will be an issue in this integrated system. The high power hyperthermia RF power could disturb the receiver of the RF coil and the metal surface of the RF coil could reflect and disturb the electric field distribution radiated by RF antenna array, which is not addressed by simulation. When MRI scanner are acquiring temperature mapping, the RF power of this applicator need to be blank to keep the receiver safety.

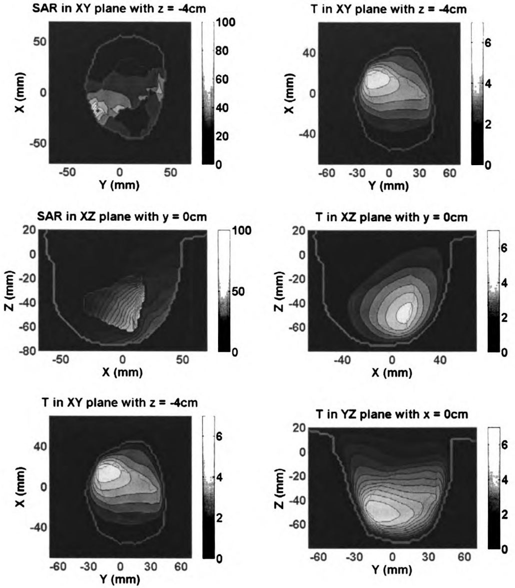

Figure 4.15. With the Wiersma method. The average SAR ratio (the average SAR in tumor to the average SAR in health tissue) is maximized and the optimized phases for five channels are 212^o, 108^o, 18^o, $-90^o$and 65^o.

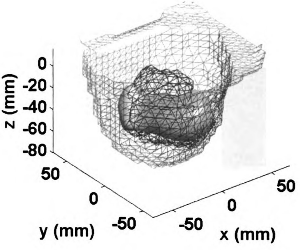

Figure 4.16. Temperature 3D distribution with the point phase method, the E field value at specified location [-2, 2, -5]cm is maximized and the optimized phases for five channels are -153^o, 146^o, 176^o, 17^{o}and 0^o.

4.5.1 Focus steering in water and homogeneous gel phantom

The four antenna in previous chapter can only steer the E field and SAR focus in xz plane (the cartesian coordinate system is shown in Fig. Figure 4.2b), while this five antenna applicator can steer the E field and SAR focus not only in the xz plane but also in the xy plane. Most of the tumor is not located at the center of the breast, so the steering ability in xy plane is necessary for breast applicator.

In Figs. Figure 4.6 and Figure 4.7, the size of the peak is about 6cm diameter in water. The wavelength in water is about 24cm at 140MHz and the size of the E field peak is about a quarter of the wavelength. In both figures, E field peak has more gradient along y direction, in other words E field is steeper along y direction. Comparing the peak center in Figs. Figure 4.6 and Figure 4.7, the E field peak moves about 5 cm along y direction.

By changing the five input magnitudes and phases, the E field and SAR can also

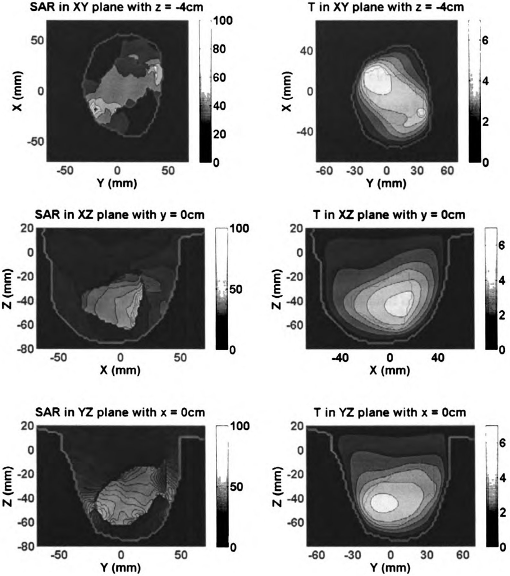

Figure 4.17. With the point phase method, the E field value at specified location [-2, 2, -5]cm is maximized and the optimized phases for five channels are -153^o, 146^o, 176^o, 17^{o}and 0^o.

be steered in the homogeneous gel phantom. Figs Figure 4.8 shows three steering case of MRI temperature mapping and simulated temperature distribution in about a plane about 3 cm below the water surface. These three case show great agreement between MRI measurement and simulation results. The center focus in Figs Figure 4.8a and b shows temperature peak is not a circle and the peak has an extension along y direction, because the two antenna on y axis are closer than that two in x axis. Comparing the bottom focus and right focus, the right focus has higher gradient in temperature, because the E field focus has the same trend in water

4.5.2 Heat focus steering in fat / tumor heterogeneous phantom

The fat/tumor heterogeneous phantom is the phantom model of breast with tumor. Fig. Figure 4.9 is one slice of the heterogeneous phantom and the tumor is in white color and around the white tumor is the fat in black-grey color. There are two gaps (in deep black) in the fat phantom below the tumor. This kind of gap does not exist in real breast. Because the single loop RF coil is used here, so only the region inside and close to the loop can be viewed, some region in water is imaged in bright color.

The thick line contours in Fig. Figure 4.9b shows the phantom simulation model in this plane about 3 cm under the water surface. The simulation model is drawn in HFSS according to the MRI images of the heterogeneous phantom and E field is maximized around the tumor region. Whatever the E field maximization location or power magnitude and phase for each channel are chosen, the peak temperature is outside the tumor region and close to the tumor/fat boundary in best case. This is also proven in the measurement with MRI temperature mapping. In Fig. Figure 4.9a, the left and right boundary of the tumor are best heated and heat transfers into the tumor region from the boundary until reaching the balance. The location of the temperature peaks on the boundary is determined by the E field polarization in tumor region, which will be talked in later chapters.

Temperature increasing with time are also monitored with MRI every two mins and simulated with BHTE with time term. The curves for peak temperature location are shown in Fig.Figure 4.11. With certain SAR level, both the simulation and experiment reach the peak temperature after 22~24mins after the power is on. After the power is turn off, the experiment and simulated curves go down with almost the same trend and gradient. But the experiment and simulated curves show a little bit different in the gradient of the temperature increase between time 0 mins and time 20 mins.

4.5.3 Heat the real 3D breast model

With the real 3D breast model extracted from MRI images (one of them is shown in Fig. Figure 4.5), the temperature simulation with some level optimization will be the treatment planning for breast cancer. Three different power inputs give huge difference on the final temperature distributions. Without any optimization method, each antenna has the same power level and zero phase and the temperature over 42^oC region is totally outside of the tumor. The Wiersma method maximizes the average tumor/normal SAR ratio and neglects the geometry shape of the tumor and breast. This method works well in a lot of cases, for example the simple breast model in previous chapter. However there could be a SAR peak with small size somewhere in the health tissue, which can be caused by the irregular tumor shape. The point maximization method works very well for this case and the temperature over 42^oC contour cover most of the tumor in Fig. Figure 4.16. The results are not sensitive to the location of the maximized point, for instance, the 3D temperature contours are almost the same with naked eye for points [0, 0, -5]cm [-2, 2, -5]cm and [-4, 4, -4]cm. The common character among these points are that they are all inside tumor and close to the tumor/fat boundary.

Different optimized magnitude and phase settings give different heating contour. Some tumor region heated in Fig. Figure 4.12, however, is not well heated in Fig. Figure 4.16. Even different point location in point maximization method can give different heating results. So combining those heating pattern in time sequence can give even better result than anyone individual. This topic will be talked in later chapters.

After the magnitudes and phases are chosen from treatment planning or optimization, the total E field inside breast and water is linear polarized in most of the case. If four of the five antennas except the bottom one is driven with phase 0^o,-90^o,$180^o$and 90^o individually, the E field inside the breast will be circular polarized and the SAR distribution around the tumor will be smoother than that with linear polarized settings. This topic will be talked in later chapters.

4.6 Conclusion

The only currently available in *vivo* temperature imaging method is measuring the water proton resonant frequency (PRF) shift with MRI. A new five dual-dipole antenna applicator is designed for hyperthermia treatment of breast cancer and integration with MRI system for treatment planning and online therapy guidance. E field inside the water tank without phantom was measured and simulated, there is E field focus at the center region of the applicator and the E field focus can be steered by changing the input magnitude and phase for five antenna. Temperature distribution of homogeneous gel phantom in one plane were measured by MRI scanner with five different focus locations and the simulated temperature distributions match the temperature map for the five focus locations. The fat/tumor heterogeneous phantom was made with gel and steak and also heated with this applicator with temperature monitor by MRI. The measured and simulated temperature both show the peak temperature region locating at the fat/tumor boundary and heat transfers into the tumor region from the boundary until reaching the balance. Simulation of the treatment on the patient shows treatment planning can dramatically improve the applicator heating performance on the tumor. The E field point maximization method gave better results than others and the results is robust with the point location selection.

CHAPTER 5

HYBRID RF/US PHASED ARRAY APPLICATOR (1)

5.1 Motivation

External ultrasound (US) phased arrays produce small focal spots while achieving high temperatures in deep-seated tumors, but these devices heat relatively small volumes. Ultrasound has good penetration in the ductile tissue in the breast because of almost no reflection on the tumor/normal tissue boundary and weak reflection on the water/tissue boundary. For heating breast regions, RF devices have limited penetration and temperature peaks are generated outside of the tumor[37] due to the reflection on the tumor/normal tissue boundary, which is caused by an impedance mismatch. Measurement and simulation results show that the RF phased array is a regional heating device that heats a large portion of the intact breast. Adding local heat produced by an ultrasound phased array is expected to improve the temperature distribution within the tumor. The hybrid approach will exploit the regional heat generated by the RF applicator that increases the temperature of the arterial blood supply, thereby reducing the power requirements for the ultrasound component. The large heated region created by the RF phased array combined with small focal spots generated by the ultrasound phased array provides multiple opportunities for optimization of the temperature distribution produced by hybrid RF/US phased array devices.

When these two modalities are combined, significantly improved temperature distributions are observed in simulated hyperthermia treatments of LABC. Power distributions are simulated for a hybrid applicator consisting of an RF phased array and a planar square US phased array, and temperature responses are evaluated for hyperthermia treatments in the intact breast. In this paper, a novel RF/US hybrid device is proposed for hyperthermia treatment of LABC. This device include a four-antenna RF phased array and a 2D planar US array with 5,000 circular elements. The simulation results suggest that this hybrid device deliver more therapeutic heat into tumor than RF device and US device used along.

5.2 Applicator and 3D patient model

5.2.1 Planar ultrasound phased array

The planar US phased array, driven by 1MHz time-harmonic excitation and mounted on the side panel of the hybrid applicator is shown in Fig. Figure 7.1. The planar phased array is square with 16.275 cm edge length wide and it comprises of 217×217 circular elements with radius $\lambda/4$. The center-center spacing between elements is $\lambda/2$. The compact structure of the array prevents the unwanted grating lobes which can cause hot spots in normal tissue. The acoustic pressure fields are computed on the grids sampled at a rate of $\lambda/2$. The distance from the center of the phased array to the center plane ($x - 0$) of the applicator is about 11 cm, the distance to the xy plane with ($z = 0$) is about 8.2 cm and there is no offset along y axis. The face of the US array is parallel to the yz plane and mounted inside of the applicator.

5.2.2 RF phased array and applicator

The design of the RF/US hybrid applicator is based on the RF applicator in [37]. The size of the top panel is about $33.6cm \times 22.5cm$. The bottom plane is $18.8cm \times 22.5cm$. Both the top panel and the bottom panel are parallel to the xy plane and the depth of the of the is about $17.0cm$. In the two hexagonal side panels, which are both parallel to the yz plane and symmetric to the xz plane, the top edge is 33.6 cm long, the bottom edge is 18.8 cm long, higher edges are 3.3 cm, lower edges are 15.3 cm, the two lowest obtuse angles are 150^o, the two top angles are right angles, and the other two obtuse angles are 120^o. Except the top plane, other planes are covered by plastic (Lexan) with $0.5cm$ thickness. Four U-shaped antenna are mounted on

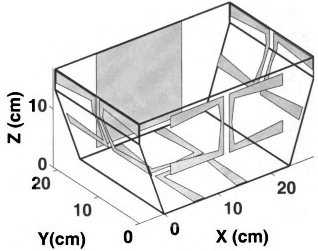

Figure 5.1. The hybrid applicator with 4 U-shaped antennas mounted on the four sides of the plastic tank, a planar ultrasound phased array mounted on a side panel.

four sides of the applicator shown in Fig. Figure 7.1. The arms of three antenna are parallel to the x axis. The arms of the fourth antenna on the hexagonal panel are parallel to the y axis. The planar ultrasound phased array is mounted on one hexagonal panel. During the treatment, the applicator is filled with deionized water with a constant temperature 39^oC. During the treatment, the patient lies down prone to the applicator and the body axis is parallel to the y axis and there is 1-2 cm air gap between the chest wall and the water surface.

5.2.3 Patient model

The 3D patient model is extracted from the MR images of the patients. The 3D model has two steps: 1) Extract the 2D contours for each organ or bone from every slice image via ct_con software. 2) Redraw these contours in HFSS and connect them into solids.

The program CT_con can manually extract tissue contours from medical images.

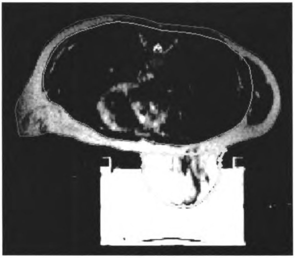

Figure 5.2. One slice of MRI images of the patient with contours. Those MR images were obtained when a patient lay prone to the hyperthermia applicator mounted in a medical couch. The contours are extracted manually with the Matlab based program 'CT_con'.

An example is given in Fig. Figure 5.2, which shows one MRI slice image with contours for breast and body. This MR image was obtained from a patient laying prone to the hyperthermia applicator (without US phased array) mounted in a medical couch. After all the contours were extracted, a 3D model was reconstructed in HFSS. This reconstruction is shown in Fig. Figure 7.4. The chest was included in this model, since the chest influences the E field distribution.

This 3D model includes tumor, breast, external layer of chest and inner chest. Different parts of the model are assigned different material listed in Table. Table 5.1. The tumor solid is assigned the tumor material. The breast is assigned the fat material. The external layer of chest is assigned the fat material, shown in Fig. Figure 5.2 in bright color. The inner chest is assigned the muscle material.

Table 5.1. Material properties for the breast model used in paper. The values of ϵ_r and σ are obtained from [1] and the values of c_p, κ, and W are obtained from [2].

	Fat	Muscle	Tumor
Relative Permittivity ϵ_r	20.4	75	65
Electrical Conductivity σ (S/m)	0.12	0.75	0.78
Specific Heat c_p $(J/kg/^\circ C)$	2387	3639	3639
Thermal Conductivity κ $(W/m/^\circ C)$	0.22	0.56	0.56
Blood Perfusion $W(kg/m^3/s)$	1.1	3.6	1.8

5.3 Methodology

5.3.1 Pressure field calculation and mode scanning techniques

Using a linear model, the total acoustic pressure field is the superposition of the pressure field of each element. Since the size and shape of the elements in the phased array are the same, the pressure field generated by elements are identical to each other. The pressure field generated by a single element source is calculated by combining the fast near-field method (FNM) [39] and the angular spectrum approach(ASA)[40, 16, 41]. Because of the equivalent sizes of the sampling grids and the array elements, the total field can be calculated by shifting and adding the field generated by the center element in a broader dimension. Due to the large number of elements and grid points, ASA is incorporated to accelerate the pressure field computation, since ASA utilizes FFT's to propagate acoustic fields. The pressure field at the first transverse plane is calculated by FNM and linearly propagated. Computational planes with a uniform size are slightly larger than the aperture (Zero padding eliminates circular convolution artifacts for short propagation distances, then the same effect is achieved by angular restriction for longer propagation distances). Both the array and the planes are normal to and centered at the z axis. The three dimensional field are calculated within an hour (Intel P4 2.4GHz CPU and 1GB memory) by using the combined simulation approach.

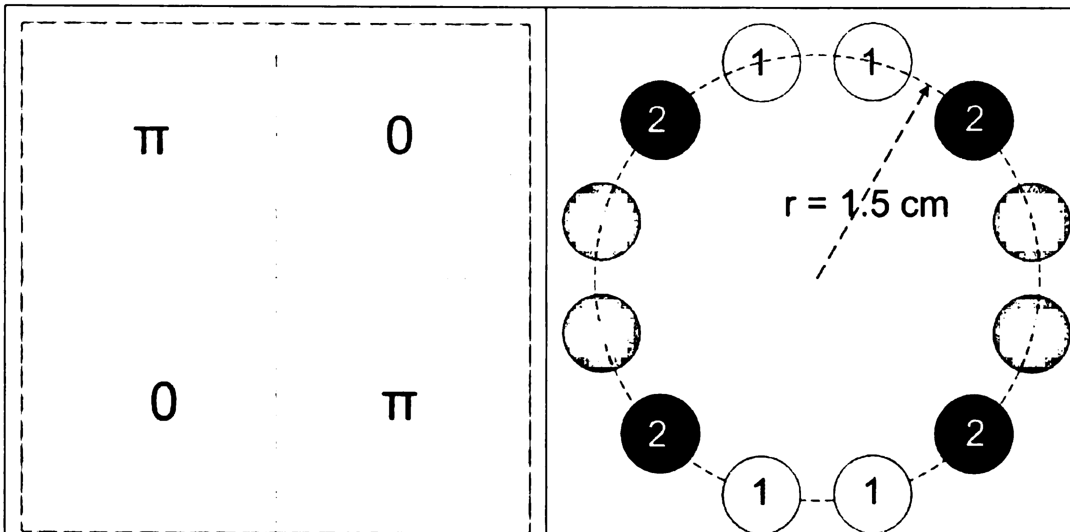

(a) Phase scheme for four focus mode scan with two cross phase symmetric planes

(b) 3 groups mode scan focusing in a circle with radius 1.5 cm

Figure 5.3. Phase a scheme for four focus mode scan and focusing strategy for planar ultrasound phased array

In order to reduce the intervening tissue heating, the mode scanning technique [42] cancels the fields in symmetric planes to reduce unwanted heat accumulated between the array and the tumor region. In the mode scanning technique, the US array is subdivided into the 4 regions shown in Fig. Figure 7.3a. Region I synthesizes a single focus at point (x,y,z). The driven phase distribution for the region II is symmetric to region I about y axis with 180^o phase difference and focus at (-x,y,z), region VI is symmetric to region I about x axis with 180^o phase difference and focus at (x,-y,z), and region III is symmetric to region I about center point and focus at (-x,-y,z). The array with four regions generates 4 focal spots and cancels the pressure field in the xz plane and the yz plane. Multi focus groups, shown in Fig. Figure 7.3b, can afford better heating pattern than single focus group. Three groups (with 12 focal points) are used in the present simulation.

After the 3D pressure field is computed, the steady state temperature field is simulated by solving BHTE equation using the SAR pressure as an input. The SAR generate by the pressure field is calculated by $SAR_P = \frac{\alpha}{\rho c}|P|^2$, where c is the velocity of the acoustic wave, ρ is the density and α is the acoustic attenuation coefficient.

5.3.2 E field computation

The E fields radiated by RF antenna are computed in the water tank and breast model by the commercial software HFSS (Version 8.0, Ansoft Corp, Pittsburgh, PA). The detail about setting up model and ABC boundary in HFSS is described in [37]. The ultrasound phase array is included in the E field calculation as the copper plate with the same size as the array. The E field distribution is computed for each separate antenna. The amplitude of the total E field can be computed from Eq. 5.1.

$$\vec{E}(\vec{r}) = \left|\sum_{i=1}^{N} A_i \exp(\varphi_i) \bullet \vec{E}_i(\vec{r})\right| \tag{5.1}$$

In this equation, A_i and φ_i are the amplitude and the phase of each antenna respectively, and N is the number of the antennas. Once the 3D E-field is computed, the SAR is calculated from the amplitude of the total E field, the electrical conductivity, and the density of the tissue according to $SAR_E = \frac{\sigma(\vec{r})}{2\rho(\vec{r})}\left|\vec{E}\right|^2$, where $\sigma(\vec{r})$ is the conductivity, $\rho(\vec{r})$is the density of the material, $\vec{r}$ is observation point.

5.3.3 SAR and Temperature Optimization

In this hybrid approach, the SAR generated by electric field and the temperature distribution produced by the total SAR (the sum of the SAR of E field and the SAR of pressure field) need to be optimized. The SAR generated by acoustic pressure field is optimized by the mode scanning technique. To optimize the SAR by RF source, one optimization method reported in [19] for optimizing SAR is easy to use. The matrices γ',η',γ,η are calculated from the E fields separately from 4 antenna and the computational detail is shown in [19]. All these four matrices are 4×4 matrix and not related with the excitation amplitudes and phases of the 4 antennas

$(A_1, A_2, A_3, A_4, \varphi_1, \varphi_2, \varphi_3, \varphi_4)$. The total SAR in the region of interest is a function of the four matrices and the antenna excitations. A Matlab function *fmincon* is used to minimize the ratio of the average SAR in normal tissue to the average SAR in tumor tissue.

There are several optimization methods[43, 44, 45, 18] to optimize the temperature distribution. There is no existing solution to optimize the SAR or temperature for RF/US hybrid source simultaneously. In this simulation, the weight of the total RF energy and the total US energy is optimized to minimized the temperature objective function. The temperature optimization function used here is in the same vein as those proposed in literature[46, 47, 48, 49, 50]. The objective is to achieve a specified tumor and normal tissue distribution: all points in tumor tissue at 43^oC, and all points in normal tissue at or below 42^oC.

5.4 Results

If the amplitude of power input of each antenna is set to unity and the phase is set to zero, there is an E field focus on the central axis of the water tank about 3 cm below the water surface where the patient breast is placed. Because of the patient motion and breathing, the positioning errors and that the tumor position is not exactly at the center region of the breast; therefore it is necessary to steer the amplitudes and phases for all the antennas to move the E field focus into the tumor region. *(Applicator focus and practical background)*

In the FE simulation, the E field is calculated in the whole 3D region inside the ABC boundary. The SAR and temperature are evaluated in a rectangular region with x from -8.0 cm to 8.0 cm, y from -8.0 cm to 8.0 cm and z from -10.0 cm to 0 cm on the 0.2 cm interval spacing. This region (16.0 cm$\times$16.0 cm$\times$10.0 cm) contains the breast, the tumor, a portion of skin and deionized water. The pressure field is only computed in this region specified above. Five faces of the rectangular region are in

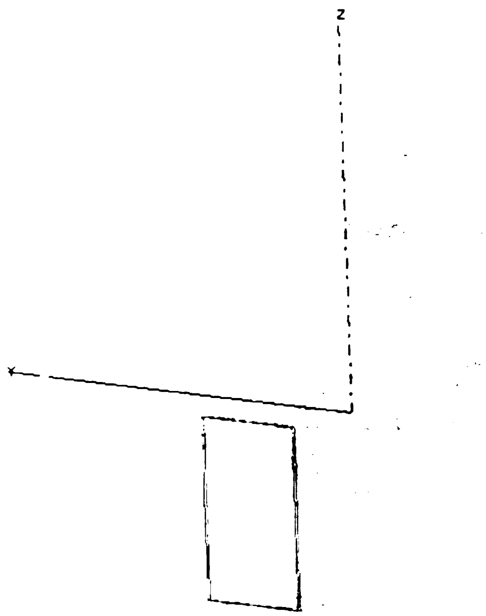

Figure 5.4. hybrid applicator including 4 RF antenna and US phased array

the water boundary and the top face of this region is located inside the body. During calculating the temperature, the five water boundaries are set at a fixed temperature (39^oC) and the sixth boundary is set as the body temperature (37^oC). *(Introduce the thermal region and temperature boundary)*

After the E field is calculated for each antenna, the SAR ratio (the average SAR inside tumor to the average SAR in the normal tissue) is maximized by the SAR optimization method. The power input magnitude for four channels are 1, 1, 1, 1 and the phase are 70.4^o, -63.8^o, 113.5^o, 0^o. The SAR ratio (E field only) is about 0.45. *(Give the detail of RF SAR optimization results)*

In order to reduce intervening tissue heating, ultrasound focal spots are placed at the distal half of the tumor. Here we assume the tumor is a sphere with 5 *cm* diameter. According to the model, the coordinate of the tumor center is around $(x, y, z) =$

$[2, 1, -3]cm$ and the center point of the US phased array is $(x, y, z) = [-11, 0, -8.2]cm$. The focal spots should be placed around the line which connect the center point of the array and the tumor center and in the half of tumor which is far from the US array. The center of the focus ring is selected manually $(x, y, z) = [3.5, 1, -4]cm$ which gives better heating performance for this hybrid applicator. *(Give the position of the array and the detail of ultrasound mode scan focusing)*

The results in the x = 0 plane and y = 1 cm plane are shown here and one more plane close to the tumor boundary in x direction is also shown here. Figures Figure 5.5, Figure 5.6, Figure 5.7 show the temperature distribution on the y = 0.5 cm plane. Figs. Figure 5.5 show the RF-only results and the E field is scaled with maximum temperature 44^oC with the SAR generated by E-field optimized with the Weisma SAR method[19]. Fig. Figure 5.5 shows the temperature distribution calculated from the RF-only SAR in this plane. In contrast with the RF-only result in the same plane (y = 10 mm), the US-only results are shown in the fig. Figure 5.6. The temperature distribution calculated from the US-only SAR with the same boundary is shown in Fig. Figure 5.6. In these results, the pressure field is scaled with maximum temperature 44^oC. The results on the same plane (y = 10 mm) with hybrid source are shown in Fig. Figure 5.7. Figures Figure 5.8, Figure 5.9, Figure 5.10 show the temperature distribution on the yz plane (x = 0). *(Introduce the view temperature results of RF only, US only and hybrid in two typical planes)*

Figures Figure 5.11, Figure 5.12, Figure 5.13 show the temperature distribution inside of the breast and tumor. The mesh grid indicates the tumor contour and the solid surface shows the isothermal surface. Fig. Figure 5.11 shows tumor model and the 3D view of the isothermal surface with temperature 42^oC with RF-only source which has the same power input and scale as Figs. Figure 5.5 and Figure 5.8. Fig. Figure 5.12 shows the 3D view of the isothermal surface with temperature 42^oC with US-only source which has the same power input and scale as Figs. Figure 5.6

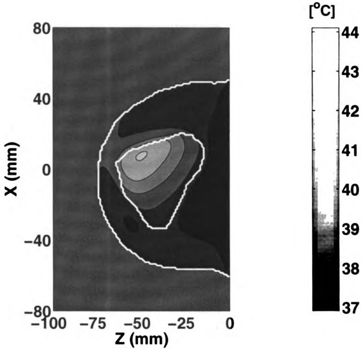

Figure 5.5. Temperature results in the xz plane (y = 10mm) with RF only

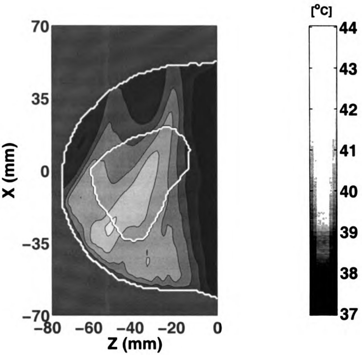

Figure 5.6. Temperature results in the xz plane (y = 10mm) with US only

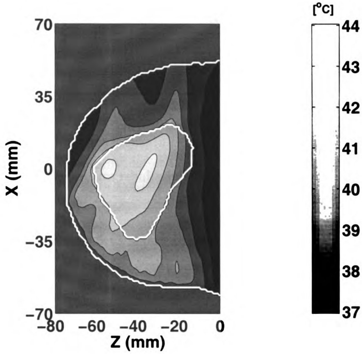

Figure 5.7. Temperature results in the xz plane (y = 10mm) with hybrid RF/US

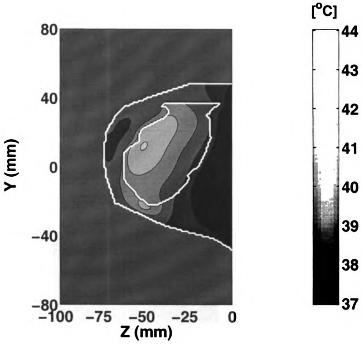

Figure 5.8. Temperature results in the yz plane (x = 0) with RF only

and Figure 5.9, Fig. Figure 5.13 shows the 3D view of the isothermal surface with temperature 42^oC with RF/US hybrid source which has the same power input and scale as Figs. Figure 5.7 and Figure 5.10. *(Introduce the 3D view of RF only, US only and hybrid temperature results)*

5.5 Discussion

The intact breast is placed at the geometric center of the phased array and the antennas are close and face toward the breast. The US phased array is mounted on the side wall, not the bottom wall of the tank. Because the acoustic pressure wave will be reflected by the ribs (acoustic impedance mismatch at bone/tissue boundary), which will cause pain to the patients, if the array is mounted at the bottom of the applicator and faces the patient body. This reflection will not occur if the array is

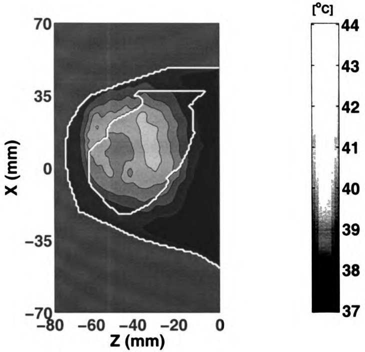

Figure 5.9. Temperature results in the yz plane (x = 0) with US only

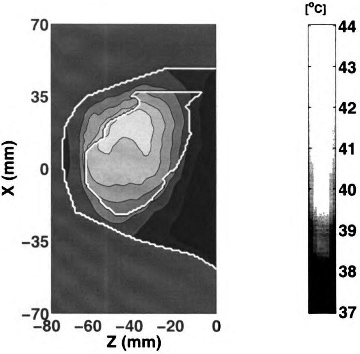

Figure 5.10. Temperature results in the yz plane (x = 0) with hybrid RF/US

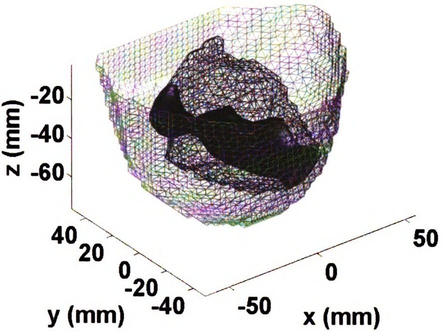

Figure 5.11. 3D view of the temperature distribution with optimized RF source only. The solid surface represents the 3D region over 42^oC temperature heating by the RF only. The external mesh contour is the tumor. The power input magnitude for four channels are 1, 1, 1, 1 and the phase are 70.4^o, -63.8^o, 113.5^o, 0^o. The SAR ratio (tumor/normal) is about 0.45.

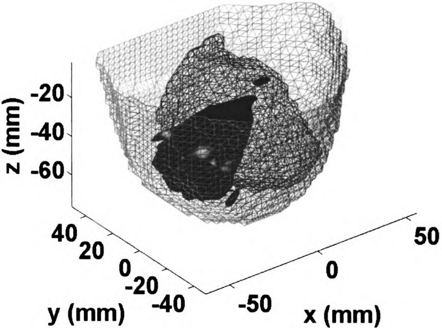

Figure 5.12. 3D view of the temperature distribution with only US source, the solid contour represents over 42^oC temperature contour.The external mesh contour is the tumor. The US phased array is located at$(x, y, z) = [-11, 0, -8.2]cm$; The center of the foci ring is at $(x, y, z) = [3.5, 1, -4]cm$.

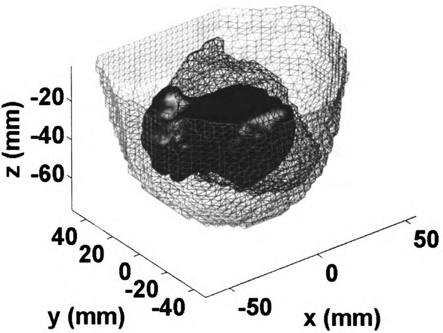

Figure 5.13. 3D view of the temperature distribution with RF/US hybrid source, the solid contour represents over 42^oC temperature contour and the external mesh contour is the tumor. The over 42^oC region covers more of the tumor region than that with ultrasound only and that with RF only. The total SAR of hybrid heating is the sum of 70.14% of the SAR by E field and 67.82% of the SAR by ultrasound pressure field.

mounted on the side wall of the tank. *(Explain why the array is mounted at the side wall of the tank)*

The parameters of the US phased array, such as element size, gap size and array size, are carefully chosen. Small array sizes have small window to deliver ultrasound power and the power density on the path to the target region will be high, which can cause intervening heating. Large element center to center spacing could cause severe grating lobes and the element size has stronger effect than the gap size. Small element center to center spacing has better performance, but it gives a large number of the element in the ultrasound phased array. *(Explain why picking these array parameters)*

The plastic tank and the deionized water are helpful to the focusing of the E field. Because the E field radiated by the antenna is reflected by the water/plastic boundary and the plastic/air boundary, so the E field inside of the tank will be much stronger than that without these boundaries. So the absorbing boundary condition can be move close to the FE model with low computational error. The field radiated by one antenna also is reflected by the metal surface of other antennae. Because of those boundaries (air/water, water/plastic) and reflections, standing waves exist inside of the applicator. Actually those standing waves have a dominant effect on the E field distribution. The overlapping E fields of those standing wave of the RF phased array generate the E field focus. One important advantage of this 4-antenna applicator is that the E field can focus close to the center of the water/air surface where the breast is located, compared with other applicator design (spherical shell, cylinder, etc). The shape and the material content of the chest does effect the E field distribution in the breast and the penetration depth into the chest wall. From the computed E field and SAR distribution, the power deposition in the chest wall is very low, because the E field decay very fast in the breast. *(Explain the design of the applicator and give the factors which effect the E field distribution)*

The E field and SAR inside breast and tumor, which are not shown here, change gradually and decay in the direction to the chest. These temperature in Figs. Figure 5.5, Figure 5.8 and Figure 5.11 indicate that E field by RF antenna array can heat the the proximal region of the tumor very well, the temperature peak is located inside of the tumor and close to the tumor/fat boundary. Most of the over 42^o region is inside the tumor, but the deep region (close to the chest wall) of tumor is not accessible by RF power. *(Talk about the heating performance by RF)*

Single-spot-focus scanning (multi-focus) approach can produce an optimal time-averaged absorbed power distribution for tumor heating. But the average intervening heating is also increased as the focus moves around and the power deposition at the focal points are still high which cause sharp temperature peaks there. Mode scanning cancels the pressure field in the phase symmetric planes, thus reducing the intervening heating and achieving low power deposition on the focal points (~1/4 of single spot focus power). Mode scanning techniques with 12 foci in this simulation are employed to heat tumors whose dimension are much larger than one single focus. In the temperature distribution in the Fig. Figure 5.6, the power deposition right on those foci are actually lower than the peak power deposition region which is located about 2 cm behind the foci ring (close to the US array) and is also clearly indicated in Fig. Figure 5.7. That is the reason that the foci are placed beyond the tumor region and inside normal tissue. In Fig. Figure 5.12, the shape of the over 42^oC regions heated by US power are not symmetric: the part in the tumor shrinks more than those outside the tumor, because of different blood perfusion. Although those foci outside of the tumor do not heat the tumor directly, they can elevate the temperature in the deep region of tumor. In this simulation, the upper limit of the temperature is set as 44^oC, which will alleviate the pain caused by thermal treatment. *(Talk about the heating performance by US)*

Although some of the over 42^oC region heating by US only is outside the tumor, the over 42^oC in the hybrid heating shown in the Fig. Figure 5.13 almost fills the whole region of the tumor. Comparing the temperature distribution by RF/US hybrid applicator with that of the RF only or US only, the over 42^oC temperature distribution by hybrid method covers not only the forepart of the tumor, but also the deep part of the tumor. The hybrid method decreases the total RF power and the hot spot temperature caused by the E field. The hybrid method also decreases the power deposition at the ultrasound foci and increases the size of the heating region with the 44^oC up temperature limit. *(Talk about the hybrid heating performance)*

5.6 Conclusions

The 3D FE model for the RF/US hybrid applicator was formulated. Also, the 3D patient models were extracted from the patient CT/MR images. The E field inside and outside of the applicator and inside of the patient model is obtained based on the FE model and the acoustic pressure field in the thermal model region was computed with a mode scan technique employed for US phased array heating strategy. The 3D temperature distribution is calculated in the thermal model based on BHTE. The SAR generated by E field is optimized and the weights of US power and RF power are also optimized to minimize the temperature objective function and keep the peak temperature lower than 44^oC. Comparisons between RF/US hybrid method and RF-only or US-only show that the hybrid heating strategy can heat the whole region of the LABC tumor better that US or RF alone.

CHAPTER 6

SECTOR-VORTEX SCANNING FOR A LARGE SQUARE US PHASED ARRAY APERTURE

6.1 Introduction

In previous chapters, the RF/US hybrid method is introduced and mode scan and imaging focus methods are used to generate pressure focus to heat the tumor. But There is still some disadvantage with those methods, such as the focus size is too small and peak is too sharp. In this chapter, the ultrasound focusing scheme for planar array is mainly talked about. How to achieve large heated region is one of the major problems for ultrasound hyperthermia.

Cain and Umemura [51, 52] proposed a rotating phase scheme ($\phi = M\theta$) for a concave sector-vortex ultrasound phased array applicator. This strategy generates a controllable ring-shaped pattern in the focal plane. In this approach, the total pressure field is approximated by an Mth-order Bessel function and the size of the focus (or the radius of the main lobe) in the focal plane is controlled by the mode number M. The sector-vortex array contains a small number of trapezoidal elements, and relative to square planar phased array structures populated with square elements, the sector-vortex array is difficult to build and calibrate. Although the focus size in the focal plane is adjustable with the sector-vortex array, the location of the focus is fixed and the size of the focus along the center axis is also not adjustable.

A large ultrasound phased array with 500 square elements was recently reported in [53]. With new PZT fabrication technology and circuit designs[54], the number of the elements in the ultrasound phased array for therapy could grow very large (~1,000 or even more) and the driving electronics system could become much more compact. The implementation of large phased arrays for hyperthermia could offer flexible control of the focus with a large scan angle while eliminating the formation of grating lobes. Furthermore, 2D planar arrays with square elements are readily available for thermal therapy applications.

A new phase scheme proposed herein can directly synthesize a controllable focus of pressure field for 2D planar square ultrasound array with square elements or circular elements. The shape of the focus generated by these large arrays approximates that generated by a concave sector-vortex array. In addition, the focus can be steered off the axis and/or along the axis and the size along the axis can also be controlled. In this paper, a prototype ultrasound phased array applicator for hyperthermia consisting of 73×73 square elements generates a broad focus in the target tumor region. Computer simulations of the ultrasound pressure fields generated by this array are calculated with the fast near-field method (FNM), and the resulting temperature distribution is computed with the bio-heat transfer equation (BHTE). Simulation results show that the combination of several modes can heat large tumors (with radius of 5 cm) with a broad, uniform temperature distribution.

6.2 Phasing Scheme

The ultrasound phase array is square planar array with $N \times N$ square elements. The square element has an edge length a and the gap between two element is b. The elements are arranged on the grid points shown in Fig. Figure 7.2. Each element with index (i, j) is driven by a sinusoidal signal with the phase for each channel ϕ_{ij} given by

$$\phi_{ij} = M\theta_{ij} - \alpha k d_{ij}^{f} \tag{6.1}$$

for $i = 1, 2, \cdots$, N and $j = 1, 2, \cdots$, N, where (i, j) is the index of the element, $\phi_{ij}$is the phase of the driven signal, θ_{ij} is the angle of the element center shown

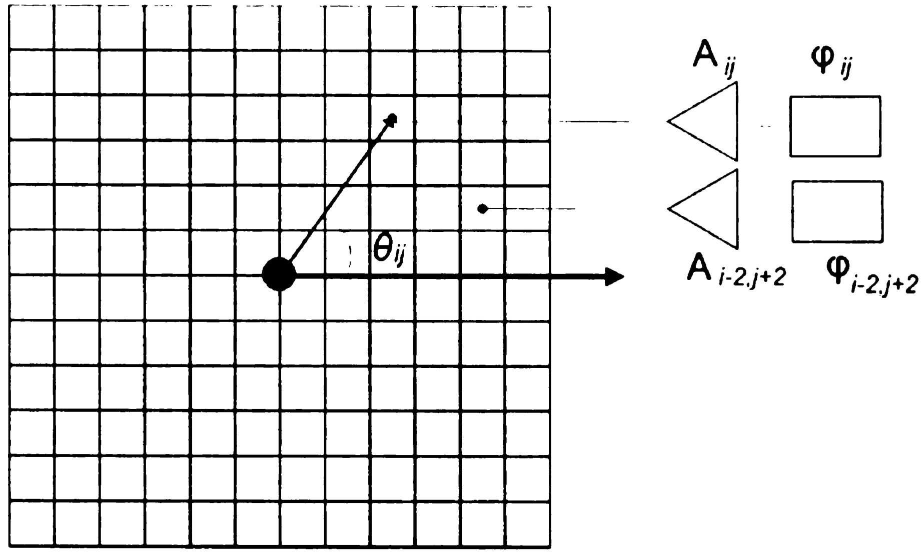

Figure 6.1. Schematics of planar array with rectangular element.

in Fig.Figure 7.2, M is the mode number, k is the wavenumber in water, α is the coefficient for focusing, d_{ij}^f is the distance from the element center to the focal point ($d_{ij}^f = \sqrt{(x_{ij} - x_f)^2 + (y_{ij} - y_f)^2 + z_f^2}$), (x_{ij}, y_{ij}) is the coordinate of the (i, j) element center, and (x_f, y_f, z_f) is the coordinate of the focus center. The first term (mode term) of Equation.7.1 shows that the phase on each element rotates $|M|$times per rotation around the center point of the array [51, 52].

The second term (focusing term) of Equation.7.1 works as a concave-converging acoustic lens shown in Fig. Figure 6.2. With this phase shift, the new wave front of the acoustic wave radiated by the array is a spherical shell and the spherical shell wave front converges to the focus specified by (x_i, y_i, z_i) shown in Fig. Figure 6.2a. With simply changing the location of the focus, the ultrasound focus can be steered off the center axis or steered along the axis shown in Fig. Figure 6.2a. The coefficient of the focusing term can control the extension of the focus along the center axis. Adjusting the α coefficients, the shape of the shifted wave front will be changed and the focus will extend or shrink along the center axis. When α equals one, the initial shifted wave front is spherical. Base on the focusing term, the mode term (the first term of Eq.7.1) modulates the pressure field distribution radiated by the phased array.

6.3 Methods

6.3.1 Pressure field calculation

The 3D pressure field radiated by one element is precisely calculated with unit magnitude is calculated by the fast near-field method[55]. The difference of the pressure field between any two elements are the complex amplitude and spatial shift. Once the pressure field by one element with unit magnitude driven signal is calculated as a sample pressure field, the pressure field by any other channel is the spatial-shifted sample pressure field times the complex amplitude. The total acoustic pressure field is the superposition of those pressure fields.

6.3.2 Patient model and thermal calculation

A cross section of the tumor model is shown in Fig.Figure 6.3. The material properties used in temperature calculation is listed in Table. Table 6.1. The tumor is a sphere with 4cm diameter, 6.2 cm deep from the skin and the center point of the tumor is at [0,0,6.2] cm. The thickness of the skin layer is 0.4 cm, the fat layer is 1.5 cm, the muscle layer is 1.5 cm and the viscera layer is 7.5 cm.

The temperature distribution is computed from the SAR distribution using the Bio-Heat Transfer Equation (BHTE). The final temperature can be computed with a steady-state finite difference method[56]. In order to accelerate the calculation, successive over-relaxation is utilized in the simulation[43]. Since the water is maintained a constant temperature, the thermal computational region is cuboid truncated from the FE region and this cuboid region contains the whole breast model and some water around the breast model. The six boundary faces of the cuboid region are set as constant temperature for BHTE, the top face of the thermal region, located in the body, is set as 37^oC and the other five faces are set as 39^oC.

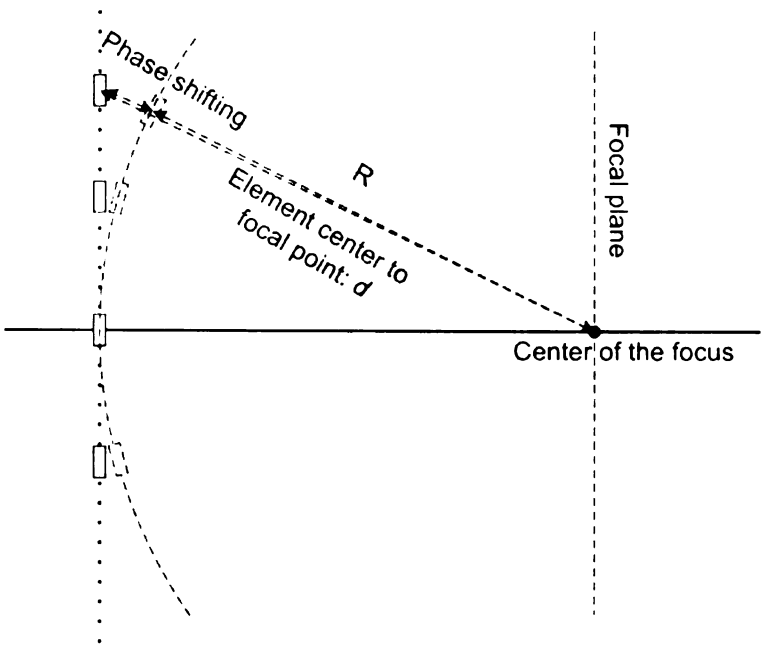

(a) focusing stratagy

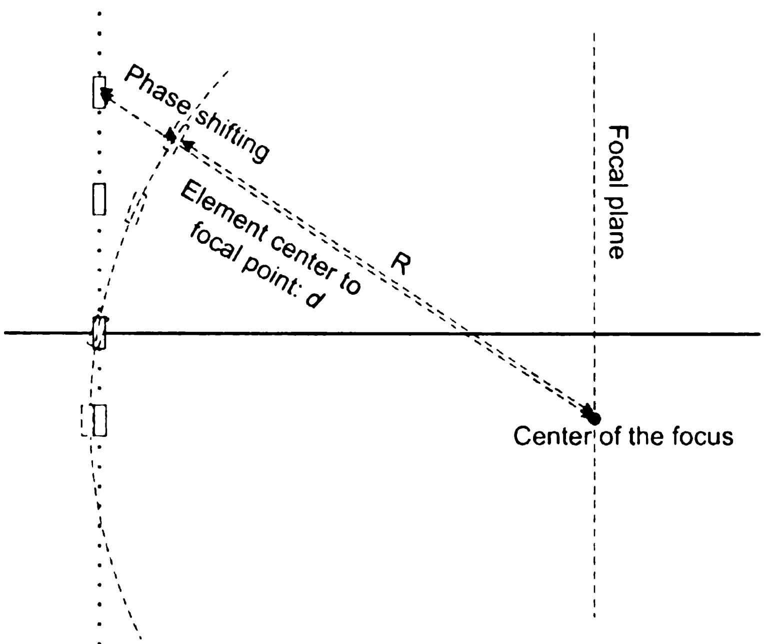

(b) Steering the focus off axis or along the axis

Figure 6.2. Focusing strategy and steering the focus

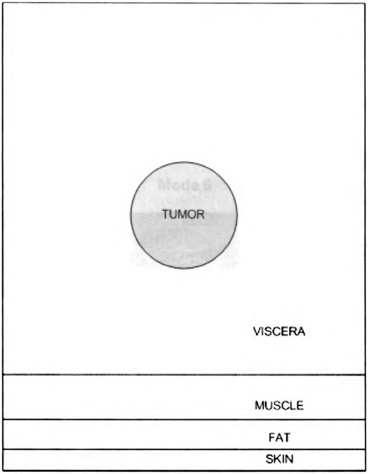

Figure 6.3. A cross section of the thermal model used for temperature calculation. The material properties is listed in Table. Table 6.1. The tumor is a sphere with 4cm diameter, 6.2 cm deep from the skin and on the z axis. The thickness of the skin layer is 0.4cm, the fat layer is 1.5cm, the muscle layer is 1.5cm and the viscera layer is 7.5cm.

	skin	fat	muscle	viscera	tumor
Blood Perfusion $W_b(kg/m^3/s)$	0	4.0	4.0	4.0	4.0
Thermal Conductivity $\kappa(W/m/°C)$	0.21	0.16	0.42	0.55	0.56

Table 6.1. Material property for human tissue and the blood specific heat is $c_b = 4000J/kg/^oC$

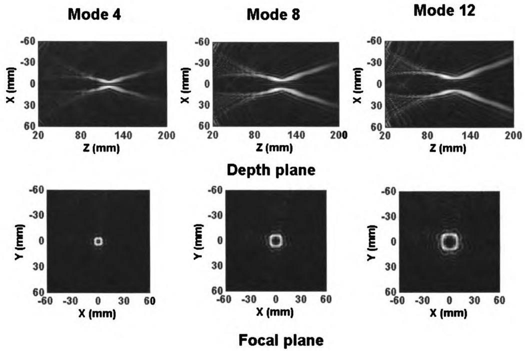

Figure 6.4. Pressure field in the focal plane and the depth plane for different modes. The focus centers of these modes are all at [0,0,12] cm (with $\alpha = 1$). Top row is the depth plane and the bottom row is the focal plane. From the left to the right, they are mode 4, mode 8 and mode 12.

6.4 Results

The driven frequency for the planar array is 1 MHz in the following analysis. The acoustic field and temperature are evaluated in 3D domain with x from -6 cm to 6 cm, y from -6 cm to 6 cm and z from 2 cm to 20 cm on the 0.075 cm interval spacing.

6.4.1 Pressure field patterns

With the same focal point location at [0,0,12] cm, the pressure field distribution on the depth plane and focal plane for different modes (M = 4, M = 8 and M = 12) are shown in Fig. Figure 6.4. Actually the $M = 0$ mode is just the single spot focus without phase modulation on the focal plane, which is not shown here. For Mode 4, 8 and 12, the pressure field distribution on the depth plane has a peak around z = 12 cm and decreases along $+z$ direction and $-z$ direction. The pressure extension along z axis for mode 8 is about 4 cm. The top view of the depth plane of these modes looks like a big 'X', but the pressure field along z axis equals zero and there is low pressure gap around z axis. From the Figure 6.4, the focus region of mode 8 is larger than that of mode 4. On the focal plane (z = 12 cm), the pressure field looks like a rectangular ring with four pressure peaks at the four corners corresponding to the four corners of the square array. The sizes of the pressure ring and the center hole (or center low pressure region) increase as the mode number increases. The size of the focal ring for mode 8 is about 3×3 cm.

With moving the focus center, the pressure field can be steered off axis and along the center axis. Off axis steering and along axis steering can be done at the same time, shown in FigFigure 6.5, by moving the focus center from [0,0,12] cm to [10,0,13.5] cm. The reference pattern without steering is shown in the left column of Fig.Figure 6.4. Adjusting the coefficient α, the focus is elongated when α is less than 1 or shrunken, when α is larger than 1, shown Fig.Figure 6.6 with mode number 8 and the focus center at [0,0,12] cm. The pressure field for mode 8 with $\alpha = 1$ is shown in the center

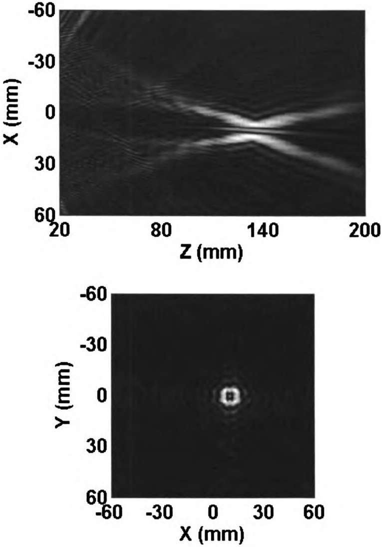

Figure 6.5. Steering the focus of mode 4 off axis and along axis, the focus center from [0, 0, 12] cm to [10, 0, 13.5] cm (with $\alpha = 1$).

column of Fig.Figure 6.4. The actual focus center moves close to the array when α is larger than 1, and moves away from the array when α is less than 1.

6.4.2 Temperature distribution

The 4 cm diameter tumor, shown in Fig.Figure 6.3, is heated with different modes: mode 4, mode 8 and mode 12. The coefficient α is set 1 for simplicity in these analysis. The focus center of mode 4 is located at [0,0,10] cm, the mode 8 center is at [0,0,10.5] cm and the focus center of the mode 16 is at [0, 0, 13] cm. In these three 3D temperature distribution, sphere mesh is the target tumor and four 2D square mesh plots are skin, fat, muscle, viscera boundary respectively. The black solid surfaces show the isothermal surface of 42^oC. The peak temperature are 44^oC in each calculation. The three dimensional field of one mode and temperature distribution in $12 \times 12 \times 18cm^3$ region are calculated within half hour (Intel P4 2.4GHz CPU and 1GB memory).

penetration

6.4.3 Frequency penetration study

For breast cancer treatment, ribs behind the breast could be over heated if ultrasound array is in front of the body and enough ultrasound energy reach the ribs. Ultrasound should offer enough heat to the deep seated tumor, but the energy on the rib surface should be lower than a threshold value. Because different frequency has different attenuation in tissue, ultrasound has different penetration depth for different ultrasound frequency. Generally low frequency ultrasound has high penetration depth, vice versa. So the ultrasound frequency should be carefully studied for breast cancer treatment with ultrasound phased array in front of the body.

With the same size array ($12cm \times 12cm$) and some focus location (110mm from the array), ultrasound at frequency range from 1MHz to 1.5MHz were used to heated the breast model, shown in Fig. Figure 6.8. In Fig. Figure 6.8, the top two mesh

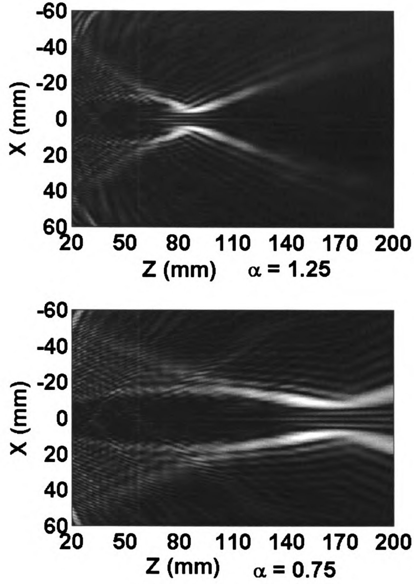

Figure 6.6. α steering for Mode 8. The plot of α = 1is shown in the center column of Fig. Figure 6.4.

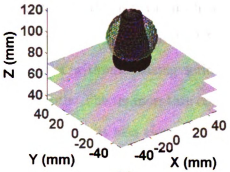

(a)

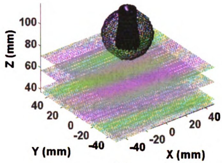

(b)

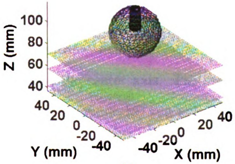

(c)

Figure 6.7. Temperature distribution for Mode 12, 8 and 4 (with $\alpha = 1$). The mesh plots are the tumor model and the black solid surfaces are the isothermal surface of 42^oC. The peak temperature are 44^oC in each calculation. a) Mode 12 with focus located at [0,0,12] cm, b) Mode 8 with focus located at [0,0,11] cm, c) Mode 4 with focus located at [0,0,10.5] cm.

contours are two ribs, the large external mesh contour is the breast, the center mesh contour is the tumor model and the solid contour are the 3D temperature iso-surface at 42^oC. From the results, the 1.0MHz ultrasound has the most penetration depth and the 42^oC contour almost reach the rib, while the 1.5MHz ultrasound can not offer a good heating inside the tumor without causing serious hot spots in health tissue because of poor penetration depth. The temperature contour of 1.1MHz result is very close to that of 1.0MHz and 1.4MHz is also close to that of 1.5MHz. Ultrasound at 1.2MHz and 1.3MHz act somewhere between what 1.1MHz and 1.5MHz do and could be the optimal frequency for breast cancer treatment.

6.5 Discussion

The two terms in Eq.7.1 with different functions work with each other very well. For mode 0, the first term of Eq.7.1 equals zero, there is no mode modulation on the focus and the size of the focus is close to one wavelength (1.5 mm for 1MHz in water). When the mode number is larger than zero, the pressure field in the depth plane has two peaks and there is a gap between two peaks, the pressure field in the focal plane is a rectangular ring with one peak at each corner, shown in Fig. Figure 6.4. Because any array element and it's center axis symmetry element have 180 degree input phase difference, the pressure fields generated by these two elements are canceled out along the center axis. The total pressure field generated by the array is zero along the center axis and very low close the center axis. The region inside of the focus with large mode number (For example: mode 12) can not be heated well, which is shown in Figs Figure 6.4 and Figure 6.7a.

Because the tumor could be off the center axis of the array, the shape of the tumor could be irregular or the The peaks of the pressure field and peaks of the temperature are not exactly in the focal plane and they are usually shifted small distance to the array, the larger mode number has the larger shift distance. In order heat the tumor at

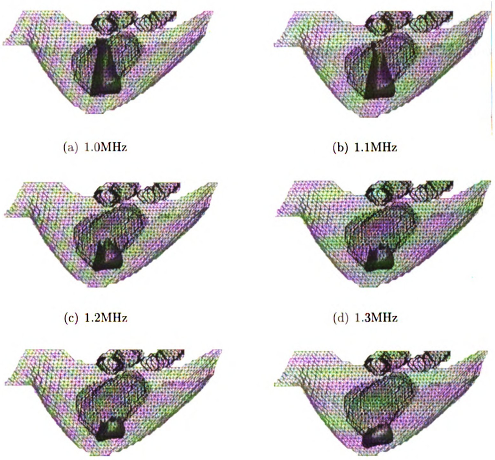

(a) 1.0MHz (b) 1.1MHz

(c) 1.2MHz (d) 1.3MHz

(e) 1.4MHz (f) 1.5MHz

Figure 6.8. The heating pattern for different frequency range from 1MHz to 1.5MHz. The array size is $12cm \times 12cm$, the gap between array and breast is 3cm and the focus is 11cm from the array. The top two mesh contours are two ribs, the large external mesh contour is the breast, the center mesh contour is the tumor model and the solid contour are the 3D temperature iso-surface at 42^oC.

the same location, different modes have different focus center, shown in Figs. Figure 6.7. From the Fig.Figure 6.5, this phase scheme can also move the focus around the target region without the shape changed. Fig.Figure 6.6 shows the phase scheme has the ability to control the focus size along the center axis. Large mode number usually has a large extension along the center axis, which will result in hot spot outside the tumor. Adjusting the α coefficient for large mode number can constrain the power deposition within the tumor region.

With the mode number increasing, the size of the focus is enlarged, shown in Figs. Figure 6.4, and the size of the over 42^oC temperature region is also increased, shown in Figs.Figure 6.7. From the temperature distribution, large number mode (Mode 12) has hollow region which is not well heated by this mode and small number mode (Mode 4) can a small solid region very well. Combing the SAR of different modes and optimizing the weight of each mode, the over 42^oC temperature region could extend the entire tumor region with 5 cm diameter without intervene heating problem.

If the ultrasound energy comes from the side of the body and the propagation path does not go through the rib region (for example the applicator in previous chapter), the rib behind the breast will not be over heated by the ultrasound. While the ribs could be over heated if ultrasound wave propagates through the rib region. The frequency should be carefully chosen so that ultrasound offers enough heat to the deep seated tumor, but the energy on the rib surface is kept at a low level. In this chapter, frequency in the range 1.0 ~ 1.5MHz were simulated for $12cm \times 12cm$ planar array by sector-vortex phase scheme with focus distance 110cm. Although the optimal frequency could be effected by the geometry shape of the array, the distance from the array to the breast, the phase scheme method and the location of the focus, frequency outside the range 1.0 ~ 1.5MHz can not give a good heating without overheating ribs and health fat tissue. The frequency range 1.2~1.3MHz is the best choice for this treatment setting in this chapter.

6.6 Conclusion

Two phase terms, phase for single spot focusing, sector-vortex phase scheme, are combined together to generate the large and size controllable focus for the 2D planar array, since the planar array is much easier to build than the concave shaped array. The large size focus is a good choice for thermal treatment of the large size tumor (diameter up to 4 or 5 cm). The focus steering property and different modes of this new phase scheme are investigated to heat the 4 cm diameter tumor which is about 6 cm underneath the skin. This phase scheme also offers a way to adjust the extension of focus along the axis direction. The ultrasound pressure fields are calculated with fast near-field method (FNM) and the temperature distribution is computed by solving a static bio-heat transfer equation. Different modes have different heating performance. Large number mode can heat large region, but the region at the center of the focus is not well heated and intervene heating problem will appear. Small number mode can heat a small region with uniform temperature distribution. Mode number from 4 to 12 and the combination of them are recommended for hyperthermia.

CHAPTER 7

HYBRID RF/US PHASED ARRAY APPLICATOR (2) FOR SMALL BREAST

7.1 Introduction

External heating devices appropriate for deep hyperthermia in the intact breast include ultrasound phased arrays[22] and radio-frequency (RF) electromagnetic phased arrays[28]. Ultrasound phased arrays are an appropriate local modality for heating small targets in the breast (up to about 2cm diameter[27]) and has the ability to steer the position of the focus in order to control the power deposition. In contrast, heat generated by RF electromagnetic devices is delivered regionally across a much larger area. RF phased arrays have been developed previously for deep hyperthermia in the pelvis [28] and in the extremities[23], respectively. The hybrid approach will exploit the regional heat generated by the RF applicator that increases the temperature of the arterial blood supply, thereby reducing the power requirements for the ultrasound component. The large heated region created by the RF phased array combined with small focal spots generated by the ultrasound phased array provides multiple opportunities for optimization of the temperature distribution produced by hybrid RF/US phased array devices.

One of the hybrid applicator design for large breast [Liyong_Hybrid_2006] base on the four antenna applicator[37] with ultrasound phased array mounted on one of the side panel. The US array is mounted on the side face of the tank to reduce the heating to the ribs caused by the reflection at the bone/tissue boundary. The US array is operated at 1MHz and is tilted to place the intended tumor target at its geometric focus. Mode scan method is used for ultrasound focusing. Temperature distributions show that that hybrid structure is capable of producing a flat with small fluctuation temperature distribution (43^oC) in the tumor region. The intervening heating in normal tissue is significantly reduced.

In this chapter, a new design of RF/US hybrid applicator is proposed for cancer treatment in small size breast. Significantly improved temperature distributions are observed in simulated hyperthermia treatments of LABC. Power distributions are simulated for a hybrid applicator consisting of an RF phased array and a planar square US phased array, and temperature responses are evaluated for hyperthermia treatments in the intact breast. In this paper, a novel RF/US hybrid device is proposed for hyperthermia treatment of LABC. This device include a four-antenna RF phased array and a 2D planar US array with 4,000 circular elements. The simulation results suggest that this hybrid device deliver more therapeutic heat into tumor than RF device and US device used along.

7.2 Applicator

7.2.1 RF phased array and applicator

The design of the RF/US hybrid applicator is based on the RF applicator in [37]. The size of the top panel is about $33.6cm \times 22.5cm$. The bottom plane is $18.8cm \times 22.5cm$. Both the top panel and the bottom panel are parallel to the xy plane and the depth of the of the is about $17.0cm$. In the two hexagonal side panels, which are both parallel to the yz plane and symmetric to the xz plane, the top edge is 33.6 cm long, the bottom edge is 18.8 cm long, higher edges are 3.3 cm, lower edges are 15.3 cm, the two lowest obtuse angles are 150^o, the two top angles are right angles, and the other two obtuse angles are 120^o. Except the top plane, other planes are covered by plastic (Lexan) with $0.5cm$ thickness. Four U-shaped antenna are mounted on four sides of the applicator shown in Fig. Figure 7.1. The arms of three antenna are parallel to the x axis. The arms of the fourth antenna on the hexagonal panel are parallel to the y axis. The planar ultrasound phased array is mounted on one

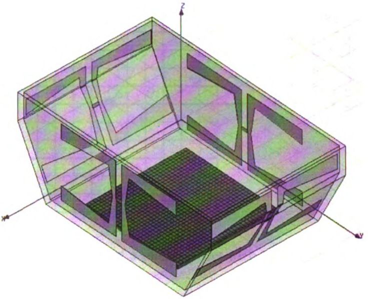

Figure 7.1. The hybrid applicator with 4 U-shaped antennas mounted on the four sides of the plastic tank, a planar ultrasound phased array mounted on a side panel.

hexagonal panel. During the treatment, the applicator is filled with deionized water with a constant temperature 39^oC. During the treatment, the patient lies down prone to the applicator and the body axis is parallel to the y axis and there is 1-2 cm air gap between the chest wall and the water surface.

7.2.2 Planar ultrasound phased array

The ultrasound phase array is square planar array with $N \times N$ square elements. The square element has an edge length a and the gap between two elements is represented by b. The elements are arranged on the grid points shown in Fig. Figure 7.2. Each element with index (i, j) is driven by a sinusoidal signal with the phase for each channel ϕ_{ij} given by

$$\phi_{ij} = M\theta_{ij} - \alpha k d^f_{ij} \tag{7.1}$$

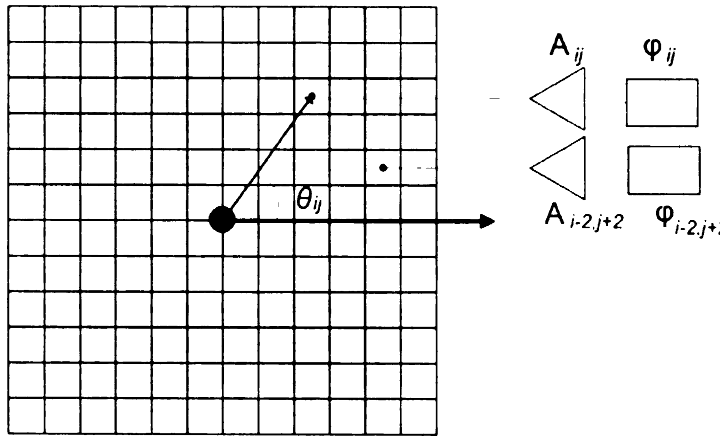

Figure 7.2. Schematic of a planar array with rectangular elements.

for $i = 1, 2, \cdots$, N and $j = 1, 2, \cdots$, N, where (i, j) is the index of the element, $\phi_{ij}$is the phase of the driven signal, θ_{ij} is the angle of the element center shown in Fig.Figure 7.2, M is the mode number, k is the wavenumber in water, α is the coefficient for focusing, d^f_{ij} is the distance from the element center to the focal point ($d^f_{ij} = \sqrt{(x_{ij} - x_f)^2 + (y_{ij} - y_f)^2 + z_f^2}$), (x_{ij}, y_{ij}) is the coordinate of the (i, j) element center, and (x_f, y_f, z_f) is the coordinate of the focal point. The first term (mode term) of Eq. 7.1 shows that the phase on each element repeats $|M|$times per rotation around the center point of the array [51, 52].

The second term in Eq. 7.1 focuses the acoustic energy as shown in Fig. Figure 6.2. By performing these phase adjustments across the aperture, the wave front emitted by the array converges to the focus specified by (x_i, y_i, z_i) shown in Fig. Figure 6.2a. The ultrasound focus can also be steered off the center axis or steered along the axis as shown in Fig. Figure 6.2a, where the coefficient of the focusing term controls the extent of the focus along the center axis. Thus, adjusting the α coefficients changes the shape of the shifted wave front. When α equals one, the initial shifted wave front is spherical. The combination of the first and second terms in Eq. 7.1 therefore focuses and modulates the pressure field distribution radiated by the phased array.

7.3 Methodology

7.3.1 Pressure field calculation

Using a linear model, the total acoustic pressure field is the superposition of the pressure field of each element. Since the size and shape of the elements in the phased array are the same, the pressure field generated by elements are identical to each other. The pressure field generated by a single element source is calculated by combining the fast near-field method (FNM) [39] and the angular spectrum approach(ASA)[40, 16, 41]. Because of the equivalent sizes of the sampling grids and the array elements, the total field can be calculated by shifting and adding the field generated by the center element in a broader dimension. Due to the large number of elements and grid points, ASA is incorporated to accelerate the pressure field computation, since ASA utilizes FFT's to propagate acoustic fields. The pressure field at the first transverse plane is calculated by FNM and linearly propagated. Computational planes with a uniform size are slightly larger than the aperture (Zero padding eliminates circular convolution artifacts for short propagation distances, then the same effect is achieved by angular restriction for longer propagation distances). Both the array and the planes are normal to and centered at the z axis. The three dimensional field are calculated within an hour (Intel P4 2.4GHz CPU and 1GB memory) by using the combined simulation approach.

In order to reduce the intervening tissue heating, the mode scanning technique [42] cancels the fields in symmetric planes to reduce unwanted heat accumulated between the array and the tumor region. In the mode scanning technique, the US array is subdivided into the 4 regions shown in Fig. Figure 7.3a. Region I synthesizes a single focus at point (x,y,z). The driven phase distribution for the region II is symmetric to region I about y axis with 180^o phase difference and focus at (-x,y,z), region VI is symmetric to region I about x axis with 180^o phase difference and focus at (x,-y,z), and region III is symmetric to region I about center point and focus at (-x,-y,z). The array with four regions generates 4 focal spots and cancels the pressure field in the xz plane and the yz plane. Multi focus groups, shown in Fig. Figure 7.3b, can afford better heating pattern than single focus group. Three groups (with 12 focal points) are used in the present simulation.

After the 3D pressure field is computed, the steady state temperature field is simulated by solving BHTE equation using the SAR pressure as an input. The SAR generate by the pressure field is calculated by $SAR_P = \frac{\alpha}{\rho c} |P|^2$, where c is the velocity of the acoustic wave, ρ is the density and α is the acoustic attenuation coefficient.

7.3.2 Temperature Optimization

In this hybrid approach, the SAR generated by electric field and the temperature distribution produced by the total SAR (the sum of the SAR of E field and the SAR of pressure field) need to be optimized. There are several optimization methods[43, 44, 45, 18] to optimize the temperature distribution. There is no existing solution to optimize the SAR or temperature for RF/US hybrid source simultaneously. In this simulation, the weight of the total RF energy and the total US energy is optimized to minimized the temperature objective function. The temperature optimization function used here is in the same vein as those proposed in literature[46, 47, 48, 49, 50]. The objective is to achieve a specified tumor and normal tissue distribution: all points in tumor tissue at 43^oC, and all points in normal tissue at or below 42^oC.

7.4 Results

In the FE simulation, the E field is calculated in the whole 3D region inside the ABC boundary. The SAR and temperature are evaluated in a rectangular region with x from -8.0 cm to 9.0 cm, y from -6.0 cm to 6.0 cm and z from -6.0 cm to 4 cm on the 0.1 cm interval spacing. This region (16.0 cm$\times$16.0 cm$\times$10.0 cm) contains the

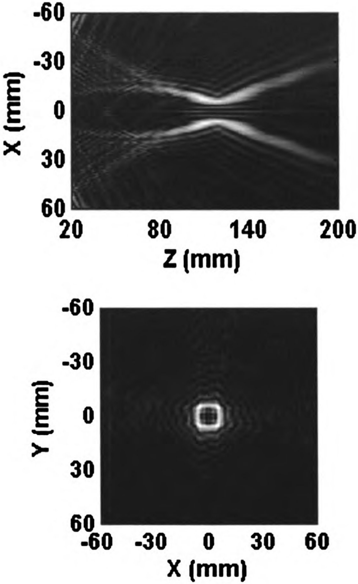

Figure 7.3. Phase a scheme for four focus mode scan and focusing strategy for planar ultrasound phased array

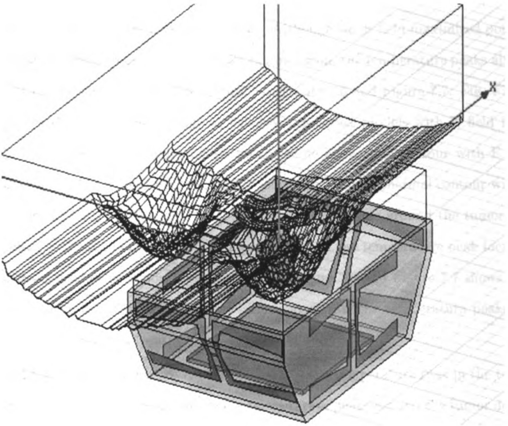

Figure 7.4. hybrid applicator including 4 RF antenna and US phased array

breast, the tumor, a portion of skin and deionized water. The pressure field is only computed in this region specified above. Five faces of the rectangular region are in the water boundary and the top face of this region is located inside the body. During calculating the temperature, the five water boundaries are set at a fixed temperature (39^oC) and the sixth boundary is set as the body temperature (37^oC).

After the E field is calculated for each antenna, the total E field is maximized at the selected point. Because the four antennas are all in one plane (parallel to xy plane), the RF array lacks the steering ability along z axis and the E field focus can only be steered in xy plane. The total E field outside the tumor region (in normal health tissue) is much stronger than that in the tumor because of the impedance mismatch between tumor and fat materials. Although the E field maximized point is picked in the tumor region or outside the tumor region, the temperature peaks always outside the tumor shown in Figs. Figure 7.5, Figure 7.6 and Figure 7.7. Fig. Figure 7.5 shows the isothermal contour at 42^oC in the breast models with E field focus at [5, 15, 0] mm. Fig. Figure 7.6 shows the same isothermal contour with E field focus at [-5, 0, 0] mm and Fig. Figure 7.7 shows the same isothermal contour with E field focus at [-20, 20, 0] mm. The E field maximized points around the tumor/ fat boundary and outside the tumor give more control on the temperature peak location than those inside the tumor. Figs. Figure 7.5, Figure 7.6 and Figure 7.7 shows that different focus locations give different heating patterns, the temperature peaks are distributed at different locations and outside the tumor.

In Figs. Figure 7.5, Figure 7.6 and Figure 7.7, the temperature rises in the tumor region are about 3~4.5 degree. Since the temperature peaks around the tumor do not overlap with each other, the superposing of the three RF SAR with different weights ([0.5, 0.3, 0.5]) can give higher temperature rise in tumor and the smaller hot spots outside the tumor shown in Fig Figure 7.8. In Fig Figure 7.8, a large portion of tumor is heated over 42^oC and the isothermal contour looks like a ring around the tumor in xy plane (the plane contains the feed points of the four antenna). Some portion of the tumor such as the center tumor region and deep region of tumor are not well penetrated by EM.

With the sector-vortex phasing scheme, ultrasound generated by a large 2D planar array can heat a relatively large region. Mode number 8 is chosen for this simulation and the temperature distribution heated by mode 8 is shown in Fig. Figure 7.9. The 42^oC region has a 5 cm extension along the z axis and average 2 cm diameter. The tumor region, which is not well penetrated by RF in Fig. Figure 7.8, is well covered by US heating.

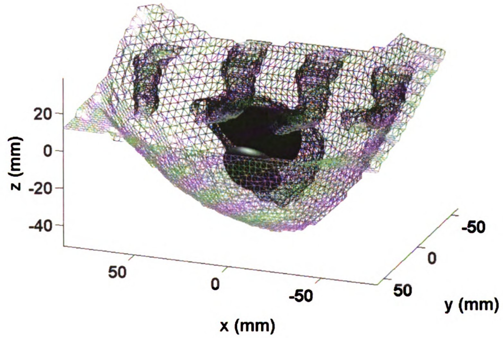

Figure 7.5. Temperature results with RF focus at location 1 (0,10,0)

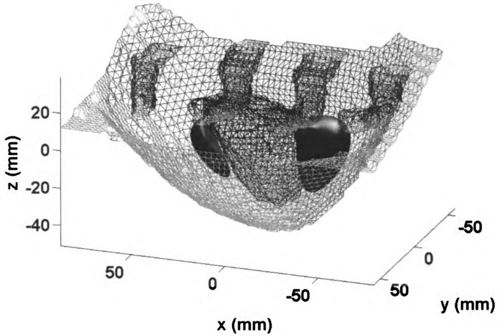

Figure 7.6. Temperature results with with RF focus at location 2: (5,0,0)

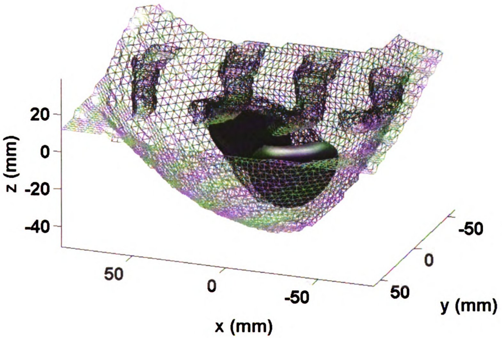

Figure 7.7. Temperature results with with RF focus at location 2: (5,0,0)

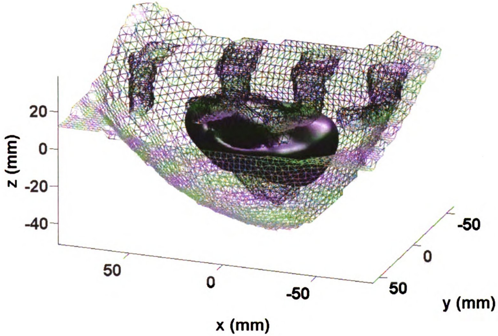

Figure 7.8. Temperature results with the combination of above 3 RF heating with **weight** [0.5, 0.3, 0.5]

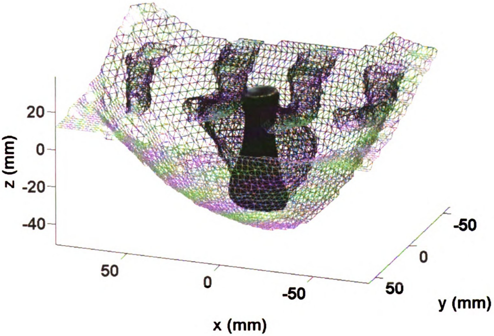

Figure 7.9. Temperature results with US mode 8

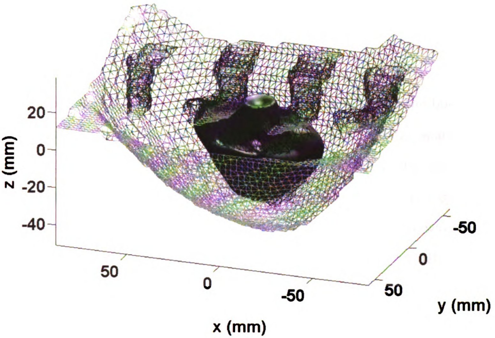

Figure 7.10. Temperature results with hybrid RF/US

When the RF and ultrasound are combined together, the temperature optimization method is applied to adjust the weights of RF SAR and US SAR to minimize the temperature objective function. The hybrid SAR, which combine the total RF SAR and ultrasound SAR with mode 8, gives very good heating pattern in tumor shown in Fig. Figure 7.10. Almost 90% of the tumor region is heated over 42^oC and the hot spots in the health tissue are dramatically reduced.

Fig Figure 7.11 gives a more detail and insight view of the temperature distribution in the breast model. From these three figure, there is a large region with temperature over 43^oC at the center of tumor. In Fig. Figure 7.11b and c, the contour of over 42^oC follows the tumor boundary and ultrasound has majority contribution to the temperature rise at the center region of tumor (also the center of the ultrasound focus with mode 8).

7.5 Discussion

This hybrid applicator with ultrasound phased array mounted at the bottom is designed for small breasts. Because small breasts do not have enough space for ultrasound wave converging in breast from the side position. So the most possible position for US phased array is mounted at the bottom of the applicator in Fig. Figure 7.1 and facing the breast. In order to reduce the pain caused by the pressure wave reflection on the ribs, the operating frequency is increased from 1MHz to 1.1MHz to increase the attenuation on the pressure wave and the pressure on the rib bone surface is reduced.

The intact small breast is placed at the geometric center of the phased array and the antennas are close and face toward the breast. If the amplitude of power input of each antenna is set to unity and the phase is set to zero, there is an E field focus on the central axis of the water tank about 3 cm below the water surface where the patient breast is placed. The four antennas are placed around the breast like a cage and two of them are tilted to move the E field focus along $z\prime$ direction. If there is no tilt and antenna are all vertical to xy plane, the E field focus will be in the plane containing all four feeding point of the array and this focus position is too low to heat tumor in small breast.

The array in the applicator design[37] is lined up and the antenna arms are parallel to each other. So the E field in the breast region is always linearly polarized in one direction which causes the hot spots aligned in the same direction. In current arrangement of antenna, the E field in the breast region is still linearly polarized, but

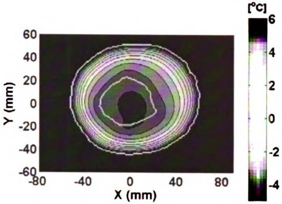

(a) XY view at z = - 20 mm

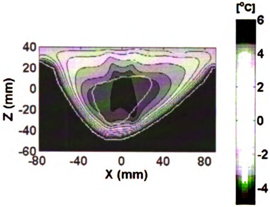

(b) XZ view with y = 0 mm

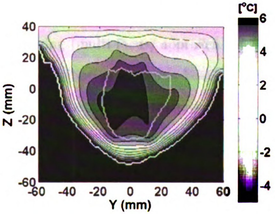

(c) YZ view with x = 0 mm

Figure 7.11. 3 cut view of the temperature distribution with RF/US hybrid source.

the polarization direction is not fixed and can be control by changing the antenna input. The total polarized E field can be any direction in the xy plane. Figs. Figure 7.5, Figure 7.6 and Figure 7.7 show three polarization directions from one hot spot pointing to another one.

The parameters of the US phased array, such as element size, gap size and array size, are carefully chosen. Small array sizes have small window to deliver ultrasound power and the power density on the path to the target region will be high, which can cause intervening heating. Large element center to center spacing could cause severe grating lobes and the element size has stronger effect than the gap size. Small element center to center spacing has better performance, but it gives a large number of the element in the ultrasound phased array. *(Explain why picking these array parameters)*

The E field and SAR inside breast and tumor, which are not shown here, change gradually and decay in the direction to the chest. These temperature in Figs. Figure 7.5, Figure 7.8 and Figure 7.11 indicate that E field by RF antenna array can heat the the proximal region of the tumor very well, the temperature peak is located inside of the tumor and close to the tumor/fat boundary. Most of the over 42^o region is inside the tumor, but the deep region (close to the chest wall) of tumor is not accessible by RF power. *(Talk about the heating performance by RF)*

Single-spot-focus scanning (multi-focus) approach can produce an optimal time-averaged absorbed power distribution for tumor heating. But the average intervening heating is also increased as the focus moves around and the power deposition at the focal points are still high which cause sharp temperature peaks there. Mode scanning cancels the pressure field in the phase symmetric planes, thus reducing the intervening heating and achieving low power deposition on the focal points (~1/4 of single spot focus power). Mode scanning techniques with 12 foci in this simulation are employed to heat tumors whose dimension are much larger than one single focus. In the temperature distribution in the Fig. Figure 7.6, the power deposition right on those foci are actually lower than the peak power deposition region which is located about 2 cm behind the foci ring (close to the US array) and is also clearly indicated in Fig. Figure 7.7. That is the reason that the foci are placed beyond the tumor region and inside normal tissue. In Fig. Figure 5.12, the shape of the over 42^oC regions heated by US power are not symmetric: the part in the tumor shrinks more than those outside the tumor, because of different blood perfusion. Although those foci outside of the tumor do not heat the tumor directly, they can elevate the temperature in the deep region of tumor. In this simulation, the upper limit of the temperature is set as 44^oC, which will alleviate the pain caused by thermal treatment. *(Talk about the heating performance by US)*

7.6 Conclusions

A new RF/US hybrid applicator geometry is evaluated for hyperthermia treatments of locally advanced breast cancer. By scanning the E field focus and adding the ultrasound broad focus phasing scheme, the EM and US field together achieve a temperature distribution that covers the majority of the 3D tumor volume. The 3D temperature distribution is calculated in the thermal model based on BHTE. This combination heats a breast tumor surrounded by fat better than either modality alone. Comparisons between RF/US hybrid method and RF-only or US-only show that the hybrid heating strategy can heat the whole region of the LABC tumor better that US or RF alone.

CHAPTER 8

E FIELD POLARIZATION AND CROSS ANTENNA

In most RF thermal therapy system[?, 45, 28, 2, 37], dipole antenna or dual dipole antenna are used as the element of the phased array. In the most target heating region, the E field radiated by the dipole antenna or dual dipole antenna is linear polarized on the plane which is vertical to the antenna. The direction of E field polarization is parallel to the antenna arms. In the hyperthermia treatment of breast cancer, this kind of E field polarization can cause the hot spots outside of the tumor[37] because of different reflection coefficient along the tumor/normal tissue boundary. The hot spots are located along the polarization direction and around to the tumor. One way to eliminate the linear polarization effect is to replace the dipole antenna with the antenna which can radiate the circular polarized EM wave.

The polarization of an electromagnetic wave is defined as the orientation of the electric field vector. Recall that the electric field vector is perpendicular to both the direction of travel and the magnetic field vector. The polarization is described by the geometric figure traced by the electric field vector upon a stationary plane perpendicular to the direction of propagation, as the wave travels through that plane. There are several types of antennas which can radiate circular polarization, such as helical antenna, spiral antenna, two orthogonal conductors, etc. The helical antenna is not compact enough to build an applicator for breast cancer treatment. The spiral antenna is complicated to build and to compose an array for breast cancer treatment. In order to make the applicator compact and This cross antenna is composed of two dipole antennas perpendicular to each other and excited with 90 degree phase difference. A $\lambda/4$ phase delay line is designed for this cross antenna to decrease the number the feed port from two to one.

In this paper, a new antenna, cross antenna with delay line, is designed for regional hyperthermia. This cross antenna composed of two dipole antenna and two delay lines can radiate circular polarized electromagnetic wave with just one input. The electromagnetic (EM) wave propagation along the cross antenna and the electric field distribution in time domain is inspected with the Finite Difference in Time Domain (FDTD) simulation. The 90 degree phase shift between two branches and the circular polarization of E field in the target region are verified. Two heating spots are observed close to the tumor/normal tissue boundary and they rotate around the tumor. The average SAR around and inside the tumor is more homogeneous than that by dipoles. An applicator with four cross antenna is proposed to treat the breast tumor.

8.1 Boundary condition

Electromagnetic boundary conditions for two different material boundary are shown in Eq. 8.1.

$$\begin{aligned} E_{1t} &= E_{2t} \\ \epsilon_1 E_{1n} &= \epsilon_2 E_{2n} \end{aligned} \tag{8.1}$$

In these two equation, E means electric field and ϵ is the material permittivity. t is the transverse direction and n is the normal direction.

A simple drawing in Fig. Figure 8.1 will show how E field polarization effects the E field distribution around the tumor fat boundary. In this figure, tumor is a circle surrounded by fat tissue and E field direction points to the top of the figure indicated by black arrows. E field directions are vertical to the tumor/fat boundary at location 1 and 2 , while they are parallel to the tumor/fat boundary at location 3 and 4. According to Eq. 8.1, E field in tumor and E field in fat are equal at location

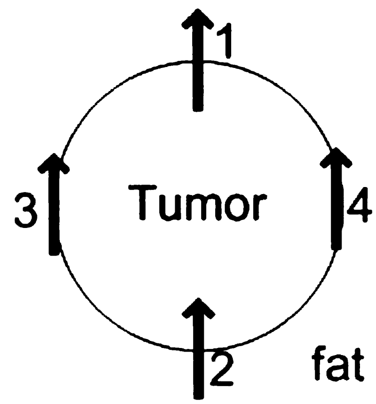

Figure 8.1. E field polarization and boundary condition

3 and 4. However E field in fat is much stronger ($\epsilon_{tumor}/\epsilon_{fat} \approx 8$ times at 140MHz) than that in tumor in location, which will cause hot spot in location 1 and 2 in fat. The simulation results in Chapter. 3 shows there are two hot spots along the E field direction and proves this theory.

8.2 Cross antenna and applicator

Two dipole antennas are placed perpendicular to each other with the superposing the center of these two antennas, shown in Fig.Figure 8.2a. The antenna plane is defined the plane containing the two dipole antennas. The central axis passes through the common center of the two dipole and is perpendicular to the antenna plane. When the feeding of two dipole antennas has 90 degree (or -90 degree) phase difference, the E-field radiated by the structure is circular polarized along the central axis.

But this two dipole structure needs two signal inputs, which have 90 degree delay, and matching circuits. To simplify the input, a phase delay line is added between two dipole. One dipole antenna is connected to the other dipole with the delay line.The total length of the phase delay line is $\lambda/4$ (56.5 mm @ 140MHz in water). In order to make the antenna compact, the length of each arm of the cross antenna is $\lambda/4$. The design of the cross antenna is shown in Fig.Figure 8.2b.

A breast model is designed here to compare the heating performance between the cross antenna and the common dipole antenna. The cross view of the one-antenna applicator is shown in Fig.Figure 8.3. The antenna is mounted on the large size plastic layer (Lexan). It is air below the plastic layer and water over this layer. A breast model is placed at the target heating region, which is along the antenna central axis and about 15 cm far away from the antenna. The tumor is a sphere with 5 cm diameter, the breast is a half sphere with 7.5 cm radius and the fat layer behind the breast is about 3 cm thick.

One-antenna applicator can not reach the desired heating performance for deep seated breast tumor duo to the decay and reflection of E field. Phased array of cross antenna with dedicated enclosure is a better choice. The four cross antenna applicator is shown in Fig.Figure 8.4, which has the same enclosure size as the four antenna applicator in[37]. The tank enclosure consists of 6 solid Lexan (GE Polymerland, North America: www.gepolymerland.com) side panels and a Lexan top piece with a large opening. RF antennas are mounted on four of the rectangular side panels, and the two remaining side panels are irregular pentagons with one axis of symmetry. The four rectangular side panels are 12.8cm by 21.5cm, and the pentagonal side panels are 12.8cm by 12.8cm by 12.8cm by 12.8cm by 33.2cm. In each pentagonal side panel, the obtuse angle measured at the lowest point on the tank is 112°, the two obtuse angles measured at adjacent vertices are 153°, and the two remaining acute angles are 61°. Each Lexan panel is approximately 5mm thick.

Four cross antennas are mounted the inner side of the lexan tank, Each antenna is rotated 45 degree relate to the edges of each panel and the arms of the cross antenna has a 45 degree with x axis. In order to decrease the cross talk among the four antenna, those four antenna are exact the same (RHCP or LHCP) and face to the applicator center.

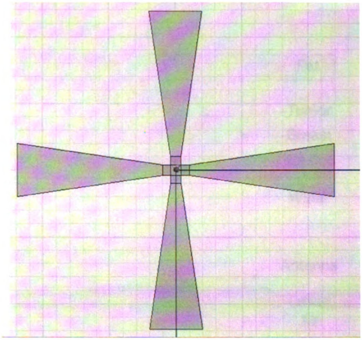

(a)

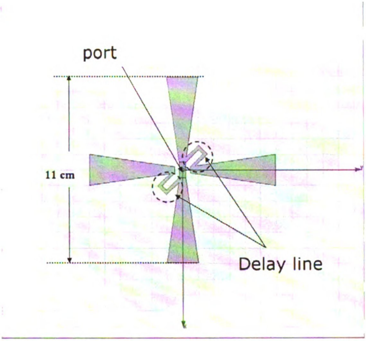

(b)

Figure 8.2. a) Original two dipole antenna which are perpendicular to each other, b) Cross antenna with $\lambda/4$ phase delay line

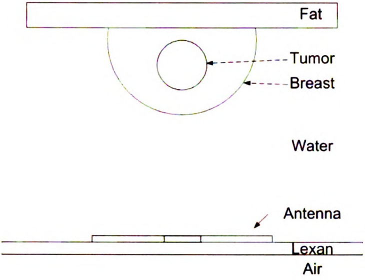

Figure 8.3. A cross section of one antenna applicator with breast model

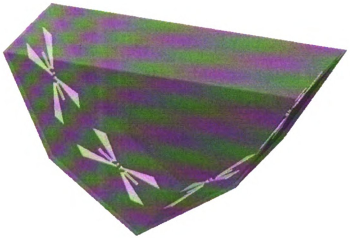

Figure 8.4. 3D view of the four cross antenna applicator. Each antenna is rotated 45 degree relate to the edges of each panel and mounted on the inner side of the panels.

8.3 Results

The polarization of the electromagnetic field radiated by the cross antenna needs to be investigated. The E field distributions varying with time, important to understand this characteristic, are simulated with the finite difference in time domain (FDTD) method. The FDTD method is a numerical solution for Maxwell's curl equations, which are based upon volumetric sampling of the unknown electric field and magnetic field within and surrounding the structure of interest over a period of time.

The time domain E field is generated by the commercial software XFDTD (Remcom, Inc. State College, PA). XFDTD can handle 3D model of antenna and applicator and subdivide them into equal-space meshes with 1 mm grid size (about 0.005λ @ 140MHz in water). The whole 3D computational domain for the four antenna applicator is about $380mm \times 470mm \times 225mm$. In these simulations, two source type are Gaussian and sinusoid waveform used for different cases. Gaussian waveform is used for viewing the electromagnetic wave propagation in the cross antenna and sinusoid waveform is used for other cases, such us calculating the E field in the target heating region. Six side boundaries are assigned with the eight-layer PML boundary to absorb the outgoing wave.

For the four antenna applicator, the E-field distribution is computed for each antenna separately, loaded into Matlab *(Mathworks Co, Natick, MA), and then the results are superposed. The magnitude of the total E-field is computed according to

$$|\mathbf{E}(x,y,z)| = \left|\sum_{n=1}^{N} \mathbf{U}_n(x,y,z) I_n\right|, \tag{8.2}$$

where I_n is a complex number representing the amplitude and the phase of the n-th antenna input, and the vector $\mathbf{I}$ steers and focuses the E-field. In Eq. 8.2, $\mathbf{U}_n$

Readers can contact with the author for the script used to read the output of XFDTD into Matlab.

represents the electric field contribution produced by the n-th antenna for a unit input excitation (i.e., $I_n = 1\angle 0°$), $N = 4$ is the number of the antennas in the phased array applicator, $\mathbf{E}$ represents the total electric field, and (x, y, z) represents the Cartesian coordinates of the simulated E-field.

Electromagnetic wave propagation in the cross antenna, E field polarization in breast model and E field distribution in the four antenna applicator are investigated by simulations.

8.3.1 Electromagnetic wave propagation in antenna

In order to examine the electromagnetic wave propagation along the cross antenna, the antenna is mounted in air/plastic/ water three layer model, the antenna is on the plastic surface in the water side and the thickness of the plastic layer is 5 mm. The dimension of the model is about $16cm \times 16cm \times 10cm$ and the outer boundaries are set PML with 8 layers. The mesh size is 1 mm in the direction parallel to the antenna plane and 0.5 cm in the direction vertical to the antenna plane. A Gaussian pulse input with 32 ps pulse width and total 1000 time steps is used as the signal input and the time step is about 1.926 ps.

E field distribution in the antenna plane is recorded in time sequence with 10 steps increase. From the recorded results, a pulse wave front is propagating in the antenna arms and delay lines. Fig. Figure 8.5 shows 4 typical time steps. In Fig.Figure 8.5, a) shows the EM wave just arrives the port of the antenna. b) shows EM wave is propagating at the half way of the vertical branch and the half way in the delay line. c) shows EM wave arrives the end of the vertical branch and reaches the horizontal branch, d) shows the EM wave reaches the end of the horizontal branch.

8.3.2 E field distribution for one antenna

The heating performance in the one antenna applicator with the breast model shown in Fig. Figure 8.3 is compared between the cross antenna and the dual dipole antenna.

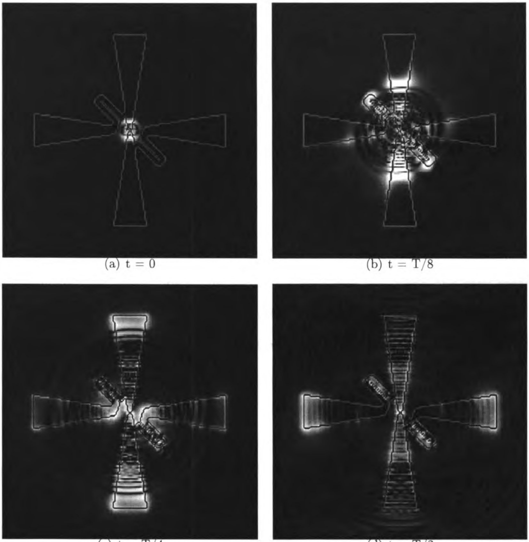

(a) t = 0 (b) t = T/8

(c) t = T/4 (d) t = T/2

Figure 8.5. A short Gaussian pulse is an input and the E field distribution on the antenna plane are recorded in different time steps. a) t = 0, b) t = T/8, c) t = T/4, d) t = T/2 (1/T = 140 MHz).

The size of the applicator, the distance from antenna to the breast model, the material properties and the distance from applicator to the radiation boundary are keep the same. The E-field distributions in the center plane (parallel to the antenna plane, through the center of the tumor) are show in Fig.Figure 8.6. Fig.Figure 8.6a shows the E field distribution by the dual dipole antenna and Fig.Figure 8.6b shows that by the cross antenna. In Fig. Figure 8.6a, there are two E field peak region around the tumor along the x direction and also two E field valley region along the y direction. These two E field peak regions can cause two hot spots outside the tumor. While the E field distribution is uniform around the tumor for the cross antenna shown in Fig. Figure 8.6b. Fig. Figure 8.6c shows the magnitude of E field along the tumor boundary in the center cut plane.

8.3.3 Single cross antenna applicator at 915MHz with oil bolus

The basic thought about this single applicator is to design a cheap and easy control hyperthermia applicator for breast cancer treatment, which also need not expensive accessories such as shielding room. The frequency 915MHz is approved by FDA for medicine in USA and many other countries and the shield room is unnecessary for the applicator working at this frequency. But the 915MHz wavelength is too small in water, which will cause unwanted standing wave and resonance in the applicator. The mineral oil is chosen here as the media for EM wave propagation and body surface cooling. The relative permittivity of the mineral oil is about 3 and the wavelength in oil is 18.9 cm. The applicator and the breast model is shown in Fig Figure 8.7. The enclosure of the applicator is same at that of the five antenna applicator because the size and shape of this applicator works very well both in simulation and treatment and prevents the unwanted resonance. The cross antenna is mounted at the center of the bottom panel because the breast is symmetric when looking from the bottom. The breast model is similar to the simple breast model which is similar to that in Chapter 3 and the four cylinders behind the breast are the four ribs.

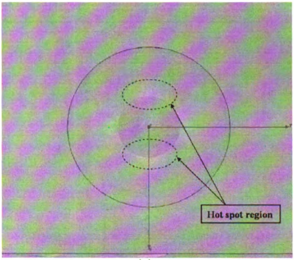

(a)

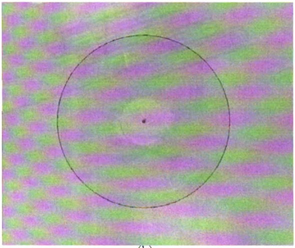

(b)

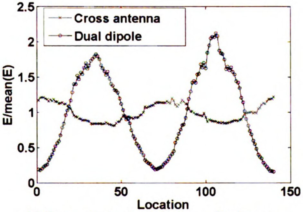

(c) E magnitude along the tumor/fat boundary

Figure 8.6. Cross antenna model and E field distribution in the breast model

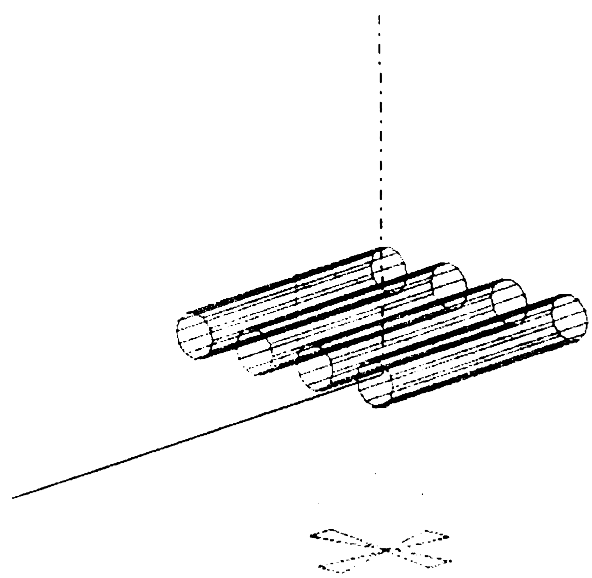

Figure 8.7. Single cross antenna applicator driven at 915MHz, the applicator is filled with mineral oil, whose relative permittivity is about 3. The enclosure of the applicator is same at that of the five antenna applicator and the cross antenna is mounted at the center of the bottom panel. The breast model is the simple breast model which is similar to that in Chapter 3 and the four cylinders behind the breast are the four ribs.

The delay line of the cross antenna should be redesigned for 915MHz, since the wavelength is different with 140MHz at water. Here for simulation convenience, two dipole antenna with two power input are used at the circular polarization source. E field on xz plane and yz plane are shown in Fig. Figure 8.8. The E field distribution around the tumor region in xz plane are similar to the distribution in yz plane, because the E field in tumor region are circular polarized and the breast model are axial symmetric.

Fig. Figure 8.9 shows the SAR distribution in yz and xz plane. The SAR peak is located at the bottom of the tumor which is close to the antenna. In the breast fat tissue, the SAR peak has a gradient along z axis and the peak is close to the breast skin which can be cooled down by oil circulator. The SAR is very low in other part of the body. The temperature distribution is shown in Fig. Figure 8.10. It shows the temperature peak region is inside the tumor.

The model with tumor off center axis is also simulated. The tumor is moved -10mm along x axis and the other part of the patient model and the applicator are kept the same as that in the previous simulation. The antenna are still operated at 915MHz with the oil bolus. The temperature results are shown in Fig.Figure 8.11 and the temperature peak region is still located inside the tumor. From the temperature distribution in xz plane, the location of the temperature peak is also move with the tumor along x axis about -8 mm.

8.3.4 E field distribution in four antenna applicator

The target heating region in the four antenna applicator in Fig.Figure 8.4 is at the center of and underneath the top water surface, where the patient breast should be located. If the amplitude of power input of each antenna is set to unity and the starting phase is set to zero, there is an E field focus at the target heating region.

The four antenna applicator model is placed at the center of the $60cm \times 60cm \times 70cm$ air region with 8 layer PML. The input to four antenna is sinusoidal wave at

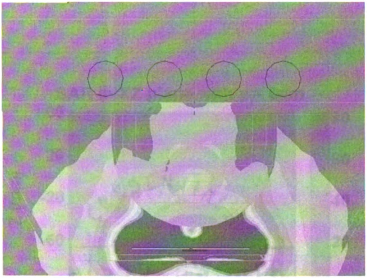

(a)

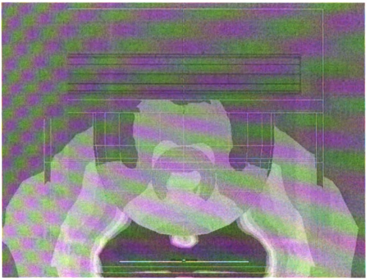

(b)

Figure 8.8. E field distribution in the breast model and water tank. a) shows the E field on the xz plane with y = 0, b) shows the E field on the yz plane with x = 0; There are strong E field close the antenna region. They also show E field decays with increasing the penetration depth.

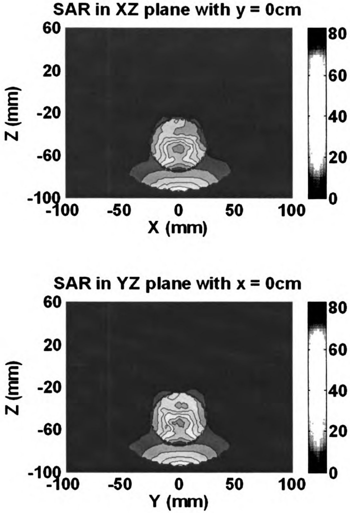

Figure 8.9. SAR distribution in xz and yz plane

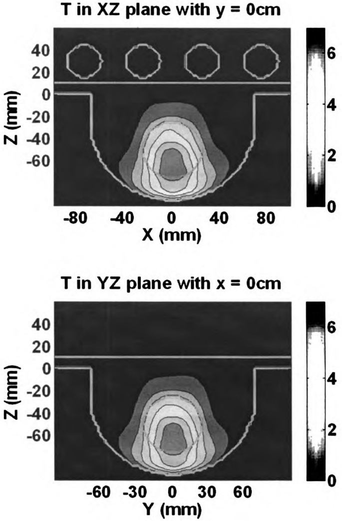

Figure 8.10. Temperature increase distribution in xz and yz plane. The peak temperature is 44^oC inside the tumor and the oil bolus temperature is body temperature 37^oC.

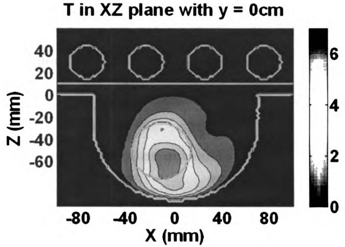

(a)

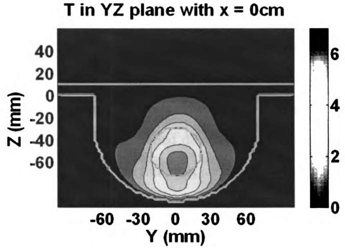

(b)

Figure 8.11. Temperature increase distribution for the breast model with tumor off axis shifting -1 cm along x axis.

140 MHz and the total length of the input 10 periods. The magnitude of the input in four channel are the same and there are no phase delay among the four input. The time average E field distribution in three cut planes are shown in Fig. Figure 8.12. All three views show there is a E field focus at the center of the applicator and the focus is about 3 cm below the water surface. In time domain, E field focus runs around the focus region.

8.4 Discussion

8.4.1 The delay line of the cross antenna

The two delay lines are the key components in the cross antenna. The original design of the cross antenna are just two dipole antennas cross to each other. The excitations of these two dipole are separate with 90 degree phase shift. In order to simplify the excitation, these two dipoles can be combined together with the delay line component. The length of one delay line is equal to $\lambda/4$(140 MHz). The geometric shape of the delay line is U shape, which is mainly determined by the shape of the two cross dipoles, shown in Fig. Figure 8.2. Another advantage of the shape of the delay line is that the electric current in the two arms of the U shaped delay line are opposite and the E field radiated by the U shaped delay line is canceled.

To verify the design of the delay line, it is necessary to investigate the detail of the electromagnetic (EM) wave propagation in the cross antenna. A short Gaussian pulse is an input and the E field distribution on the antenna plane is recorded in different time steps. Fig. Figure 8.5 shows four time steps of the EM wave propagating along the surface of the cross antenna. In Fig. Figure 8.5a, the electromagnetic starts propagating in the vertical dipole. In Fig. Figure 8.5b, the wave front reaches the half way of the vertical dipole and half way of the delay line. In Fig. Figure 8.5c, the wave front reaches the end of the vertical dipole and starts propagating in the horizontal dipole. Fig. Figure 8.5d shows the wave front reaches the end of the

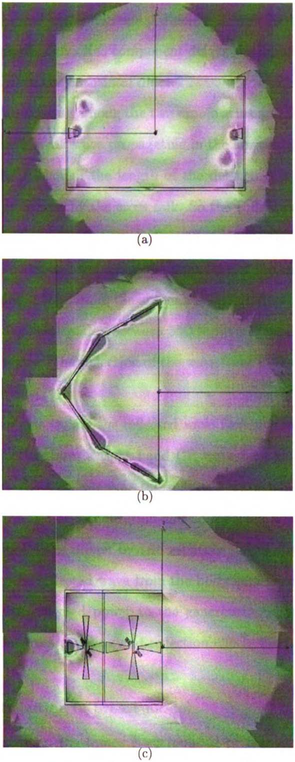

Figure 8.12. E field distribution in the four cross antenna applicator

horizontal dipole. The time gap between the wave front reaching the end of the vertical dipole and the end of the horizontal dipole is T/4 or 90 degree (at 140 MHz). This simulation shows the delay line component delays the input sinusoidal signal 90 degree (at 140 MHz) into the horizontal dipole.

There is cross talks existing among the two dipole arms and the arms of the delay line, for example there is weak wave propagating in the horizontal dipole at time T/8 in Fig. Figure 8.5 b. Although the length of the delay line is $\lambda/4$(140 MHz), the delay is not exact T/4 caused by the cross talk. So the E field radiated by this cross antenna is not purely circular polarized. In Fig. Figure 8.6b, the heating by the cross antenna is still not perfect uniform along the boundary of the tumor.

In the Gaussian pulse simulation, the antenna is mounted at the air/water boundary. There is a impedance mismatch between 50Ω input impedance and the radiation impedance of the antenna. The reflection of the wave front is observed in the vertical dipole in Fig. Figure 8.5d.

The delay line can also isolate the reflected wave from coming into the amplified system. Since a reflection from a right hand CP wave returns as a left hand wave and is reflected back the CP antenna, the reflected wave will generated opposite direction current at the two arm connection and no reflected power flows back to the generator. If two dipoles are driven by two separate power channels which have a 90^o phase shift, then the reflected wave from the body surface would directly return through each dipole as reflected power to the generator. So when deciding about applicator choices, the cross coupling and reflection effects need to be considered for the driving system.

8.4.2 E field distribution in breast model

In breast cancer treatment, the tumor is surrounded by fat tissue and the breast is immersed in the deionized water. The permittivity of fat material is much less that of tumor and water and the conductivity of the fat is also much less that of tumor. This three layers structure with impedance mismatch causes difficulty to the applicator with dipole type antenna aligned in the same direction to heat the large size tumor. This type applicator has different E field penetrations in different directions, because the E field radiated by dipole antenna is linear polarized in the tumor region. The inhomogeneous penetration of E field by dipole type antenna in the breast model in Fig. Figure 8.3 are shown in Fig. Figure 8.6a. The dipole antenna is along the x axis, the E field on this cut plane is linear polarized along x axis. Around the tumor, the E field at the region close to x axis is much stronger than that close to y axis and will cause two hot spots at the tumor/fat boundary. When the dipole antenna is replaced by cross antenna in the one antenna applicator, E field in this cut plane is circular polarized, the E field direction at any point on this plane is rotated 360 degree in one period and the magnitude of the E field does not change in the rotation. When the E field is circular polarized, The E field distribution and the penetration of E field are uniform around the tumor which is shown in Fig. Figure 8.6b.

8.4.3 Single cross antenna applicator at 915MHz

The E field seems better penetration into tumor from the simulation results, although the poor penetration depth at 915MHz was reported by the clinical application. Different shape, size and material of the bolus can partially explain the different between the simulation and clinical experience. Some factors could give the reason that the 915MHz has good penetration into to deep tumor. One of them is that the permittivity difference between the tumor and fat at 915MHz is smaller than that at 140MHz or 100MHz and it is same to the conductivity, which lows the reflection coefficient at tumor/fat boundary. The other one is that the low oil permittivity helps EM energy entering the breast. But the low oil permittivity also helps EM energy leaking out of the bolus.

The rib has no blood flow to help cooling down the temperature during the treatment, so the ribs are very easy to heat up if there is amount of SAR in rib region. The decay of EM at 915MHz in the behind tumor region is higher than that at 140MHz, because the conductivities of fat, tumor and muscle at 915MHz are higher than that at 140MHz. So the EM wave decays to very low level when it reaches the ribs, which is shown in Fig. Figure 8.8 and Fig. Figure 8.9.

The power efficiency of this applicator is not calculated. Given enough power input into this applicator, it will heat the tumor (3-4cm deep) very well without burning the breast skin. This applicator also showing a promising result on heating the shifted tumor. The tumor will be heated without positioning the applicator to align the tumor on the axis of the antenna and the tumor needs not to be at the center of the breast, which happens to most of the breast cancer cases.

8.4.4 E field distribution in four antenna applicator

Fig. Figure 8.12 shows that simulations predict the approximate shape and location of the focus generated by the four antenna applicator. Figs. Figure 8.12b and Figure 3.6Figure 8.12b demonstrate that the focus is in the center of the water tank and is about 3 cm under the water surface. These figures demonstrate that the focus generated by this RF phased array is quite broad, which suggests that this device is appropriate for regional heating.

In time domain, the E field focus runs around the focus region and the E field vector is circular polarized in the cross antenna applicator, while the position of the focus is fixed and E field is linearly polarized for the applicator with dipole antenna. This property of the cross antenna applicator is helpful to remove the hot spots and the tumor/fat boundary will be heated more uniformly than that with dipole antenna applicator.

Coupling between antennas is also evident in these measurements. This coupling is in part caused by standing waves within the water tank. The standing wave pattern changes as the input phases and amplitudes are varied, which also changes the coupling between antennas. This coupling also changes depending on the load in the water tank. In particular, the coupling changes for different water levels and for different phantom materials placed in a plastic cup on the water surface. This coupling is responsible in part for the differences between the measured and simulated phase and amplitude settings required for a focus in the center of the tank and for a steered focus. These effects, which are commonly encountered in RF phased array systems designed for hyperthermia [?, 34, ?], are reduced by focusing the breast applicator in center of the water tank so that the reflected powers are minimized. This defines the location where preferential focusing is achieved for this RF phased array applicator.

8.5 Conclusion

Linear polarization heating is found in the dipole type antenna applicator, which will cause two hot spots outside the tumor along the polarization direction. A new type antenna, cross antenna, is designed for regional hyperthermia to avoid this kind of polarization hot spots. The electromagnetic (EM) wave propagation along the cross antenna and the electric field distribution in time domain is inspected with the Finite Difference in Time Domain (FDTD) simulation. The 90 degree phase shift between two branches and the circular polarization of E field in the target region are verified. The average SAR around and inside the tumor is more homogeneous than that by dipoles. A new single cross antenna applicator at 915MHz is proposed to heating breast cancer with oil bolus. E field, SAR and temperature are simulated for this applicator with simple breast model. Another four cross antenna phased array is also proposed to treat breast cancer at 140MHz with water bolus. The results of E field distribution of this array applicator shows there is a E field focus at the center of the applicator and under the water/air surface, where is the tumor location in the treatment.

CHAPTER 9

SUMMARY AND FUTURE RESEARCH

Several novel applicators, RF phased array and RF/US hybrid applicator are simulated with E field, pressure field, SAR and temperature calculation and/or measured with E field probe and MRI scanner. The four antenna applicator and the five antenna applicator had good performance in clinical treatment. The hybrid applicators show the best heating performance which can be obtained through physical modalities. The electric field polarization effect on hyperthermia was found in the simulation study of the RF applicator. The applicator should avoid aligning the antenna in the same direction, which will cause linear polarization with fixed direction. The circular polarization was first introduced into the design of the RF applicator and the cross antenna with delay line was designed to radiate the CP wave. The one cross antenna applicator offers good heating performance in a small breast.

The RF (or hybrid) applicator and MRI integrated system is a promising clinical application or equipment for deep seated tumor hyperthermia treatment. The MRI system can be used for imaging the target area, tumor region recognition and temperature guidance for treatment.

Relationship between the wavelength and applicator size

The size or dimension of the applicator should be determined at first when designing a new applicator. For non-invasive breast applicator, current majority designs are plastic enclosure with antenna mounted on the inner surface and the enclosure is filled with some media, such as water, mineral oil and etc. According to simulation results in this thesis, the dimension of the applicator in any direction should be in the range 1λ 2λ(this is experience value, not a mathematic solution). If the size/wavelength ratio is much larger than 2, some parasitical standing wave would exist somewhere in the applicator, which can cause skin burn. If the size/wavelength ratio is smaller than 1, it is not easy for E field focusing and steering in the phased array applicator.

Optimization method for hybrid SAR

There are numbers of method for RF or US hyperthermia individually. But there is no method currentlt available for RF/US hybrid application. In this thesis, the weights of RF and US power are optimized, while the ultrasound SAR distribution and RF SAR distribution are optimized individually.

Close-loop control of applicator by temperature feed back

The integration of hyperthermia system and MR system still needs time to fit the clinical requirement. The electromagnetic interference between RF applicator and MR system is not clearly understood. The software controlling the combined system is not sophisticated enough for clinical application.

The power inputs for all RF antennas and/or US channels currently are optimized with the geometric shape and material properties of the patient model. But in clinical treatment, hot spots in healthy tissue are inevitable and some part of the tumor is not well heated. The method using temperature as optimization parameter to control the applicator is still not well developed.

Blood flow by MR Angiography (MRA)

The blood flow strongly effects the heat diffusion in the treatment region. In the simulation, blood perfusion is a constant and homogeneous value in one tissue. Actually the blood flow is not constant and homogeneous for one tissue and the blood flow is high in vessel and in the high temperature region. MRA can image the distribution of the blood vessel and the velocity of the blood flow. With the image of the blood vessel in the treatment region, the treatment plan can give much more precise result. The online feed back of the blood flow change offers more parameters for further heating optimization.

BIBLIOGRAPHY

BIBLIOGRAPHY

[1] W. T. Joines, Y. Zhang, C. Li, and R. L. Jirtle, "The measured electrical properties of normal and malignant human tissues from 50 to 900 mhz," *Med. Phys.*, vol. 21, no. 4, pp. 547–550, Jan 1994.

[2] H. Kroeze, J. B. Van de Kamer, A. A. C. De Leeaw, and J. J. W. Lagendijk, "Regional hyperthermia applicator design using FDTD modelling," *Physics in Medicine and Biology*, vol. 46, no. 7, pp. 1919–1935, 2001.

[3] J. van der Zee, "Heating the patient: A promising approach?," *Annals of Oncology*, vol. 13, pp. 1173–1184, 2002.

[4] B. Hildebrandt, P. Wust, O. Ahlers, and et al., "The cellular and molecular basis of hyperthermia," *Critical Reviews in Oncology/Hematology*, vol. 43, pp. 33–56, 2002.

[5] P. Wust, B. Hildebrandt, G. Sreenivasa, and et al., "Hyperthermia in combined treatment of cancer," *The Lancet Oncology*, vol. 3, pp. 487–497, 2002.

[6] J. L. Volakis, A. Chatterjee, and L. C.Kempel, *Finite Element Method for Electromagnetics*, p. 161. New York: IEEE press, 1998.

[7] J. Jin, *The Finite Element Method in Electromagnetics*, p. 15. New York: John Wiley and Sons, INC, 2002.

[8] D. M. Sullivan, D. T. Borup, and O. P. Gandhi, "Use of the finite-difference time-domain method in calculating EM absorption in human tissues," *IEEE Trans. Biomed. Eng.*, vol. 34, no. 2, pp. 148–157, 1987.

[9] K. D. Paulsen, X. Jia, and J. M. J. Sullivan, "Finite element computations of specific absorption rates in anatomically conforming full-body models for hyperthermia treatment analysis," *IEEE Trans. Biomed. Eng.*, vol. 40, no. 9, pp. 933–945, 1993.

[10] S. T. Clegg, S. K. Das, E. Fuller, S. Anderson, J. Blivin, J. R. Oleson, and T. V. Samulski, "Hyperthermia treatment planning and temperature distribution reconstruction: A case study," *Int. J. Hypertherm.*, vol. 12, no. 1, pp. 65–76, 1996.

[11] J. C. Kumaradas and M. D. Sherar, "Edge-element based finite element analysis of microwave hyperthermia treatments for superficial tumours on the chest wall," *Int. J. Hypertherm.*, vol. 19, no. 4, pp. 414–430(17), Jul-Aug 2003.

[12] E. G. Williams and M. J. D., "Numerical evaluation of the rayleigh integral for planar radiators using the fft," *J. Acoust. Soc. Am.*, vol. 72, no. 6, pp. 2020–2030, 1982.

[13] P. T. Christopher and K. J. Parker, "New approaches to the linear propagation of acoustic fields," *J. Acoust. Soc. Am.*, vol. 90, no. 1, pp. 507–521, 1991.

[14] P. Wu and T. Stepinski, "Extension of the angular spectrum approach to curved radiators," *J. Acoust. Soc. Am.*, vol. 105, no. 5, pp. 2618–2627, 1999.

[15] P. Wu, R. Kazys, and T. Stepinski, "Analysis of the numerically implemented angular spectrum approach based on the evaluation of two-dimensional acoustic fields 1. errors due to the discrete fourier transform and discretization," *J. Acoust. Soc. Am.*, vol. 99, no. 3, pp. 1339–1348, 1996.

[16] P. Wu, R. Kazys, and T. Stepinski, "Optimal selection of parameters for the angular spectrum approach to numerically evaluate acoustic fields," *J. Acoust. Soc. Am.*, vol. 101, no. 1, pp. 125–134, 1997.

[17] P. Wu, R. Kazys, and T. Stepinski, "Analysis of the numerically implemented angular spectrum approach based on the evaluation of two-dimensional acoustic fields 2. characteristics as a function of angular range," *J. Acoust. Soc. Am.*, vol. 99, no. 3, pp. 1349–1359, 1996.

[18] S. K. Das, S. T. Clegg, and T. V. Samulski, "Electromagnetic thermal therapy power optimization for multiple source applicators," *Int. J. Hypertherm.*, vol. 15, no. 4, pp. 291–308, 1999.

[19] J. Wiersma, V. M. RAM, and V. D. JDP, "A flexible optimization tool for hyperthermia treatments with rf phased array systems," *Int. J. Hypertherm.*, vol. 18, no. 2, pp. 73–85, Mar 2002.

[20] G. C. Van Rhoon, D. J. Van der Heuvel, A. Ameziane, P. J. M. Rietveld, K. Volenec, and J. Van der Zee, "Characterization of the sar-distribution of the sigma-60 applicator for regional hyperthermia using a schottky diode sheet," *Int. J. Hypertherm.*, vol. 19, no. 6, pp. 642–654, Nov-Dec 2003.

[21] S. K. Das, S. T. Clegg, and T. V. Samulski, "Computational techniques for fast hyperthermia temperature optimization," *Med. Phys.*, vol. 26, no. 2, pp. 319–328, 1999.

[22] K. Hynynen, O. Pomeroy, D. N. Smith, P. E. Huber, N. J. McDannold, J. Kettenbach, J. Baum, S. Singer, and F. A. Jolesz, "Mr imaging-guided focused ultrasound surgery of fibroadenomas in the breast: A feasibility study," *Radiology*, vol. 219, no. 1, pp. 176-185, 2001.

[23] Y. Zhang, W. T. Joines, R. L. Jirtle, and T. V. Samulski, "Theoretical and measured electric field distributions within an annular phased array: Consideration of source antennas," *IEEE Trans. Biomed. Eng.*, vol. 40, no. 8, pp. 780–787, 1993.

[24] Y. Fujita, H. Kato, and T. Ishida, "An rf concentrating method using inductive aperture-type applicators," *IEEE Trans. Biomed. Eng.*, vol. 40, no. 1, pp. 110–113, JAN 1993.

[25] H. Kato and T. Ishida, "Present and future-status of noninvasive selective deep heating using rf in hyperthermia," *Medical and Biological Engineering and Computing*, vol. 31, no. S, pp. 2–11, Jul 1993.

[26] C. Gromoll, U. Lamprecht, T. Hehr, M. Buchgeister, and M. Bamberg, "An online phase measurement system for quality assurance of the bsd 2000. part i: technical description of the measurement system," *Int. J. Hypertherm.*, vol. 16, no. 4, pp. 365–373(9), July 2000.

[27] M. Malinen, T. Huttunen, K. Hynynen, and J. P. Kaipio, "Simulation study for thermal dose optimization in ultrasound surgery of the breast," *Med. Phys.*, vol. 31, no. 5, pp. 1296–1307, 2004.

[28] P. Wust, J. Nadobny, R. Felix, P. Deuflhard, A. Louis, and W. John, "Strategies for optimized application of annular-phased-array systems in clinical hyperthermia," *Int. J. Hypertherm.*, vol. 7, no. 1, pp. 157–173, 1991.

[29] P. F. Turner, "Mini-annular phased-array for limb hyperthermia," *IEEE Transactions on Microwave Theory and Techniques*, vol. MTT-34, no. 5, pp. 508–513, 1986.

[30] A. J. Fenn, G. L. Wolf, and R. M. Fogle, "An adaptive microwave phased array for targeted heating of deep tumours in intact breast: animal study results," *Int. J. Hypertherm.*, vol. 15, no. 1, pp. 45–61, 1999.

[31] P.F.Turner, "Regional hyperthermia with an annular phased array," *IEEE Trans. Biomed. Eng.*, vol. 31, no. 1, pp. 106–14, Jan 1984.

[32] K. D. Paulsen, J. W. Strohbehn, S. C. Hill, D. R. Lynch, and F. E. Kennedy, "Theoretical temperature profiles for concentric coil induction heating devices in a two-dimensional, axi-symmetric, inhomogeneous patient model," *Int. J. Radiat. Oncol. Biol. Phys.*, vol. 10, pp. 1095–1107, 1984.

[33] K. D. Paulsen, J. W. Strohbehn, and D. R. Lynch, "Theoretical electric field distributions produced by three types of regional hyperthermia devices in a three-dimensional homogeneous model of man," *IEEE Trans. Biomed. Eng.*, vol. 35, no. 1, 1988.

[34] S. N. Hornsleth, L. Frydendal, O. Mella, O. Dahl, and P. Raskmark, "Quality assurance for radiofrequency regional hyperthermia," *Int. J. Hypertherm.*, vol. 13, no. 2, pp. 169–185, Mar-Apr 1997.

[35] D. M. Sullivan, "Mathematical methods for treatment planning in deep regional hyperthermia," *IEEE Trans. Microwave Theory Tech.*, vol. 39, no. 5, pp. 864–872, 1992.

[36] D. L. Carter, J. R. MacFall, S. T. Clegg, X. Wan, D. M. Prescott, H. C. Charles, and T. V. Samulski, "Magnetic resonance thermometry during hyperthermia for human high-grade sarcoma," *Int. J. Radiat. Oncol. Biol. Phys.*, vol. 40, no. 4, pp. 815–822, 1998.

[37] L. Wu, R. J. McGough, O. A. Arabe, and T. V. Samulski, "An rf phased array applicator designed for hyperthermia breast cancer treatments," *Phys. Med. Biol.*, vol. 51, no. 2006, pp. 1–20, Jan 2006.

[38] L. Wu and R. J. McGough, "The effect of e-field polarization on hyperthermia breast cancer treatments," *the 2006 Annual Meeting of the Society for Thermal Medicine*, Apr 2006.

[39] R. J. McGough, J. F. Kelly, and T. V. Samulski, "An efficient grid sectoring method for calculations of the nearfield pressure generated by a circular piston," *J. Acoust. Soc. Am.*, vol. 115, no. 5, pp. 1942–1954, 2004.

[40] P. R. Stepanishen and K. C. Benjamin, "Forward and backward projection of acoustic fields using FFT methods," *J. Acoust. Soc. Am.*, vol. 71, no. 4, pp. 803–812, 1982.

[41] G. T. Clement and K. Hynynen, "Field characterization of therapeutic ultrasound phased arrays through forward and backward planar projection," *J. Acoust. Soc. Am.*, vol. 108, no. 1, pp. 441–446, 2000.

[42] R. J. McGough, H. Wang, E. S. Ebbini, and C. A. Cain, "Mode scanning: heating pattern synthesis with ultrasound phased arrays," *Int. J. Hypertherm.*, vol. 10, no. 3, pp. 433–42, May-Jun 1994.

[43] E. S. Ebbini, "Deep localized hyperthermia with ultrasound phased arrays using the pseudoinverse pattern synthesis method," *Thesis for PHD degree in Electrical Engineering in the Graduate College of UIUC*, 1990.

[44] R. J. McGough, E. S. Ebbini, and C. A. Cain, "Direct computation of ultrasound phased-array driving signals from a specified temperature distribution for hyperthermia," *IEEE Trans. Biomed. Eng.*, vol. 39, no. 8, pp. 825–835, 1992.

[45] K. D. Paulsen, J. W. Strohbehn, and D. R. Lynch, "Theoretical temperature distributions produced by an annular phased array-type system in CT-based patient models," *Radiation Research*, vol. 100, pp. 536–552, 1984.

[46] K. S. Nikita, N. G. Maratos, and N. K. Uzunoglu, "Optimal steady-state temperature distribution for a phased array hyperthermia systemn," *IEEE Trans. Biomed. Eng.*, vol. 40, p. 1299¨C1306, 1993.

[47] D. S. Sullivan, R. Ben-Yosef, and D. S. Kapp, "Stanford 3d hyperthermia treatment planning system. technical review and clinical summary," *Int. J. Hypertherm.*, vol. 9, p. 627¨C643, 1993.

[48] S. K. Das, S. T. Clegg, and T. V. Samulski, "Computational techniques for fast hyperthermia temperature optimization," *Med. Phys.*, vol. 26, no. 2, pp. 319–328, Feb 1999.

[49] F. Bardati, A. Borrani, A. Gerardino, and G. Lovisolo, "Sar optimization in a phased-array radiofrequency hyperthermia system," *IEEE Trans. Biomed. Eng.*, vol. 42, no. 12, pp. 1201–1207, DEC 1995.

[50] P. Wust, M. Seebass, J. Nadobny, P. Deuflhard, G. Monich, and R. Felix, "Simulation studies promote technological development of radiofrequency phased array hyperthermia," *Int. J. Hypertherm.*, vol. 12, no. 4, pp. 477–494, 1996.

[51] C. Cain and S. Umemura, "Concentric-ring and sector vortex phased array applicators for ultrasound hyperthermia," *IEEE Trans. Microwave Theory Tech.*, vol. 34, no. 5, pp. 542–551, 1986.

[52] S. Umemura and C. Cain, "The sector-vortex phased array: acoustic field synthesis for hyperthermia," *IEEE Trans. Ultrason. Ferroelect. Freq. Contr.*, vol. 36, no. 2, pp. 249–257, 1989.

[53] K. Hynynen, G. T. Clement, N. McDannold, N. Vykhodtseva, R. King, P. J. White, S. Vitek, and F. A. Jolesz, "500-element ultrasound phased array system for noninvasive focal surgery of the brain: A preliminary rabbit study with ex vivo human skulls," *Magn. Reson. Med.*, vol. 52, no. 1, pp. 100–107, Jun 2004.

[54] D. Chorman and R. J. McGough, "Development of prototype phased array ultrasound system for hyperthermia and targeted drug delivery," *Proceedings of the acoustics week in Cannada 2005*, vol. 33, no. 3, pp. 88–90, Sep 2005.

[55] R. J. McGough, T. V. Samulski, and J. F. Kelly, "An efficient grid sectoring method for calculations of the nearfield pressure generated by a circular piston," *Journal of Acoustic Society of America*, vol. 115, no. 5, pp. 1942–54, May 2004.

[56] J. Wang and O. Fujiwara, "Fdtd computation of temperature rise in the human head for portable telephones," *IEEE Trans. Microwave Theory Tech.*, vol. 47, no. 8, pp. 1528–34, Aug 1999.